AGARD

ADVISORY GROUP FOR AEROSPACE RESEARCH & DEVELOPMENT

7 RUE ANCELLE 92200 NEUILLY-SUR-SEINE FRANCE

AGARD REPORT No. 598

on

Experiments on Management of Free-Stream Turbulence

by

R.I.Loehrke and H.M.Nagib

NORTH ATLANTIC TREATY ORGANIZATION

NORTH ATLANTIC TREATY ORGANIZATION

ADVISORY GROUP FOR AEROSPACE RESEARCH AND DEVELOPMENT

(ORGANISATION DU TRAITE DE L'ATLANTIQUE NORD)

AGARD Report No.598

EXPERIMENTS ON MANAGEMENT OF FREE-STREAM TURBULENCE

by

R.I.Loehrke and H.M.Nagib

Mechanics and Mechanical and Aerospace
Engineering Department
Illinois Institute of Technology
Chicago, Illinois 60616
USA

Edited by

Professor M.V.Morkovin, Illinois Institute of Technology
and
Professor D.Küchemann, Royal Aircraft Establishment
Farnborough, Hampshire, England

This Report has been prepared at the request of the Fluid Dynamics Panel of AGARD.

THE MISSION OF AGARD

The mission of AGARD is to bring together the leading personalities of the NATO nations in the fields of science and technology relating to aerospace for the following purposes:

- Exchanging of scientific and technical information;
- Continuously stimulating advances in the aerospace sciences relevant to strengthening the common defence posture;
- Improving the co-operation among member nations in aerospace research and development;
- Providing scientific and technical advice and assistance to the North Atlantic Military Committee in the field of aerospace research and development;
- Rendering scientific and technical assistance, as requested, to other NATO bodies and to member nations in connection with research and development problems in the aerospace field.
- Providing assistance to member nations for the purpose of increasing their scientific and technical potential;
- Recommending effective ways for the member nations to use their research and development capabilities for the common benefit of the NATO community.

The highest authority within AGARD is the National Delegates Board consisting of officially appointed senior representatives from each Member Nation. The mission of AGARD is carried out through the Panels which are composed for experts appointed by the National Delegates, the Consultant and Exchange Program and the Aerospace Applications Studies Program. The results of AGARD work are reported to the Member Nations and the NATO Authorities through the AGARD series of publications of which this is one.

Participation in AGARD activities is by invitation only and is normally limited to citizens of the NATO nations.

Published September 1972

533.6.011

Printed by Technical Editing and Reproduction Ltd
Harford House, 7–9 Charlotte St. London W1P 1HD

PREFACE

Special appreciation goes to Mark V.Morkovin, who suggested the initial line of the investigation, advised and argued with us whenever asked, and contributed to Chapter VI. We are indebted to Robert J.Hannemann, John M.Hogan, Jimmy Tan-atichat, Julie T.Yung, and George H.Ruiter who carried out some of the measurements over the last two and a half years. These measurements were needed for various investigations sponsored by the Themis Project, USAF OSR Contract F44620-69-C-0022, which is monitored by Capt. W.H.Smith. This Report also constitutes AFOSR Report TR-72-0077 on the above contract. We wish to acknowledge the skill and patience of Martin Iwamuro in drafting and arranging all the figures and Marsha G.Faulkner in preparing the final manuscript.

Insofar as the Report appears integrated into the body of past knowledge on generation and control of turbulence, the credit goes to G.B.Schubauer, S.Corrsin, and J.L.Lumley, who offered patient though critical comments on the first draft of the Report.

The AGARD Fluid Dynamics Panel wishes to thank Professors M.V.Morkovin and D.Küchemann for their contributions in undertaking the review and editing of this AGARD Report, which was prepared by the authors in support of the AGARD Fluid Dynamics Panel Large Wind Tunnels Working Group, chaired by Professor D.Küchemann.

ABSTRACT

The effects of various passive devices (screens, perforated plates, porous foam, and honeycomb-like matrices formed with closely packed plastic drinking straws) on free-stream turbulence and mean velocity profiles are studied in air with hot-wire anemometry and in water using hydrogen-bubbles visualization. These "turbulence manipulators" are viewed as operators which suppress the level of the incoming turbulence and generate, primarily through documented instabilities, new turbulence with scales characteristic of the device and its shear layers. In this sense these manipulators can be used to control, manage and/or modify the incoming turbulence flow to yield the one appropriate to the application.

The level, structure and decay of the generated turbulence depends, in part, on the instabilities and therefore can be modified by passive devices acting on the shear layers immediately downstream of the manipulator. For honeycombs, the suppression of the incoming turbulence appears to be mostly due to the inhibition of lateral components of the fluctuating velocity. For most devices, it is conjectured that part of the energy in the undesirable larger scales of motion drains away through the action of the Reynolds stresses of the smaller scale laminar and turbulent motions (including the instabilities). The performance of the manipulators is found to depend on the characteristics of the incoming turbulence including its frequency spectra, level, and spatial distribution and on the incoming mean flow profiles. The efficacy of devices generating large scale turbulence in smoothing out gross inhomogeneities in the mean velocity profiles is illustrated. By contrast, in flows with only fine-scale and/or low-level turbulence, mean velocity nonuniformities tend to persist. Some combined interacting manipulators are more effective, on the basis of equal pressure drop, in reducing free-stream turbulence and uniformizing the mean velocity profiles than individual manipulators.

CONTENTS

*In Collaboration with M. V. Morkovin, Mechanics and Mechanical and Aerospace Engineering Department, Illinois Institute of Technology, Chicago, Illinois 60616 U.S.A.

LIST OF FIGURES

NOTATION

A,B,C,D,E,F	Test flow conditions; see pages 12 through 14 and 21
b	Constant used in Equations (I-17), page 6, and (VI-1), page 31
C_D	Grid drag coefficient or its equivalent when used for honeycomb
F_1,F_2,F_3	Turbulence reduction factors in the streamwise and the two lateral directions; defined as the ratio of the effective u_i' at the inlet of the manipulator with the manipulator in place to the value of u_i' at the same position in absence of the manipulator. The effective u_i' at the inlet is obtained by taking the value of u_i' at the operational downstream boundary of the manipulator and extrapolating back to the inlet using the slope of the decay curve of the turbulence in absence of the manipulator (operational downstream boundary is defined on page 28).
$\bar{F}_1,\bar{F}_2,\bar{F}_3$	Reduction factors of the spatial variations in the streamwise and two lateral mean velocity components; defined as the effective spatial variations in $\bar{U}_i$ at the inlet of the manipulator with the manipulator in place to the spatial variations in $\bar{U}_i$ at the same position in absence of the manipulator. The effective spatial variations in $\bar{U}_i$ at the inlet is obtained by taking the value of the spatial variations at the operational downstream boundary of the manipulator and extrapolating back to the inlet using the slope of the decay curve of the spatial variations in absence of the manipulator (operational downstream boundary is defined on page 28).
F_{1n}	Turbulence reduction factor in the streamwise direction, F_1, due to n screens placed in series
f	Frequency
f^*,f^*_ℓ	Characteristic frequency of shear layer instability downstream of turbulence manipulator of length ℓ
i	$= \sqrt{-1}$; when used as a subscript, indicates 1, 2, or 3
K	Pressure-drop coefficient $\equiv \dfrac{\Delta P}{\frac{1}{2}\rho U_\infty^2}$
K*	Pressure-drop coefficient defined by Equation (I-12), page 5.
L	Turbulence integral scale
ℓ	Physical length of single or combined turbulence manipulator in the streamwise direction
ℓ_o	Operational length of single or combined turbulence manipulator in streamwise direction; equal to distance from the upstream boundary to the operational downstream boundary of the manipulator (see page 28)
M	Mesh length or distance between openings of the different turbulence manipulators
P	Static pressure
q	Fluctuating velocity ($q^2 = u_i u_i = u_1^2 + u_2^2 + u_3^2$)
q'	rms value of q
Re_M	Reynolds number based on the mesh size $= \dfrac{MU_\infty}{\nu}$
r	Radial direction measured from an arbitrary point in the test section
U	Instantaneous velocity in the streamwise direction $= U_1 = \bar{U} + u$
$\bar{U}$	Time-mean value of U
U_∞	Time average velocity of flow with a uniform lateral velocity distribution
U_1,U_2,U_3	Components of velocity in the streamwise and two lateral directions
u	Fluctuating velocity component in streamwise direction $= u_1$
u_1,u_2,u_3	Components of fluctuating velocity in the streamwise and two lateral directions
u_i'	rms value of u_i

$(u')_{average}$	Average value of u' over the test section cross section
x	Axial distance in the streamwise direction measured from the downstream end of single or combined turbulence manipulator
Δx	Separation distance between turbulence manipulators placed in series
x_o	Axial location of virtual origin of turbulence decay; see Equation (I-17), page 6
x_1, x_2, x_3	Eulerian Cartesian Coordinates
α	Refraction coefficient of screen = ϕ/θ
∂	Partial differential operator
ζ	Axial distance in the streamwise direction measured from the downstream end of the turbulence manipulator generating the test flow condition
ζ_o	Separation distance between obstacle and upstream end of turbulence manipulator (see Fig. 7B)
η	Turbulence energy reduction factor $(\overline{q}^2)$ downstream/$(\overline{q}^2)$ upstream
θ	Angle between mean velocity vector and the normal to the plane of the screen on the upstream side
κ_1	Streamwise component of wave-number vector
λ	Turbulence microscale
μ	Fluid dynamic viscosity
ν	Fluid kinematic viscosity
ω_i	Vorticity
ξ	A screen parameter defined by Equation (I-9), page 4
π	A screen parameter defined by Equation (I-10), page 4
ρ	Fluid density
σ	Solidity of turbulence manipulator; equal to the solid area divided by the total cross-sectional area
ϕ	Angle between mean velocity vector and the normal to the plane of the screen on the downstream side

CHAPTER I
INTRODUCTION

A. OBJECTIVES

With a rising need for special purpose wind tunnels and other fluid-mechanical experimental facilities, there is an increasing demand for the understanding of the means by which turbulence may be controlled and managed. An engineer facing such design problems will find in this report a rapid guide to past and present experience, providing him with phenomenological interpretations (not rigorously documented precepts) of the various mechanisms that are currently believed to govern the performance of various flow inserts.

The study is thus intended to provide help to the engineer faced with the need to control the turbulence in an air stream while being constrained by the permissible pressure drop, by structural requirements and by the size, cost and availability of the materials required to accomplish his task. It is hoped that the numerous examples illustrating the complexity of the hidden mechanisms will also furnish him with a broad enough spectrum of data for use in his particular application.

Selected data for single devices and for closely coupled manipulators are presented in Chapters IV and V and are accompanied by a minimum of explanations leaving their interpretation to the unbiased reader. In Chapter VI an attempt is made to correlate this material with various experiences and theories culminating in an openly subjective "recipe" for the sequential approach to a design problem. It should therefore be understood that for the sake of engineering usefulness, the material presented in Chapter VI goes beyond currently accepted, fully documented concepts. In addition, a number of unsettled issues are identified with a view to further research.

B. INTRODUCTION AND BACKGROUND

One of the most important tools in the study of laminar instabilities, transition phenomena, and the mixing of turbulent streams is a wind tunnel with a uniform mean velocity and a low or controllable turbulence level. The work reported here was initiated in response to the need at I.I.T. for several such facilities.

The most popular scheme for producing a flow of low turbulence in a wind tunnel consists of a series of fine mesh screens located in the settling chamber that serve to decrease the absolute level of the turbulence, u_1', u_2', u_3'. The screens are usually followed by a contraction that decreases at first the relative intensity u_1'/U_∞ and ultimately u_2'/U_∞ and u_3'/U_∞. Sometimes precision honeycombs are used in place of the screens particularly in water tunnels where higher dynamic loads may make the installation of screens difficult. Although honeycombs have been utilized in this application for a longer time than screens, their use has been somewhat limited due to their high cost. Various types of honeycombs are frequently found in water channels and open return tunnels, often in conjunction with several screens and a contraction section.

A considerable amount of theoretical and experimental information is available on the effect of screens on turbulence (see section C of this chapter). All of the available theoretical studies assume that the incoming turbulence is isotropic and homogeneous while the experimental studies are primarily concerned with the details of the effect of screens on grid-generated turbulence. Usually the state of the flow in the settling chambers of wind tunnels and in other installations of practical interest differs from such conditions. Separation and secondary flows in corners, fan-induced swirls in closed circuit tunnels and disturbances caused by the surroundings of open return tunnels (e.g., the flow field induced by room air-conditioning systems and spatial asymmetries near the tunnel intake) are examples of the gross inhomogeneities and unisotropies that one may encounter. Because of situations of this sort this study includes the investigation of combinations of various devices such as screens and honeycombs that could be more effective than screens alone in reducing turbulence levels and in removing nonuniformities in u' and $\bar{U}$.

Within the present context a flow insert (or device) can be thought of as an operator which transforms the incoming turbulence $(u_1')_{in}$, $(u_2')_{in}$ and $(u_3')_{in}$ to exiting turbulence $(u_1')_{out}$, $(u_2')_{out}$ and $(u_3')_{out}$. One can picture the operation schematically as a combination of a damping or suppression module with a generation module as shown below. The suppression and generation functions may not necessarily occur in series as shown and they may be different for u_1', u_2', and u_3'.

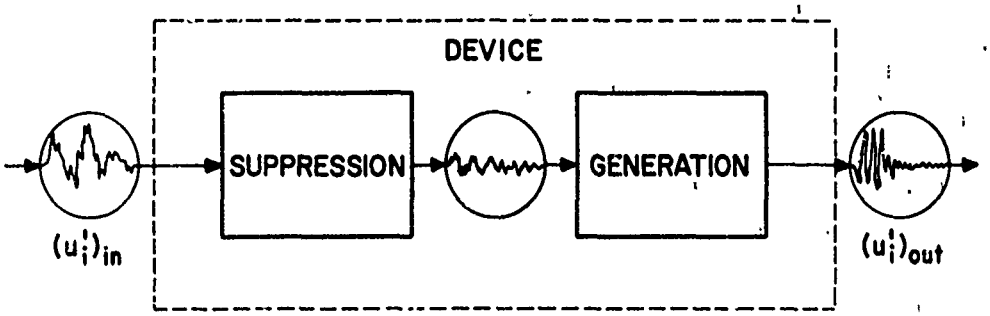

NOTE:
$(u_i')_{in}$ & $(u_i')_{out}$ ARE FUNCTIONS OF X.

The process of generation of turbulence may be due to instabilities of wakes caused by the device or to boundary layers generated within the device (as in honeycombs at high Reynolds numbers), or to the action of the Reynolds stress $\overline{u_1u_2}$ on the mean shear (i.e., $\overline{u_1u_2}\,\partial\bar{U}_1/\partial x_2$). However, the ultimate effect of these generation processes may at times be an overall reduction in turbulence level as pointed out by Corrsin[1] (p. 52), "...there may still be a net reduction in turbulence (due to the screen) far downstream if the screen (generated) turbulence is of somewhat smaller structure than the turbulence to be eliminated. The additional large wave number energy may be expected to accelerate the spectral transfer rate of the pre-existing small wave number energy, thus increasing its decay rate."

The suppression process may be due to the inhibition of the transverse velocity components, u_2 and u_3, by solid boundaries within the device or to cascades of energy transfer downstream of the device leading to the viscous dissipation of the turbulent motions.

As far as nonuniformities in the mean velocity are concerned, the effect of the device may be attributable to the pressure drop across the device and to the consequences of the turbulence generated by the device. Various factors may intervene with the latter mechanism, e.g., the relation between the spatial scale of the irregularities and of the structure of the incoming turbulence to the turbulence generated by the device.

In an operational sense the boundaries of the flow inserts may extend beyond their physical boundaries and these may be difficult to define especially on the downstream side. For our purposes we will define the incoming flow as that which would exist at the locus of the leading edge of the device in the absence of the device. The downstream boundary of the device is considered, operationally, to be located where the streamwise gradients of the mean and fluctuating velocities, $\partial\bar{U}/\partial x$ and $\partial u'/\partial x$, are about the same as they would be in the absence of the device.

One set of measures of the effectiveness of a flow insert are the turbulence factors F_i that are defined as the ratios of the effective u_i' at the inlet to the device with the device in place to the value of u_i' at the same location in absence of the device. The effective u_i' at the inlet is determined by extrapolation from the value of u_i' at the operational downstream boundary of the device with the aid of the turbulence decay curve obtained in absence of the device. This is the method used by Schubauer, Spangenberg

and Klebanoff[2], in the case of screens. In this manner, devices of widely different characteristics can be compared. (See the schematic diagram at the beginning of Chapter VI). The factors F_i may be expected to depend on the state of the entering flow including the structure of the incoming turbulence. The following sections summarize some of the literature of relevance to the present study.

C. SOME RELEVANT LITERATURE

In a study published in 1947, Dryden and Schubauer[3] make the following observations: "About 10 years ago the intensity of the turbulence in the average wind tunnel was in the range 0.5 to 1.0 per cent of the mean speed. Today there are several wind tunnels in which the intensity is of the order of 0.02 to 0.05 per cent." The number of high quality wind tunnels, with low or controllable free-stream turbulence levels, has increased considerably since the publication of that work and the volume of research directed toward the study of the effect of screens and grids on free-stream turbulence has grown equally since then. For a detailed review of this subject the reader is referred to Corrsin's[1] article on experimental methods in turbulence. A brief summary of the theoretical predictions of the effect of screens on free-stream turbulence and mean velocity nonuniformities and a careful experimental assessment of the characteristics of screens is found in the report of Schubauer, Spangenberg and Klebanoff[2].

A list of some past experimental and theoretical results[2-40] pertaining to the performance of screens and grids is given in the References. Others can be found in Corrsin's[1] article and in the classical texts of Batchelor[41], Townsend[42] and Hinze[43]. Some of the experiments[44-49] in which screen- or grid-generated turbulence has been utilized for the study of various aspects of turbulence and in which detailed measurements are reported downstream of screens and grids are also included in the References.

Lattices of parallel or bi-plane cylinders have been used to generate free-stream turbulence as well as to suppress it. Because of this empirically established dual function a lattice having a small-scale mesh (compared to the stream width), utilized at a small mesh Reynolds number is referred to as a damping screen, or simply as a screen or gauze. Lattices of a larger scale, employed at high mesh Reynolds numbers, Re_M, are called turbulence-producing grids.

Screens or grids are characterized usually by parameters describing their geometrical shape, mesh and solidity and the pressure drop across them. The range of these parameters for the devices utilized in the present experiments is apparent from Fig. 6.

1. Screens

Schubauer, et al.[2] define two possible regimes associated with the flow downstream of screens. When a screen operates in the first regime, labeled subcritical, the turbulence level immediately downstream of the screen is lower than the incoming turbulence. In the second regime, referred to as supercritical or above-critical, the velocity fluctuations immediately downstream of the screen are far in excess of those in the incoming stream. These fluctuations are found to decay rapidly with downstream distance and in most cases the turbulence far downstream of the screen reaches levels that are below the original free-stream turbulence.

All existing theories bypass this rise and fall in the velocity fluctuations occurring immediately downstream of a screen operating at above-critical conditions. Instead the screen is usually characterized by a loss coefficient $\Delta P/(\frac{1}{2}\rho U_\infty^2)$, referred to as the pressure drop coefficient K, and its linearized perturbation. The coefficient K is found experimentally and is assumed to be independent of the nature and the level of the incoming turbulence. In addition to K, a second empirical quantity, the refraction coefficient, α, is also used to characterize a screen. This coefficient α is the ratio of the angles enclosed between the mean stream direction and the normal to the screen downstream and upstream of it, i.e., $\alpha = \phi/\theta$.

From tests on a variety of screens Dryden and Schubauer[8] found that for small angles θ, the following empirical relationships hold:

$$\alpha = \frac{8 - K}{8 + K} \qquad \text{for } K < 0.7 \tag{I-1a}$$

and

$$\alpha = \frac{1.1}{\sqrt{1 + K}} \qquad \text{for } K > 0.7 \tag{I-1b}$$

Several theoretical formulas are available for the reduction factors of the spatial variations in the mean velocity $\overline{F}_i$ and the turbulence reduction factors F_i. They are presented in the following, but for the details of the theories the reader is referred to the original papers.

a. Prandtl[4]:
$$\overline{F}_1 = \frac{1}{1 + K} \tag{I-2}$$

b. Collar[5]:
$$\overline{F}_1 = \frac{2 - K}{2 + K} \tag{I-3}$$

c. Dryden and Schubauer[3]:
$$F_i = \frac{1}{\sqrt{1 + K}} \tag{I-4}$$

From Eq. (I-4) it is readily apparent that a number of screens, n, placed in series with a sufficient distance between them, have an overall reduction factor

$$F_{in} = \frac{1}{(1 + K)^{n/2}} \tag{I-5}$$

d. Taylor and Batchelor[7]:
$$\overline{F}_1 = \frac{1 + \alpha - \alpha K}{1 + \alpha + K} \tag{I-6}$$

$$\overline{F}_2 = \overline{F}_3 = \alpha \tag{I-7}$$

It is noteworthy that the results of Prandtl and Collar agree with two limiting cases of the formulas of Taylor and Batchelor, Eq. (I-6), i.e., when $\alpha = 0$ Eq. (I-6) reduces to Eq. (I-2) and when $\alpha = 1$ Eq. (I-6) reduces to Eq. (I-3). According to Dryden and Schubauer's[3] empirical findings, Eq. (I-1), these two limiting cases correspond to screens of very high and very low solidity, respectively.

Taylor and Batchelor[7] have also found that when the incoming turbulence is isotropic, the level of turbulence will be reduced across the screen according to the relations,

$$F_1^2 = \frac{(1 + \alpha - \alpha K)^2 + 2\alpha^2}{(1 + \alpha + K)^2 - 4} + \frac{(1 + \alpha - \alpha K)^2 - 4\alpha^2}{(1 + \alpha + K)^2 - 4} \cdot \frac{3}{2}(1 - \pi^2)\left[1 + \frac{\pi^2 - \xi^2}{2\pi} \log\left(\frac{\pi - 1}{\pi + 1}\right)\right] \tag{I-8}$$

where,
$$\xi^2 = \frac{(1 + \alpha - \alpha K)^2}{(1 + \alpha - \alpha K)^2 - 4\alpha^2} \tag{I-9}$$

and,
$$\pi^2 = \frac{(1 + \alpha + K)^2}{(1 + \alpha + K)^2 - 4} \tag{I-10}$$

The corresponding reduction factors in the lateral directions are given by:

$$F_2^2 = F_3^2 = \alpha^2 + \frac{1}{8}\left[(1 + \alpha - \alpha K)^2 - (1 + \alpha + K)^2 F_1^2\right] \tag{I-11}$$

Corrsin[1] notes in his review, in reference to the Taylor-Batchelor theory[7], that when the relation between α and K, Eq. (I-1), is introduced into Eqs. (I-6) and (I-7), the resulting numerical values of the reduction factors of the mean velocity nonuniformities, $\bar{F}_i$, are approximately equal to those of the turbulence reduction factors, F_i, obtained from Eqs. (I-8 through 11). That is, Corrsin[1] finds that if one assumed that

$$K \equiv \frac{\Delta P}{\frac{1}{2}\rho U_\infty^2} \simeq K^* \equiv \frac{d(\Delta P)}{d(\frac{1}{2}\rho U_\infty^2)} \tag{I-12}$$

it follows that for $K < 0.7$

$$F_1 \simeq \left[\frac{4 - K}{4 + K}\right]^2 \tag{I-13}$$

and, $$F_2 = F_3 \simeq \left|\frac{8 - K}{8 + K}\right| \tag{I-14}$$

and for $K > 0.7$

$$F_1 \simeq \left|\frac{1 + \frac{1.1}{\sqrt{1 + K}} - \frac{1.1K}{\sqrt{1 + K}}}{1 + \frac{1.1}{\sqrt{1 + K}} + K}\right| \tag{I-15}$$

and, $$F_2 = F_3 \simeq \frac{1.1}{\sqrt{1 + K}} \tag{I-16}$$

In the Taylor-Batchelor theory[7] the effect "...of gauze on small arbitrary unsteady disturbances--i.e., on turbulence--is also determined, on the assumption that the gauze wires produce no wake turbulence." Also, "With the assumption of small relative intensity of turbulence, the effect of the gauze is linear..." These statements appear to be at variance with the results in Fig. 5 of Ref. 2 (Schubauer, et al.[2]), where velocity fluctuations in excess of 10% of the mean speed are shown downstream of screens operating in the above-critical regime. We believe that these high levels of velocity fluctuations will influence the comparison between theory and experiment, even if the intensity of the incoming turbulence is low.

Even though it is relatively simple to evaluate the factors $\bar{F}_i$ and F_i using the formulas listed above, it is clear that K or both α and K must be known before the effect of a screen can be predicted. To date these parameters can be obtained only through experimental evaluation. In addition, as Corrsin[1] points out, "the K of any (low Reynolds number) screen varies with Reynolds number, so it (the screen) can be optimum for only a particular flow rate."

The various theories and experiments are compared by Taylor and Batchelor[7], Dryden and Schubauer[3], Townsend[10], Corrsin[1], Schubauer, et al.[2] They indicate better agreement in the reduction factors of the spatial variations in the mean velocity, $\bar{F}_i$, than in the turbulence reduction factors, F_i. We believe that the lack of agreement between the theoretical and experimental values of F_i is due to the fact that the theories treat the screen only as a turbulence suppressing device and do not include any mechanisms of generation of new turbulence by the screen (for details of the mechanisms see Chapter VI). While these generation mechanisms may be present only in the near-downstream region of the screen they could influence the level, structure, scale and rate of decay of turbulence and would thus have an effect on the performance of the screen. The measurements of Schubauer, et al.[2] (referred to earlier and presented in their Figs. 5, 6, 7, 9 and 10) strongly support this argument.

2. Grids and Perforated Plates

When a grid of low solidity is placed in a duct with uniform, steady flow of a much lower turbulence level than the turbulence to be generated by the grid, one can expect,

on the basis of previous experiments (e.g., see section A-I of Corrsin[1]), that the grid-generated turbulence will be reasonably isotropic far downstream. It has also been established that for a wide range of Reynolds numbers Re_M the turbulence energy decays downstream of this grid according to the relation

$$\left[\frac{U_\infty}{u'}\right]^2 = \frac{b}{C_D}\left[\frac{x}{M} - \frac{x_o}{M}\right] \qquad \text{(I-17)}$$

However, this so-called law of the initial period of decay does not apply to the first 20 to 30 mesh lengths downstream of the grid, where transverse inhomogeneities are usually present. The constant x_o designates the position of the virtual origin and is usually found to be in the range from 5M to 15M for square-mesh grids. The value of b appears to depend on the shape of the grid and hence the shape of the emerging velocity profiles. Some of the values for b reported by Batchelor[41] (p. 135) are: 101 for a double row of rods, 53 for a single row of rods and 91 for a single row of slats.

The studies of Tsuji[13,14] point out that the turbulence downstream of a grid will depend on the upstream turbulence. Batchelor[41] (p. 134) also remarks that the early measurements of the decay of grid-generated turbulence were a "little confused by the existence in the wind tunnel stream of turbulence from sources other than the grid." Based on these findings one may surmise that the dependence on the upstream flow conditions must be somehow introduced into Eq. (I-17) if one is to apply it to grids in flows with considerable turbulence levels.

Sometimes perforated plates are used in place of grids since their effect on the flow is quite similar. Baines and Peterson [12] and Davis[16] tested punched steel plates (or perforated plates) in their studies on grids. These flow inserts are commercially available and thus in many instances more convenient to use. In the present study three types of perforated plates with different hole size, mesh and solidity are examined.

3. Honeycomb

The literature available on the influence of honeycomb on turbulent flow fields is rather limited in spite of the fact that they have been used by many experimentalists over the years to reduce the turbulence level in wind and water tunnels. The most noteworthy information on this subject is contained in the papers by Lumley[50] and Lumley and McMahon[51]. An analysis similar to that of Taylor and Batchelor[7] on screens (discussed in section 1 above) has been carried out by Lumley [50] on honeycombs. In addition to the assumptions of Taylor and Batchelor[7], Lumley assumes that "the turbulence contains only wavelengths large compared to the cell size, or, in any event, that the fluid in a cell moves as a unit in response to fluctuating pressure fields due to the approaching turbulent stream. In addition, it has been assumed that the flow through an individual cell is fully developed; more specifically it has been assumed that the transverse velocity vanishes in passing through a cell. The requirement of full development of the flow then is just a way of requiring a sufficient number of characteristic times to have elapsed so that a perturbation of the profile (such as might be caused by a crossflow) will vanish. Finally, we require that the instantaneous skin friction in a cell is the same as the equilibrium value at the same mean velocity."

Lumley[50] defines a turbulence reduction factor (or honeycomb efficiency), η, given by the following expression

$$\eta \equiv \frac{(q')^2_{\text{downstream}}}{(q')^2_{\text{upstream}}} = 8\left[\frac{KL}{3\pi\ell}\right]^2 \int_0^1 \frac{dy}{\left[\frac{4KL(K+1)}{3\pi\ell}\right]^2 + y^2\left[1 + \frac{8K}{3\pi}\frac{L}{\ell}\frac{1}{\sqrt{1-y^2}}\right]^2} \qquad \text{(I-18)}$$

When this equation is applied sufficiently far downstream of the honeycomb so that the return to isotropy (Batchelor[41], pp. 67 and 133) has been achieved, it can be written as

$$\eta = \frac{(u_1')^2_{\text{downstream}}}{(u_1')^2_{\text{upstream}}} \qquad \text{(I-19)}$$

In his analysis, Lumley[50] observes that the K in Taylor and Batchelor's analysis[7] is replaced by $K(1-i\ell\kappa_1/K)$ in the case of the honeycomb. Thus, if a screen is considered analogous to a resistive impedance, the honeycomb may be regarded as the analog of a low-pass inductive-resistive filter. Lumley[50] also found that for equal pressure drops the honeycomb is more efficient in reducing the turbulence intensity than screens. For example, for $K = 1$ a honeycomb has the same η as that of four screens placed in series with a total $K = 4$. This comparison is based on screens with solidity of 0.45, which is the highest solidity at which screens are assured of not exhibiting anomalous behavior.

The paper by Lumley and McMahon[51] provides an additional input to the analysis: "In general, the turbulence created by the honeycomb arises from the flow in the cell and the breakup of the mean profile emanating from the individual cells. It is perhaps surprising that the turbulence created by the honeycomb is higher when the cell flow is laminar than when it is turbulent; the large wake characteristic of the laminar cell flow produces more turbulence than is lost in the laminarization of the cell flow."

The authors then estimate the contributions to the newly generated turbulence from energy balances across the honeycomb based on an empirical law of turbulence decay downstream of grids. These contributions, viewed at downstream distances x in excess of 20M, are apparent from the following explicit decay formulae:

a) For fully developed laminar flow in the cells:

$$\left[\frac{q'}{U_\infty}\right]^2 = \frac{0.03}{x/M} \qquad \text{(I-20)}$$

and when the return to isotropy is reached

$$\left[\frac{u_1'}{U_\infty}\right]^2 = \frac{0.01}{x/M} \qquad \text{(I-21)}$$

b) For fully developed turbulent flow in the cells:

$$\left[\frac{q'}{U_\infty}\right]^2 = \frac{0.0072}{x/M} \qquad \text{(I-22)}$$

and when the return to isotropy is reached

$$\left[\frac{u_1'}{U_\infty}\right]^2 = \frac{0.0024}{x/M} \qquad \text{(I-23)}$$

Lumley and McMahon[51] suggest that in the final period of decay the turbulence will decay according to the relation

$$(q')^2 \propto (x/M)^{-5/2} \qquad \text{(I-24)}$$

The final period of decay is reached when the turbulent microscale, λ, approaches the Loitsianskiy scale ($\mathcal{L} = \left[\int_0^\infty r^4 f(r)\,dr\right]^{1/5}$.) Lumley and McMahon[51] present working charts for the designer to choose the honeycomb type for his application (characterized by the cell size and length) based on their theory.

Honeycombs are usually given preferential use in water tunnels. The main reason for this is explained by Lumley and McMahon[51]: "Screens with wire diameters dictated by strength requirements operate in the Reynolds number range where vortex shedding occurs, this vortex shedding causes the familiar 'singing' effect. Attempts at using screens at the Ordnance Research Laboratory have met with failure due to this 'singing' effect. However, honeycombs in which the cells have a large length-to-diameter ratio have been used successfully to reduce turbulence to acceptable levels."

4. Porous Foam

Despite the large amount of literature available on flow through porous media (e.g., see De Wiest[52]), little is known concerning the effect of porous media on turbulence. In his experimental study of the mixing of coaxial jets, B. Johnson[53], has proposed the use of a combination of perforated plates and "Scott Foam" as a means of reducing the turbulence in the mixing streams. Although the details of the manner in which he attaches foam of different thicknesses to the downstream face of a perforated plate is not outlined in his report (see Chapter III for the method used in the present investigation), he does report success in using them. He concludes from the limited data presented that when the perforated plate plus foam is placed at the exit plane of the inner jet, the turbulence in the two mixing streams and hence the mixing between them is reduced.

In a more recent work by Bennett and Johnson[54], further details are presented. The objective of their study is to find methods of reducing the mixing between confined coaxial flows in short cylindrical chambers. The study is related to the development of open-cycle gaseous-core nuclear rockets, in which the velocity of the outer stream is much larger than that of the inner stream. "Scott Foam" of 20 and 30 pores/in. (nominal) and of thicknesses varying from 0.635 to 1.27 cm. is attached to the downstream end of perforated plates. The only information given about the plates used is their thickness, 0.159 cm. The "Scott Foam" used is referred to as of the industrial type (we interpret this to be nominally 3% dense). The porous plate formed by the combination of foam and perforated plate is placed at the entrance to the mixing chamber with its upstream side (the perforated plate) located immediately downstream of the inner jet exit.

Two reasons are given for the use of porous plates: a) To suppress the large scale eddy structure developed rapidly near the inlet plane of the mixing chamber which was observed by them in earlier studies to enhance the mixing; b) To reduce the velocity gradient across the shear layer between the jets in order to minimize the mixing.

Bennett and Johnson[54] present some flow visualization and hot-wire data for different mixing conditions and inlet configurations. Although no comparison with flows without porous plates or with the conditions upstream of the plates is presented, they conclude that for the flow with the minimum mixing "the maximum turbulence intensity was less than one-third the value previously reported for similar confined coaxial flows." They also note that using flow visualization no large-scale eddy motions are observed, and that for air-air mixing "the maximum ratio of outer-stream flow rate to the inner-stream flow rate for which the inner-jet gas filled 20% of the chamber volume was increased by a factor of 10 compared to the best previously measured results." The porous plate which yielded the best results was made of 30 pore/in. foam, 0.953 cm. thick, with a perforated plate, 0.159 cm. thick.

Since the results of Bennett and Johnson[54] and the more recent ones by Kunze, Suckling and Cooper[55] may hold promise for the techniques of controlling and reducing the amount of turbulence in free-streams, one phase of the present work was devoted to porous foam plates. Unfortunately, no comparison with Bennett and Johnson's[54] or Kunze, Suckling and Cooper's[55] results can be made because of the lack of information concerning the details of the distribution of the mean and fluctuating velocities both upstream and downstream of the porous foam plates in their experiments.

At I.I.T. a different porous material (General Electric "Nickel Foametal") has also been used to reduce the turbulence level in the flow of water entering circular pipes (e.g., see Nagib, et al.[56]).

CHAPTER II
FACILITY AND INSTRUMENTATION

The wind tunnel used in the present study was the compressed-air driven hot-wire calibration facility designed by Hannemann[57]. Construction details are included in the Appendix to this report. A plan view of the tunnel is shown in Fig. 1. Dry compressed air is introduced into an acoustically baffled, fiber-glass lined plenum chamber. The air enters the bellmouth to the test section after passing through a paper vacuum cleaner bag filter supported on a wire frame inside the plenum chamber. The 2.84 in. diameter test section is formed of segments of plexiglas tubing and flanges held in compression with tie rods. This construction scheme provides flexibility in location of the test objects. The maximum test section length used was approximately 30 inches. The test section opened into the lab providing access for the hot-wire probes used in the measurements.

The flow through the test section is maintained relatively constant regardless of the resistance of the object under test, by inserting a choked orifice upstream of the plenum chamber. Generally, only small variations in the average velocity, U_∞, from 15 fps were noted due to changes in the upstream pressure. The average air temperature in the test section was measured and found to be within 0.5°F of the ambient laboratory temperature.

The probes were mounted in a traversing mechanism located to the side of the tunnel exit. The probe was fitted in a DISA traversing mechanism which in turn was held in a milling machine indexing head. This arrangement provided for probe positioning in three perpendicular axes. The probe was positioned manually to an initial location using the milling head adjustments and then traversed automatically by the DISA unit which provided a position signal to one axis of an X-Y recorder. A picture of the tunnel with a hot-wire probe held directly in the indexing head is shown in Fig. 2.

The probes used held single-wire tungsten elements. The .00015-in. dia.,.040-in. long wires were positioned with their long axis perpendicular to the tunnel axis yielding the mean, $\bar{U}$, and fluctuating, u, components of velocity in the axial direction. The frequency response of the hot-wire system, as measured by the square wave technique, with a mean velocity of 15 fps was 30 kHz.

The signal from the wire was processed in the manner shown in the diagram in Fig. 3. The resulting data consisted of plots of the mean velocity, $\bar{U}$, the rms level of the fluctuating velocity u', versus radius, r, and axial (downstream) distance, x, from some reference point and of spectra of u at selected locations. The linearizer gain was set so that a 1.0 volt output corresponds to a velocity of 10.0 fps for all of the data presented in this report. Thus, rms voltage data can be converted to fps simply by multiplying by ten.

A band width of 10 Hz was used for all the spectral data presented unless otherwise noted. The low pass filter between the auxiliary unit and the X-Y plotter was used to damp oscillations in the writing pen during recordings of mean velocity profiles. The 10 kHz low pass filter in the auxiliary unit was employed to reduce electronic noise. The output from the DISA rms meter at low scale values was not linear. For this reason low end data were taken from the instrument meter rather than from the X-Y records.

The data which are not presented in the figures as X-Y records fall under one of the following categories:

a) Curves presented in the figures by continuous straight lines with no experimental points shown; these curves are obtained by drawing a best fit average to the X-Y records which are presented in another figure of the report (e.g., compare Fig. 18 with Figs. 15 and 16).

b) Curves presented in the figures as the best fit to experimental points shown on the same figure; these points are obtained by recording the output of the DVM or the rms volmeter directly rather than using the X-Y recorder (e.g., see Figs. 18 and 64).

c) The spectra of u; the records of the G.R. 1910-A wave analyzer are first recorded on the G.R. strip chart recorder which is coupled to the analyzer. The records are then averaged, replotted on the figures and connected by a continuous solid line (e.g., see Fig. 20).

CHAPTER III
DESCRIPTION OF TURBULENCE MANIPULATORS AND TEST CONDITIONS

In the present study a number of different flow elements are placed in the test section and their influence on the structure of the oncoming flow is studied. These different flow elements are referred to as "turbulence manipulators." Although the flow elements act on both the fluctuating and mean components of the flow, we deemed the term (originally proposed by M.V. Morkovin) appropriate since our primary interest, ultimately, is in the effect on turbulence. The manipulators considered include screens, plastic straws, perforated plates, porous foam, and combinations.

A. TURBULENCE MANIPULATORS

1. Screens

The screens used in the present study are made of 0.005-in. Dacron thread formed into a square mesh of approximately 30 pores per lineal inch (M = 0.033 in.). The solidity, σ, of this screen is 0.28, where the solidity is defined as the ratio between the solid area to the total area. The pressure drop coefficient, K, ($K = \Delta P/\frac{1}{2}\rho U_\infty^2$) for the range of Reynolds numbers considered is 0.86. A screen stretched across a test section flange is shown as item 7 in Fig. 4B.

2. Plastic Straws

Due to the high price of precision honeycomb materials available on the market, the packing of plastic drinking straws into a honeycomb-like matrix was suggested. After finding that the packing of straws is relatively simple even in large quantities, they were utilized extensively in this study and in general at I.I.T. The friction between the neighboring straws, when they are packed tightly, is sufficient to maintain their position, when used in air streams of low and moderate speeds (velocities up to approximately 60 fps are run at I.I.T.). When the straws are used in water it is found that they must be joined together along their outer walls using an adhesive material such as contact cement. Due to the low cost of adapting these plastic straw matrices, they are referred to often by us as the "Poor man's honeycomb." The inlet of a low-speed wind tunnel (2.5 x 9 ft.) was packed with approximately 120,000 plastic straws in a period of one day.

The straws used here have 0.175-in. outside diameter and 0.006-in. wall thickness. Lengths of 1 in., 3 in., 5 in. and 10 in. were tested. When packed tightly but without an appreciable distortion of their circular shape, the average number of straws per lineal inch is 5.7 $in.^{-1}$. The solidity, σ, of the resulting honeycomb structure is estimated to be 0.20. The pressure drop coefficient as a function of velocity over the range tested is shown in Fig. 5 for three straw lengths. An end view of a honeycomb matrix (item 8) and an angle view of a 3-in. long honeycomb matrix with a screen placed at the exit (item 9) are shown in Fig. 4B.

3. Perforated Plates

Three types of perforated plates are used, and are referred to as P.P. #1, P.P. #2 and P.P. #3. All the plates are standard stock punched steel plates with circular holes arranged in a hexagonal array. Because of the manner in which the plates are manufactured, one edge of the hole is sharp while the other is rounded. In spite of this, no influence of the plate orientation could be detected.

The geometrical characteristics of the three plates are tabulated in Fig. 6. The three types of plates cut to 3.2-in. diameter round discs in order to be used in the test section of the tunnel are shown in Fig. 4A, where P.P. #1, P.P. #2 and P.P. #3 are labeled 1, 2 and 3, correspondingly.

4. Porous Foam

Polyurethene foam supplied by Scott Company is used in the present study. The foam is made of 3% dense material (we estimate its solidity, σ, to be equal to 0.03; see bottom part of Fig. 4A) with 45 PPI (pores per lineal inch) nominal size (M = 0.022 in.). The pressure coefficient, K, for 0.25-in. thick foam of this type is equal to 6.6 at 15 fps mean flow velocity. An enlarged photograph of a thin section of the foam material is shown in Fig. 4A.

In order to use the foam in large cross sections under high dynamic loads without excessive deflection, a scheme of attaching the foam to one side of the perforated plates described above was devised. The plate is first sprayed with 3M Scotch Spra-Ment adhesive and then the foam is laid over it carefully without stretching it. The perforated plate with the foam attached is then placed on a flat surface and a flat plate and a large weight are placed above the foam. The plate is then left in this condition for approximately 12 hours in order for the adhesive to cure. Care must be taken in order that no relative motion in the radial direction between the perforated plate and the foam occurs. When the plate is removed it should be examined and cleaned of any excessive adhesive that may plug some of the holes of the perforated plate. Minimum amount of cleaning using a sharp edge, such as a sewing needle, is found necessary. The resulting turbulence manipulator is referred to as a porous foam plate. Foam thicknesses up to 1 in. have been joined to plates and tested in mean velocities up to 60 fps without any problems detected. Figure 4A shows two porous foam plates (items 4 and 5) utilizing P.P. #1 and P.P. #2, shown from their downstream side and upstream side, respectively. Data using both the foam separately and different porous foam plates are presented in Chapter IV.

The physical dimensions, the values of the mesh size, M, the solidity, σ, the pressure coefficient, K, and the Reynolds number based on mesh size, Re_M(= UM/ν), for the different turbulence manipulators are tabulated in Fig. 6. The values of Re_M and K listed are those corresponding to U_∞ = 15 fps.

B. TEST FLOW CONDITIONS

The work of Tsuji[13,14] reviewed earlier, has shown that the level and structure of turbulence in the flow upstream from a grid can have a pronounced effect on the decay of turbulence downstream from this grid. In many applications where the devices tested in the present work are used for turbulence reduction, the structure of the incoming flow may be largely unknown. At any rate the structure will vary from one application to another. For these reasons several different test flow conditions were employed in this work. In two of the conditions the turbulence level was moderately high but the source of the turbulence differed. A third condition possessed a fairly low level of turbulence. Finally, an incoming flow with a large inhomogeneity in the mean velocity profile (a wake flow) was constructed. These flow conditions are detailed in the following sections.

As described in Chapter II and in more detail in the Appendix, the entrance to the circular test section from the acoustic chamber (plenum chamber) consists of a smooth bellmouth. A screen, of the type described earlier in this chapter, is located at the downstream end of the bellmouth. The variable length, constant diameter test section is the location in the tunnel where the different test conditions are generated.

1. Test condition "A" with uniform mean velocity, $\bar{U}$, moderate turbulence intensity, u'/U_∞, and minimum control of upstream history

This test flow condition is the one existing in the circular duct at a large distance downstream of the test section entrance screen (made of the same type of screen described in part A-1 of this chapter; M = 0.033 in. and σ = 0.28). The turbulence manipulator to be investigated is located in the test section with its upstream end at a distance of 6 in. downstream from this screen, as shown in Fig. 7A. As indicated in the heading of this paragraph, flow condition "A" is intended to be somewhat representative

of turbulent flow fields present in numerous industrial applications. Despite the apparent uniformity of the axial mean velocity in some of these flow fields, the structure of turbulence is far from being isotropic or even stationary in them. In condition "A" the plenum chamber, the bellmouth entrance to the test section, and the screen located upstream of the turbulence manipulator represent the uncontrolled input parameters to the flow; in particular, to the turbulence. Therefore, the results obtained in this test flow condition should be interpreted with care. We believe, however, that in order to meet our objective of aiding the design engineer in his tasks of managing his turbulent flow fields, we should become aware of some of the peculiarities of the effects of the different turbulence manipulators on these flow fields and develop a better understanding of the mechanisms governing these effects.

The convenience offered by the tunnel used in the present study is an additional incentive for utilizing test flow condition "A." This convenience permitted us to examine the different passive devices, listed earlier in this chapter, in detail. In addition, other test flow conditions (B and C, in particular) where the turbulent flow was sufficiently controlled, as described below, were easily generated. It should be pointed out, however, that due to the small cross section of the tunnel test section, the data at large distances downstream of the device may be influenced by the growth of the side wall boundary layer. Data up to axial distances of 10 in. downstream of the different manipulators is presented in this report. No evidence of any noticeable influence of the side walls is seen in either the radial or the axial profiles (e.g., see the radial profiles at x = 6.5 in. of Fig. 70).

The origin of the coordinate system for the measurements in this test condition is located on the axis of the test section at the downstream end of the turbulence manipulator. Figure 8 shows a plot of the axial distribution of u'/U_∞ downstream from the test section entrance screen. The dashed line represents the average level of u'/U_∞ during the period when the present investigation was conducted. The other two curves indicate the upper and lower limits of u'/U_∞ across the test section and over a period of two years during which minor alterations in the tunnel were made.

A part of the variation is due to radial inhomogeneities in u' as shown in Fig. 9. It should be noted here, however, that the radial profiles of $\bar{U}$ and u'/U_∞ shown in Fig. 9 include the test section side wall boundary layer (left-hand side of the figure). These radial distributions are obtained at 6 in. downstream of the entrance screen for the case of U_∞ = 10 fps.

The average values of u'/U_∞ for different U_∞ are tabulated in the same figure. One of the peculiarities of test flow condition "A", referred to earlier, is the increase of u'/U_∞ with decreasing U_∞. This is not in agreement with experiments on grid-generated isotropic turbulence discussed in Corrsin's article[1], where u'/U_∞ is found to be independent of velocity at high Reynolds numbers Re_M. Spectra of u for this flow condition are in Fig.10.

2. Test condition "B" with uniform mean velocity, $\bar{U}$, and uniform low turbulence intensity, u'/U_∞

In this test flow condition a matrix of 1-in. long straws with a screen located at their downstream end is placed in the duct as shown in Fig. 7A. A distance of 11.5 in. is allowed for the flow to reach near equilibrium and for u'/U_∞ to reach a low level. Fig. 11 shows the decay of u'/U_∞ downstream of the 1-in. straws and screen. The value of u'/U_∞ is found to be equal to 0.015 at U_∞ = 15 fps. The turbulence manipulator to be examined is located in the test section with its upstream side 11.5 in. downstream from the straws and screen. The coordinate system for this test condition has its origin on the axis of the test section at the downstream end of the turbulence manipulator. Both $\bar{U}$ and u' are found to be uniform across the test section except in the boundary layer of the duct.

3. Test condition "C" with uniform mean velocity, $\bar{U}$, uniform moderate turbulence intensity, u'/U_∞, and controlled upstream history

This test flow condition was concocted when some of the results obtained in condition "A" were suspected to be influenced by the possible existence of secondary flows or swirls in the test section. (A detailed discussion of these results is given in Chapters IV and VI.) For this reason this condition was designed in order to eliminate the secondary flows and to generate a uniform moderate turbulence intensity of the same level as condition "A." As shown in Fig. 7B, 3-in. straws with a screen at their downstream end were placed in the test section. The straws are intended to break up any large scale eddies or swirls that may have penetrated the screen at the entrance of the test section. A perforated plate (P.P. #3) is placed at a distance of 4.5 in. downstream of the straws in order to generate the moderate intensity uniform turbulence. The turbulence manipulator examined in this condition is located with its upstream end at a distance of 2.38 in. downstream from the plate. When U_∞ = 15 fps the turbulence intensity level u'/U_∞ is equal to approximately 0.08 at the entrance of the turbulence manipulator (see Fig. 12). The radial distribution at this axial location of both $\bar{U}$ and u'/U_∞ is found to be uniform (e.g., see Figs. 37 & 38). The spectra of the axial component of the turbulence are shown in Fig. 13 for three different axial locations. One difference in the character of u' in comparison to condition "A" is the larger gradient of u'/U_∞ in the axial direction. This unfortunately could not be avoided in order to maintain the level of u'/U_∞ at the same value for both test flow conditions. The measurement coordinate system is located as usual in relation to the turbulence manipulator.

4. Test condition "D" with large mean flow nonuniformity and high turbulence intensity

The final test flow condition was designed to obtain a severe case of nonuniformity in the radial distribution of both the mean and fluctuating axial components of the velocity. A high level of turbulence was one of the objectives of this case. This test condition was generated to simulate in some sense a flow downstream from an obstacle one might encounter in a typical industrial application.

At a distance of 7.5 in. downstream from the test section entrance screen an obstacle was placed across the test section. This obstacle is made of the same perforated plate material used for P.P. #3. A 1.25-in. wide strip was cut from a 3.2-in. disc of this plate material (see Fig. 4, item 6). The obstacle is then placed in the test section in a nonsymmetric position with respect to its axis as shown in Fig. 7B. The different turbulence manipulators used for the management of the resulting flow field are placed at a distance ζ_o downstream from the obstacle (the distance ζ_o is varied with the different tests). The radial distribution of $\bar{U}$ and u'/U_∞ at two different axial locations downstream from the obstacle are shown in Fig. 14. The different turbulence manipulators are tested in the flow field given in these two figures and the usual measurement coordinate system is used.

Other special-purpose test flow conditions were engineered for different experiments during the course of the investigation. Two of these conditions are described on page 21 and are denoted by conditions "E" and "F". Additional ones are referred to on page 35.

CHAPTER IV

RESULTS

The experimental results presented in this chapter are organized in the following manner: First, the performance of single manipulators in flows of uniform mean velocity, condition "A", "B", and "C", is set forth; next, the effect of combinations of manipulators on the same uniform flows is documented; next, the action of selected individual and combined manipulators on a stream with a gross inhomogeneity in the axial mean velocity profile, condition "D", is recorded; finally, the effect of Reynolds number is examined.

A. SINGLE TURBULENCE MANIPULATORS

1. Screens

The action of single and multiple screens on grid-generated turbulence has been extensively studied by other investigators and was included in this work as a kind of benchmark. The flow variable of interest was the fluctuating velocity component, u, and its decay in the downstream direction. Sample records of the rms value of this variable, u', for flow conditions "A" and "B" are shown in Figs. 15 and 16, respectively. The large peak in u'/U_∞ and the subsequent rapid falloff within the first inch downstream from the screen is similar in both figures.

More details in this region are revealed in Fig. 17, in which the horizontal axis for condition "B" has been expanded by a factor of ten. The behavior in this initial region is associated with the detailed flow structure through the screen as evidenced by the nonhomogeneity in u'/U_∞. The curve marked "a" in Fig. 17, which shows an increase in u'/U_∞ for the first 0.2 in. behind the screen followed by a decrease, corresponds to a radial position of the hot-wire probe chosen so the mean velocity is near a maximum at the initial point in x (here $\bar{U}$ = 23 fps). The curve marked "b" was started with the probe near a minimum in $\bar{U}$. Due to the averaging effect of the hot-wire, the length of which is 1.33 times the screen mesh size, and the imprecision in maintaining exactly the same radial position throughout the entire axial traverse, these curves merely indicate trends and must not be taken literally.

The measured radial inhomogeneity of u' plus the details of the spectra of u in the near screen region indicate that the flow is certainly not homogeneous, isotropic turbulence but rather some mixture of modified upstream turbulence plus newly emerging velocity fluctuations associated with instabilities in the screen wake shear layers. Curves "a" and "b" merge together beyond x = 0.5 in. Downstream of x = 1 in. the development of u' differs between conditions "A" and "B", Figs. 15 and 16. In condition "A", u' rises slightly and then remains almost constant to x = 10 in. while for condition "B", u' continues to fall, but at a slower rate. To investigate whether this behavior is due to the level of incoming turbulence, a single screen was tested in condition "C" at a point where the intensity u'/U_∞ was approximately the same as in condition "A" but the structure of turbulence was in some sense different from that of condition "A" (for details see Chapter III). The downstream development of u' behind the screen in this condition is similar to that of Fig. 16, condition "B", in that u' continues to fall downstream of x = 1 in. A comparison of the three cases, flow conditions "A", "B" and "C", is shown in Fig. 18.

Some evidence of the difference in the structure of u' in the flow behind single screens for the three flow conditions is contained in Figs. 19, 20 and 21, which show the spectra of u at several axial locations. In Fig. 20, for condition "B" with a low level of incoming turbulence, the near screen detailed structure is revealed. The spectral peaks at 800, 1500, 1800 and 1900 Hz for small x are not unique in the sense that the relative magnitudes, and even the frequencies at which the peaks occur, depend on the radial location of the probe, but the uniform decay of the low frequency components is consistent. In contrast, for condition "A" in Fig. 19, the low frequency content is seen to increase in absolute magnitude beyond x = 1 in., while for condition "C", Fig. 21, with

higher level of incoming turbulence the spectral peaks at high frequency cannot be identified at x = 1.5 in.; compare with curve "d" of Fig. 20 at the same x. However, low frequency spectral peaks (large scale eddies) can be detected (see top curve of Fig. 21).

2. Straws

Because of their large mesh size more detail near the exit plane of the straws can be resolved with the hot-wire than was the case for the screens. In particular, the mean velocity profiles of the jets issuing from the individual straws are clearly measured at x = 0.1 in. as shown in Figs. 22 and 23 for 1-in. and 3-in. long straws, respectively. All straw tests were run in flow condition "A". Due to the packing imperfections of the straw matrix, a horizontal traverse with the hot-wire cut across only a few of the straws sufficiently close to the centerline to indicate the maximum velocity. Even so, the difference in the development of the velocity profiles within the straws due to the difference in development length (1 in. to 3 in.) is clear (compare shape of profiles and maximum straw centerline velocity at x = 0.1 in.). Similar profiles with straw exit centerline velocity up to about 36 fps for 10-in. long straws were measured by Hannemann[57] but are not reproduced here. If the solidity of the straws matrix is corrected for, the fully developed centerline velocity within each straw is estimated to be 35 fps. The length of the 10-in. straws is also estimated to be almost adequate for reaching fully developed laminar flow for U_∞ = 15 fps.

Radial profiles of u' for the two cases are shown in Fig. 24. The jet-like structure of the mean velocity profiles, Figs. 22 and 23, has essentially disappeared by x = 2.0 in. and only for the 3-in. long straws does there remain any evidence of the structure in the u' profiles at x = 2.0. in. The streamwise profiles of u' for the three lengths of straws tested are shown in Fig. 25. Also shown is the profile of u' for the tunnel with the straws absent (flow condition "A"). As in the case of the screen, the inhomogeneity in u' in the near wake of the straws precludes the characterization of u' versus x by a unique curve (e.g., the data points shown from x = 0.2 in. up to x = 2.0 in. for the 3-in. long straws are simply typical values obtained from one traverse). In general, for the straws, at any radial location u' increases with x, reaches a peak and then decreases again (see Fig. 24). The peak occurs at nearly the same axial distance for any radial location. Two features of Fig. 25 should be noted: first, the level of u' far downstream and at the saturation peak increases with increasing straw length; second, the location of the peak in u' moves downstream with increasing straw length.

The spectra of u at several downstream stations for the 1-in. and 3-in. straws are shown in Figs. 26 and 27, respectively. In Fig. 26, the locations marked f_1^*, f_3^*, and f_{10}^* indicate the frequency at which the spectral peaks occur for the 1-, 3-, and 10-in. long straws, respectively, when measured near the straw exit plane (e.g., at x_1 = 0.6 in.) The characteristic frequencies, f_ℓ^*, were clearly visible on the oscilloscope screen when the hot-wire output in the region of the ascending portions of the curves of Fig. 25 was displayed. The frequency f_ℓ^* was found to be insensitive to the radial position in contrast to the spectral peaks behind the screens.

An interesting composite plot is presented in Fig. 28. Shown are plots, which were recorded from two consecutive traverses, of the mean velocity $\bar{U}$ and the turbulence intensity u'/U_∞ versus x for a probe initially positioned at the center of the exiting jet from a 10-in. long straw. The mean velocity drops rapidly from a maximum of about 37 fps at the straw exit reaching the mean value of about 16 fps just downstream from the peak in u'. This figure illustrates the dramatic mixing which occurs within the first 2½-in. downstream of the straws exit plane and the subsequent decay of the wake-generated turbulence in the region of uniform mean velocity. It should be pointed out that due to the attenuation setting used on the rms meter, in order to capture the peak in u'/U_∞, the values presented in the plot at large x are not accurate.

For the 10-in. straws inhomogeneities in u' seem to persist farther downstream

than for the shorter straws. Two axial profiles of u'/U_∞ at different radial locations are shown in Fig. 29. The initial rapid falloff of u' from the peak is similar in both cases; however, the decay rates beyond x = 3.0 in. and up to x = 8.0 in. are somewhat different.

3. Perforated Plates

All three plates were tested initially under flow condition "A". The mean velocity profiles of plates #1, #2 and #3 are shown in Figs. 30, 31 and 32, respectively. Figure 30 shows the strong jets, at x = 0.1 in., issuing from the holes in the high solidity plate #1 (σ = 0.7). Two consecutive radial traverses were made at x = 0.5 in. to indicate the reproducibility of the kinks in the profile at this point. Of special note here is the hairy region at the extreme right of the profile. This feature persists even after the remainder of the profile has smoothed out at x = 2.0 in. This anomalous behavior was noted only downstream of plate #1. The development of the velocity profiles behind plates #2 and #3 (Figs. 31 and 32) show a more uniform approach to the average velocity. The depressed region near the center of the traverse at x = 0.1 in. in Fig. 31 was caused when the hot-wire probe moved in a radial direction normal to the line of traverse from a region near the holes centers to a region between holes. Figure 33 shows the radial profiles of u'/U_∞ corresponding to Figs. 30, 31 and 32 for P.P. #1, P.P. #2 and P.P. #3. Although P.P. #1 has the smallest mesh, and P.P. #3 has the largest, it is to be noted that when compared at x = 2.0 in., P.P. #3 yields the most uniform u' distribution of all three plates and P.P. #1 yields large nonhomogeneities which are found to persist in x.

The axial profiles of u'/U_∞ for P.P. #1, P.P. #2 and P.P. #3 are shown in Figs. 34, 35 and 36, respectively. The traverses of Figs. 34 and 35 were initiated near x = 0 at a plate hole centerline. A high $\overline{U}$ reading was used to center the probe with the hole for P.P. #1 and due to the large size holes of P.P. #2, we were able to position the probe by aligning it visually in Fig. 35.

The holes in plate #3 were large enough so the hot-wire prongs could be extended through it for upstream measurements. Curve "a" in Fig. 36, which starts upstream of the plate, is a profile in line with a hole, while curve "b" is a profile which begins with the hot-wire positioned between two holes at an axial location just downstream of x = 0. Again the rapid increase in u' in the near exit plane region, the saturation, and the rapid decay are evident.

In order to obtain more details of the structure of the turbulence generated by the plates, plate #3 was tested with a low level incoming turbulence (condition "B"). The resulting mean velocity profiles for this case are shown in Fig. 37. The jet-like profiles at x = 0.1 in. are slightly more sharply defined than for the corresponding location in test flow condition "A" (Fig. 32). The profiles farther downstream are markedly different, showing a slower mixing under flow condition "B". The radial profiles of u'/U_∞, Fig. 38, also indicate noticeable nonuniformities as far downstream as x = 2.0 in. Note the two separate u' peaks associated with the jet shear layer at x = 1.0 in.

The spectra of u, for P.P. #3 in conditions "A" and "B" are shown in Figs. 39 and 40. The absence of high "background" turbulence in condition "B", particularly at the lower frequencies, reveals more of the structure of the plate-generated turbulence. In particular, the growth of the peak near 850 Hz between x = 0.2 in. and x = 0.5 in. which is quite clear in Fig. 40 is masked in Fig. 39. Also, while little growth in the low frequency content is evident in Fig. 40, considerable growth and/or transformation of high frequency energy into apparent low frequency u content is observed in Fig. 39 for the condition "A" flow.

The axial profile of u'/U_∞ for condition "B" is shown in Fig. 41. The major peak has been clipped because the input exceeded the limit of the scale being used on the rms meter. The smaller peak just upstream from the plate exit plane was traced to nonuniform probe traversing through a region of a high velocity gradient. A plot of that portion of

the u' profile with both the horizontal and vertical axes expanded is shown in Fig. 42 together with the mean velocity profile in the axial direction. As the air approaches a hole in the plate the velocity increases rapidly, continues to increase through the hole and reaches a maximum somewhat downstream of the exit plane. The apparent decrease in $\bar{U}$ from x = -0.7 to x = -0.2 is believed to be caused by the probe-stem blockage of the perforated plate hole. The small peak in the u'/U_∞ profile occurs at the point where the rate of change of $\bar{U}$ with x is maximum. This peak was not apparent, however, when the probe was slowly traversed manually, but only occurred when the probe was moved by the stepper-motor of the DISA traversing mechanism. During this manual traverse a small decrease in u' was measured as the hot-wire entered the hole from the upstream side. The level of u' continued to decrease until the wire was at the exit of the hole and then increased as in Fig. 42.

4. Porous Foam

The flow downstream from the 1/4-in. foam was measured for flow condition "A". Traversing for these measurements was done manually and the data was recorded at discrete points. The mean velocity profiles in the radial direction for several axial locations are shown in Fig. 43. Although no apparent nonuniformity in the thickness was visible in the foam slab used and the foam structure is believed to be regular (see bottom part of Fig. 4A), considerable irregularity is evident in the mean velocity downstream of the foam. The deviations from U_∞ near the foam are not as large as near the exit plane of the perforated plates, e.g., compare to Fig. 32; however, they seem to persist farther downstream for the foam.

The radial profiles of u'/U_∞, Fig. 44, also show considerable nonhomogeneity which decreases rather slowly. The decay of u' in the axial direction is shown in Fig. 45 for a single traverse. The flat portion of the curve around x = 2 in. may be due to slight radial misalignment of the probe as it is moved axially causing it to move from a radial region of relatively low u' to one of high u'. No increase in the average radial level of u'/U_∞ can be detected between axial locations for which radial u'/U_∞ traverses were made; see Fig. 44.

B. COMBINATIONS OF TURBULENCE MANIPULATORS

1. Multiple Screens

In order to facilitate a comparison among the various manipulators on an equal pressure drop basis, several arrays of multiple screens were examined. One of the first questions which arose in setting up this test was: "What is the sensitivity of the overall u' reduction ratio, F_{1n}, to the screens separation distance?" Since it was most convenient to use small separations between screens, Δx from 0.31 in. to 0.5 in., an initial test was run to compare the u' levels far downstream from two screens separated first by Δx = 0.31 in. and then by Δx = 1.0 in. in test flow condition "A". The axial profiles of u'/U_∞ for the two separations are shown in Fig. 46. The only difference discernible is in the first 0.5 in., which can be attributed to the near screen inhomogeneity documented in Fig. 17.

In the subsequent tests with three and seven screens placed in series, the screens separations ranged between 0.31 and 0.62 in. The axial u'/U_∞ profiles for three and seven screens in series are presented in Fig. 47. The general shape of these curves is similar to that of a single screen in flow condition "A" (compare to Fig. 15), but the u' level far downstream decreases as the number of screens increases. This aspect is discussed in Chapter VI.

2. Straws Plus Screen

In order to test a hypothesis that the straw wake instability could be modified by altering the velocity profiles of the jets issuing from the exit plane, a series of experiments were conducted with a single screen stretched across the downstream face of

the straws matrix (see item 9 in Fig. 4B).

Typical axial traverses of u'/U_∞ for the 1-in. and 3-in. straws plus screen are shown in Figs. 48 and 49, respectively. A composite plot of u'/U_∞ versus x for 1-in., 3-in. and 10-in. straws with a single screen at the exit plane of each straw bundle is presented in Fig. 50. The profile of u'/U_∞ for the 10-in. straws alone, from Fig. 25, is included for reference. The three outstanding effects of the screen evident from these curves are: the increased reduction ratio of u', F_1, for all three straw lengths beyond $x \approx 1.0$ in.; the shifting of the saturation peaks in u' nearer to the straw exit plane; and the almost complete loss of influence of the straws length on the u'/U_∞ profiles.

The mean velocity profiles in the radial direction for the 3-in. straws plus screen are shown in Fig. 51. Even as close as $x = 0.1$ in. the jet-like profile on the scale of the straw diameter, seen in the absence of the screen (Fig. 23), is almost totally obscured by smaller scale irregularities due to the screen wake. The radial u'/U_∞ profiles, Fig. 52, at $x = 0.5$ in. and $x = 1.5$ in. are similar in shape to the u'/U_∞ profiles for the 3-in. straws alone at $x = 1.5$ and $x = 2.0$ in. (Fig. 24) but at a lower level. Two consecutive traverses at $x = 0.5$ in. are shown in Fig. 52 to give some indication of the stationarity of the u' profiles.

Spectra of u were taken at several axial stations downstream from the 1-in. straws with a screen at their exit. These spectra, Fig. 53, reveal two characteristic frequencies, one at 1650 Hz and one at 1175 Hz. Neither of these frequencies correspond to the peaks in the spectra for the straws alone (Fig. 26) or the screen alone (Fig. 20).

Two axial u'/U_∞ profiles obtained from consecutive traverses made downstream from the 10-in. straws with a screen at their exit plane are presented in Fig. 54. To record the curve marked "a" the hot-wire probe was started, near $x = 0$, in a region of low mean velocity, $\bar{U}$. Prior to making the traverse marked "b" the hot-wire probe was moved radially, near $x = 0$, to a region of high mean velocity, $\bar{U}$. Two different saturation peaks are seen in curve "a"; one sharp spike at $x \approx 0.15$ in. followed by a lower maxima at $x \approx 0.6$ in. For curve "b" only one peak, at $x \approx 0.4$ in., is evident. The difference between the two curves gradually decreases and they finally merge near $x = 10.0$ in.

One last series of experiments was performed to investigate the influence of the straw-screen separation distance, Δx, on the downstream u'/U_∞ level. Two typical decay curves for $\Delta x = 0.375$ in. and $\Delta x = 1.375$ in. are shown in Fig. 55. The abscissa for this figure is $x + \Delta x$, which is a measure of the distance downstream from the straw exit plane since x is measured from the screen location. For these two separation distances, u' is lower for $\Delta x = 0.375$ in. than u' for $\Delta x = 1.375$ in. when both are compared at any $x + \Delta x$ or at any x. A composite plot of u'/U_∞ versus $x + \Delta x$ for these and several other values of Δx, Fig. 56, shows that the optimum location for the screen in order to achieve low u' levels downstream, and thus higher turbulence reduction ratios, F_1, is upstream from the peak in u'/U_∞ of the straws alone.

3. Perforated Plate Plus Screen

In light of the dramatic effect of screens on the downstream development of u' behind straws, a similar series of experiments was conducted with a screen against the downstream face of perforated plate #3. Both flow conditions "A" and "B" were employed. The radial profiles of the mean velocity, $\bar{U}$, for conditions "A" and "B" are shown in Figs. 57 and 58, respectively. In both cases at $x = 0.1$ in. the major jet pattern of the plate holes is somewhat obscured by the screen wake, but it remains distinguishable. (Contrast with Figs. 32 and 37 for the plate alone.) By the axial position $x = 0.5$ in., the basic plate pattern has re-emerged and subsequently decays more slowly than in the case of the plate alone.

The radial profiles of u'/U_∞ for the two flow conditions "A" and "B", Fig. 59, are more irregular than their counterparts for the plates alone, Figs. 33 and 38 (with the exception of plate #3 alone in flow condition "B" at $x = 1.0$ in.). The smoothing of these

profiles is also much slower with the screen than without it. In fact, the difference between the radial minimum and maximum in u' appears greater at x = 2.0 in. than at x = 1.0 in. for flow condition "B". The axial profile of u'/U_∞, Fig. 60, for flow condition "A" when compared to that for the plate alone reveals a substantial attenuation, due to the screen, of the saturation peak of the plate alone, at $x \simeq 1.0$ in., but only a slight decrease in u' at x = 10.0 in. is distinguishable. A similar comparison for flow condition "B", Figs. 61 and 41, shows a comparable attenuation of the peak along with a more significant decrease in u' at x = 10.0 in. for the plate with a screen. More recent results, to be reported in detail in the near future, prove that the screen can be much more effective if a separation distance, Δx, of 0.125 in. is allowed between the plate and the screen. While other separation distances (Δx = 0.125, 0.25 and 0.375 in.) were examined and proved successful, the value of Δx = 0.125 in. appeared to be the optimum value for P.P. #3. The improvement in the u'/U_∞ level at x = 10.0 in. due to the screen at this separation distance (approximately 1/2 the plate hole diameter) is comparable to that of the straws plus screen (see Figs. 25 and 50),

4. Porous Foam Plates

Plates #1 and #2 were tested with a layer of 1/4 in. foam attached to their downstream surfaces under flow condition "A". (See Chapter III for detailed description.) The radial mean velocity profiles for plate #2 plus foam are shown in Fig. 62. The average velocity, U_∞, dropped slowly during this series of traverses from 15 fps during the traverse at x = 0.1 in. to 11 fps for the traverse at x = 6.5 in. due to a malfunction of the supply air compressor. The obliteration of the jet-like structure downstream from plate #2 alone, shown in Fig. 31, is almost complete at x = 0.1 in. A certain amount of waviness in the mean velocity profile is still apparent, however, as far downstream as x = 6.5 in.

The inhomogeneity in the flow is more graphic in the radial profiles of u'/U_∞, Fig. 63. The reproducibility of the repeated traverse at x = 6.0 in. indicates the stationarity of this phenomenon. All of the data recorded in Fig. 63 were obtained with U_∞ = 11 fps. Nonuniformity in the mean flow is even more evident with plate #1 plus foam. The mean velocity profiles for this case, Fig. 64, show a 50% variation as far as 6.0 in. downstream from the exit plane. The data of Figs. 64 and 65 were all taken with U_∞ = 15 fps. The radial u'/U_∞ profiles, Fig. 65, for plate #1 plus foam, shows a low but nonuniform level at x = 6.0 in.

Axial profiles of u'/U_∞ for plate #2 plus foam, Fig. 66, and for plate #1 plus foam, Fig. 67, indicate little change in level beyond x = 6.0 in. This is particularly remarkable for plate #1 plus foam, where the two profiles, corresponding to different radial positions of the same plate and at the same operating conditions, differ in level by a factor of three. For the lower curve in Fig. 67 the mean velocity, $\bar{U}$, at x = 10.0 in. was 13.3 fps while for the upper curve it was 15 fps.

C. AN EXERCISE TEST CASE

In all of the previous experiments the turbulence manipulators were tested in flows with uniform mean velocities. The essential questions to be answered were: "How do the various devices alter the level and structure of the incoming turbulence?" and "How rapidly do the perturbations, introduced in the mean velocity by the devices themselves, die out?" This last series of experiments was performed to see how effectively a flow with gross defect in mean velocity and considerable variation in u' could be homogenized and converted to a uniform stream of low turbulence intensity. Candidate devices for these experiments were selected subjectively on the basis of their performance in uniform streams (the results from test flow conditions "A", "B" and "C" shown in Figs. 15 through 67) without regard to pressure drop or size. The incoming flow condition for the following experiments is documented in Fig. 14 of Chapter III.

The first manipulator tested was perforated plate #3. This plate was positioned 1-1/2 in. downstream from the obstacle, i.e., ζ_o = 1.5 in. Radial traverses of $\bar{U}$ and

u'/U_∞ at several axial stations, Fig. 68, show relatively flat profiles at x = 2.5 in. but a high level of u'/U_∞. The location x = 1.5 in. shown in Fig. 68 is the same distance from the obstacle as the location ζ = 3.0 in. in Fig. 14. To reduce the level of u' a bundle of 3-in. straws was added 1 in. downstream from the previous perforated plate yielding the profiles shown in Fig. 69. For this run $\zeta_o + \ell$ = 5.5 in. so that the position x = 4.0 in. is 9.5 in. downstream from the obstacle (i.e., x = 4.0 in. corresponds to ζ = 9.5 in.). The profiles are flat and the level of u' is low although no data for the plate alone were taken at comparable ζ. The addition of a screen, at the straw exit plane, results in an even lower u' level, Fig. 70. Finally the perforated plate upstream from the straws and screen was removed ($\zeta_o + \ell$ remains equal to 5.5 in., resulting in the profiles of Fig. 71. The mixing provided by the plate, which helped in uniformizing the gross inhomogeneities, is particularly clear when Fig. 71 is compared to Fig. 70. Figures 68-71 illustrate the type of information obtained from comparisons of various devices in the test case "D". Additional results are discussed in section 7 of Chapter VI.

D. EFFECT OF REYNOLDS NUMBER

The essential feature of settling chambers of wind tunnels is the low flow velocity within the chamber. In turn, this results in relatively large decay times and minimal pressure drops across the turbulence reduction devices that are usually found in these chambers. With the exception of supersonic tunnels, the flow velocity in settling chambers is usually around 15 fps. For this reason, the majority of our studies have been carried out at similar speeds. As indicated in the following, a few of the manipulators were examined over the relatively wide range of free-stream velocities from 5 to 40 fps.

Perforated plates #1 and #3 were tested in the high-speed section of the I.I.T. environmental wind tunnel. The tunnel operates in the closed return mode and the test section has a cross section 2 ft. x 3 ft., 10 ft. long. A series of damping screens followed by a settling chamber and a 4:1 contraction section are located upstream of the high-speed test section. Free-stream velocities up to 200 fps can be achieved in this test section. The perforated plates were cut to the size of the cross section and were supported in the test section by the tunnel side walls.

The same hot-wire probes and instrumentation were used as described in Chapter II. The probes were mounted in the tunnel automatic traversing mechanism, which is driven by variable-speed d.c. motors and permits streamwise or transverse (vertical) traverses. Similar techniques to those described in Chapter II were used to collect the data. Both the mean velocity, $\overline{U}$, and the fluctuating velocity, u', were recorded simultaneously during the axial traverses along the tunnel centerline from x = 0 to x = 10.0 in. Spectra of u at different x positions were also obtained for various values of U_∞.

Two flow conditions were used to test P.P. #1 and P.P. #3. The first was the tunnel free-stream which will be referred to as test flow condition "E". According to the carefully performed measurements of Yung[58] the turbulence intensity in the free-stream of the tunnel at the test position is estimated to be 0.08% for the range of velocity utilized here. (For details of the measurement technique used in this low turbulence flow, see Nagib and Way[59].) The second test flow condition was that of a grid-generated turbulence and will be referred to as test flow condition "F". A section of P.P. #3 which spanned the entrance to the tunnel test section was used as the grid. The level of the generated turbulence intensity, u'/U_∞, at the manipulator test position was approximately 5%.

Additional experiments dealing with the effect of Reynolds number were performed in the tunnel described in Chapter II and the Appendix using a different laboratory air supply, which permitted tests over a larger range of speeds, i.e., from 5 to 25 fps. These tests involved the same screen used in sections A and B of this chapter and 5- and 10-in. honeycomb-like straw matrices.

Supplementary information was obtained by Tan-atichat[60] for P.P. #3, 2-in. strawbanks and 2-in. honeycomb sections (1/16-in. mesh hexagonal cross section made of aluminum)

in addition to other manipulators. The experiments of Tan-atichat[60] were performed in a small water tunnel over a free-stream velocity range from 0.5 to 1.5 fps. Although the water tunnel used by him has a smaller test section, its design features are quite similar to those of the tunnel employed extensively in this investigation.

1. Turbulence Reduction

The axial profiles of u'/U_∞ for P.P. #1 which were obtained for all velocities tested in condition "F" resemble the profile shown in Fig. 34. The u' peak, the rapid growth up to $x \simeq 1.0$ in. and the subsequent slow turbulence decay were all observed. The regular instability character was also noted on the oscilloscope, particularly during the portion of the traverse corresponding to the rising part of the u' peak. As the probe approached the position of the peak the signal became more random. Finally, the regular instability patterns became undiscernible from the oscilloscope traces at streamwise positions downstream of the location of the peak. This behavior is quite general in all manipulators tested in this report and was confirmed repeatedly in the Reynolds number tests reported in this section.

An interesting result obtained from the data covers the turbulence level at the saturation peak in the axial profiles of u'/U_∞, which is denoted by $(u'/U_\infty)_{max}$. In the case of P.P. #1 in condition "F", $(u'/U_\infty)_{max}$ was observed to decrease from approximately 0.55 at U_∞ = 5 fps reaching a plateau of approximately 0.21 for the range of U_∞ from 16 to 22 fps. Then $(u'/U_\infty)_{max}$ increased to 0.24 at U_∞ = 25 fps and finally decreased to approximately 0.1 at U_∞ = 35 fps. These results point to a possible change of flow regime downstream of the plate as the velocity is increased. The axial profiles of u'/U_∞ downstream of the plate, from which these data were obtained, also indicate that the anomalous behavior of this high solidity plate is intensified near U_∞ = 15 fps. Pressure drop measurements across the plate obtained in test flow condition "A" (not reported in detail here) support this observation (for definition of $(u'/U_\infty)_{max}$ see schematic diagram on page 28).

The present measurements are by no means adequate in order to make any conclusions regarding the dependence of the anomalous behavior, which is present downstream of high solidity devices, on Reynolds number. One can, however, surmise that this anomalous instability may only be present beyond a certain Reynolds number which may depend on the solidity of the device, its mesh and the incoming turbulence.

When P.P. #1 was tested in condition "E" similar observations and data were obtained. However, the level of u'/U_∞, including that at the saturation peak, was consistently lower for this flow condition than for condition "F".

As described in section A-3 of this chapter, the hot-wire probes used were sufficiently small to permit traverses through the holes of P.P. #3. The axial traverses for P.P. #3 in the experiments performed in the I.I.T. environmental wind tunnel were initiated approximately at x = -1.0 in. as in Figs. 36, 41 and 42. All main features of the instability, its growth and randomization and the decay of the turbulence generated remained identifiable over the entire range of velocities, $5 < U_\infty < 40$ fps. The axial profiles of u'/U_∞ obtained for conditions "E" and "F" were similar in shape to those in Figs. 41 and 36, respectively.

Some of the values of $(u'/U_\infty)_{max}$ obtained from the axial profiles for both flow condition "E" and "F" are:

U_∞ - FPS	5	10	15	20	25	30	35
$(u'/U_\infty)_{max}$ CONDITION (E)	0.34	0.22	0.18	0.15	0.12	0.12	0.12
$(u'/U_\infty)_{max}$ CONDITION (F)	0.38	0.29	0.24	0.22	0.22	0.22	0.22

The turbulence reduction factor, F_1, was also calculated from the axial u'/U_∞ profiles for all free-stream velocities in which P.P. #3 was tested. The downstream operational boundary used for these calculations was x = 10.0 in. As would be expected, F_1 was found to be larger than unity for test condition "E". Thus, it may be more appropriate to refer to F_1 in this case as the turbulence generation factor. However, F_1 was found to be essentially constant in condition "E" for all free-stream velocities.

The values of F_1 for condition "F" were considerably smaller than unity and were also found to be independent of velocity. For free-stream velocities from 5 fps to 40 fps the value of F_1 was approximately 0.25 in this test flow condition.

A most interesting phenomenon occurred when the velocity in the tunnel was increased beyond 30 fps while P.P. #3 was located in position across the test section. A pure tone of sound which increased its intensity and pitch with increasing velocity was clearly audible outside the tunnel. Some of the hot-wire and microphone measurements of this generated sound are reported in the following section in addition to the spectral information regarding the shear layers instability of the manipulators.

2. Instability and Generated Sound

Narrow-band spectral peaks similar to those in Figs. 26, 27, 39 and 40 were recorded in the numerous spectra which were measured during the experiments reported in this section. The common feature among the different manipulators is the increase of the frequency of the instability as U_∞ is increased. The following tables summarize the results from two manipulators, which are representative of the data obtained. The spectra of u from which the data of f*, presented in this section, is obtained were recorded at the x position where $u'/U_\infty \approx 0.5\ (u'/U_\infty)_{max}$ on the upstream side of the peak measured in the axial profiles of u' .

a) P.P. #3 in condition "E"

U_∞ - FPS	7.5	10	15	20	25	30	36
f^* - kHz	0.85	1.0	1.3	1.75	2.25	3.0	4.1

b) 10-in. straws in condition "A"

U_∞ - FPS	5	8	10	10.6	11.5	12.5	13.5	14	15	15.8	16.5	18	20	22	25
f^* - kHz	0.13	0.34	0.48	0 60	0.65	0.65	0.65	0.65	0.80	0.84	0.96	1.08	1.24	1.45	1.6

In the case of P.P. #3 additional spectral peaks were recorded by the hot-wire when the free-stream velocity was increased beyond 30 fps and the "singing" of the plate occurred. For example, narrow-band peaks at 3000, 7900, 8200, 8500 and 9450 Hz were easily identified in the hot-wire spectra for U_∞ = 36 fps. A microphone connected to a sound level recorder was then placed outside the tunnel test section and the output of the recorder was analyzed by the spectrum analyzer. When the free-stream speed was equal to 36 fps spectral peaks at 8200 and 8500 Hz were identified from the output of the analyzer. The corresponding hot-wire spectra, referred to above, displayed the highest amplitude for the peaks at 3000, 8200 and 8500 Hz.

The present measurements and those obtained by Tan-atichat[60] indicate that the position of the u' peak in the streamwise direction is insensitive to changes in free-stream velocity, U_∞, for P.P. #3. In the case of the straw-banks (5- and 10-in. straws in the present measurements and 2-in. in Tan-atichat's experiments[60]) the position of the u' peak

moved upstream and u'_{max} increased as the free-stream velocity, U_∞, was increased.

Tan-atichat[60] also reports that the frequency of the instability for the 2-in. straws, f_2^*, at a free-stream velocity, U_∞, equal to 0.88 fps is approximately 75 Hz. However, his measurements were performed in water. For the ambient temperatures in the present experiments and those performed by Tan-atichat[60] we need to multiply the speed in water by approximately 15 to arrive at the equivalent speed in air so that the corresponding f_2^* for 2-in. straws in air would be approximately 1150 Hz at free-stream velocity, U_∞, of approximately 13 fps.

A noteworthy observation occurred during the experiments with the "singing plate," i.e., P.P. #3 at $U_\infty > 30$ fps. When an object, such as a person's hand, was placed downstream of the perforated plate at axial distances, x, of approximately 1.0 in. to 4.0 in. and the object was moved in the transverse direction in a random paddling-like motion sufficient to disturb the flow field in the near-downstream of the plate, the singing disappeared. At no time during the motion of the object did one need to touch the perforated plate in order to stop the singing. When the experiment was repeated with the object at axial distances larger than approximately 5 in. no effect on the frequency or level of the sound generated by the plate could be heard.

CHAPTER V
HYDROGEN-BUBBLES FLOW VISUALIZATION OF MANIPULATOR MECHANISMS

In order to gain more insight into the basic mechanisms associated with the turbulence manipulators and to aid in the interpretation of the hot-wire measurements, flow visualization was utilized in the present investigation. Due to the expected complexity of the flow fields to be studied, hydrogen-bubble flow visualization in water was selected. This technique offers a degree of control and resolution not easily obtained with smoke or other visualization methods used in air. An open top water channel available in the Fluid Mechanics Laboratory at I.I.T. (supplied by the Techquipment Company of England) was selected for these flow visualization studies.

The test section is 3 inches wide, 6 inches deep, 15 feet long and is made of 3/8-inch clear plexiglas. A gate at the downstream end of the channel is used to control the depth of the flow in the test section. The flow, which is recirculated by a centrifugal pump, enters the test section from a large settling tank through a contraction section. The flow rate is controlled by a valve located downstream from the pump but upstream of the settling tank. The flow rate is measured by weighing the test section effluent.

When the flow was first visualized in the test section a high level of turbulence and some secondary flow near the entrance were observed. Two honeycomb sections (1/16-in. mesh hexagonal cross section made of aluminum) were cut to the size of the cross section of the channel. The first section, 2 in. long, was placed at the entrance to the channel (downstream from the contraction) and the second section, 1 in. long, was located 1.5 ft. downstream from the first. The manipulators were then tested at a position 30 in. downstream from the second honeycomb. The hydrogen bubble wires were fixed in their position by stretching them across the channel and holding them with Scotch adhesive tape. The wires were normally located at a height of 2 in. from the bottom of the channel. The mean velocity profile just upstream from the manipulators was uniform except for thin boundary layers near the walls and the turbulence level was low over the range of flow rates used in the tests. A mirror which can be adjusted in position and angle was placed on the top of the channel at eye level and was normally used at an angle of 45° to the horizontal to permit easy observation by the observers standing next to the channel.

The basic technique used in the hydrogen bubble visualization is well documented (e.g., see Schraub et al.[61]). The bubbles were generated along a .0015-in. diameter platinum-10% rhodium wire by applying a voltage potential, which was supplied by a specially built d.c. voltage source and pulser, between the wire and a downstream electrode made of stainless steel screen. The pulsed d.c. voltage generator was made to interrupt the bubble sheet at controlled intervals. The pulse lines thus obtained are actually time-lines. The mean velocity distributions can be inferred from the progressive distortion of these initially straight lines. The pulser consists of a low voltage power supply, a high voltage power supply and an astable multivibrator triggering a monostable multivibrator which triggers the high voltage output stage. The specifications of the pulsed d.c. voltage generator are:

	Minimum	Maximum
Pulse Width	0.20 sec.	30 sec.
Repetition Rate	.075 Hz	200 Hz
Output Voltage	0	500 Volts RMS

The bubbles were illuminated by Colortron Hi-Spot photo lamps placed at an angle of 120° from the viewing direction.

A Nikon 35mm SLR camera with a bellows attachment and 105mm lens was used with TRI-X black and white film which was pushed to ASA 1200 by developing it in Acufine. Overexposure of film and prints and the use of high contrast film, paper and chemicals is recommended.

High-speed movies of the flow field were recorded using a Beaulieu 4008 ZM Super 8 with a zoom lens. TRI-X Reversal black and white film gave the best results; the film was exposed at 70 frames per second with sufficient overexposure.

It should be noted here that for all the figures presented in this chapter, the flow is from right to left and for Figs. 72 through 76 and Fig. 79, the right-hand edge of the photographs is located approximately at x = 0. The fine, bright white line shown at the right of these figures marks the position of the hydrogen bubble wire. In Fig. 78, multiple wires were used and can be located on the photographs by the same bright white line. All the manipulators used here were machined to the size of the channel cross section and sealed around their circumference when tested.

A. FLOW DOWNSTREAM FROM TURBULENCE MANIPULATORS*

1. Straws

A honeycomb-like matrix, 10 in. long, made of plastic straws as described in Chapter III, was first examined. Figure 72 shows the flow immediately downstream from the honeycomb at two different free-stream velocities.

In the top photograph (Fig. 72a) the current through the wire was interrupted for a short period to give an indication of the mean velocity profiles emerging from the straws. This is shown by the dark tongues just downstream from the wire (compare to Fig. 23A). The regular structure farther downstream on Fig. 72a and the middle of Fig. 72b is a manifestation of the shear layer instability.

2. Straws Plus Screen

Figure 73 shows the flow under approximately the same condition as Fig. 72 except for the addition of a screen (same as one described in Chapter III) immediately downstream from the honeycomb. The screen was held tight against the honeycomb using masking tape around the edges of the honeycomb matrix. The effect of the screen on the scale of turbulence is remarkably clear when Figs. 72 and 73 are compared.

3. Perforated Plates

Photographs taken at progressively longer intervals after the initiation of a bubble sheet just downstream from P.P. #3 are shown in Figs. 74a through 74e. In Fig. 74b the wire was pulsed producing a time-line rather than a bubble sheet. The difference in displacement of the leading edge of the bubble sheets from the generating wire in Figs. 74a and b gives a qualitative indication of the mean velocity profiles in this region. (Compare to Fig. 32A and 37A.) Figures 74c and 74d show the development of the shear layers instability and Fig. 74e portrays the development of these instabilities to the ultimate turbulent flow.

The flow downstream of P.P. #1 is shown in Fig. 75a. The irregular behavior of this high solidity plate is shown by the bunching up of the small emerging jets into separate groups, each composed of several jets, and the existence of reversed flow (indicated by bubbles to the right of the wire).

A regular instability structure quite similar to that observed for the straws in Fig. 72 can be seen in the top right-hand side of Fig. 75b, which shows the flow downstream of P.P. #2.

The side view of Fig. 76a, which was taken through the plexiglas side of the channel, shows the three-dimensional nature of the instability downstream of P.P. #3. (The bright areas are the adhesive Scotch tape used to hold the bubble wire to the side of the channel.) Since the bubbles are generated in the horizontal plane and buoyancy effect is acting upward on the bubbles, the downward motion in this picture is a clear indication of this three-dimensionality. The instability was observed to be of a corkscrew shape for most manipulators.

---

*1 fps in water is equivalent to 14 fps in air for comparison between Chapters IV and V.

4. Porous Foam Plates

The relatively small scale and low intensity of the turbulence downstream of P.P. #3 + Foam is shown in Fig. 76b. It can also be observed that nonuniformities in the mean velocity appear to persist. Care must be taken in interpreting this photograph due to the integrating effect of the hydrogen bubble visualization technique. A persistent nonuniformity in the mean velocity causes the distortion of the time-lines (the lines passing through a family of bubbles generated at the same instant) to increase in proportion to the distance from the generation wire, while a time-line with frozen shape in time (or space) indicates a uniform velocity field.

B. FLOW THROUGH PARALLEL PLATES

In order to visualize the flow in the interior of a long honeycomb-type manipulator, the parallel plate device shown in Fig. 77 was constructed. (The plates are parallel and the curvature shown in the photograph is due to distortion by the camera lens.) The plates are made of 0.032-in. thick plexiglas and are cemented to a 0.25-in. thick plexiglas base at a mesh of 0.25 in. The manipulator length, ℓ, is 7 in. and the three spacers on the top are used to assure that the plates remain parallel at all times. The resulting solidity, σ, is approximately equal to that of the straw-banks. Three hydrogen bubble wires, just visible in the original photograph of Fig. 77, were stretched across the plates through specially machined holes at equal intervals along the manipulator length. The holes were located at a height of approximately 2 in. from the bottom of the channel. Each set of holes was located slightly lower than the set upstream of it to avoid the interference of bubble sheets from the different wires.

Figure 78a shows an overall view of this manipulator flow field indicating the turbulence on the upstream side, the damping of turbulence and the velocity profiles along the chord of the manipulator, and the generation of turbulence through the instability on the downstream side. The level of the incoming turbulence was artifically increased to 2% for this test by placing a section of P.P. #3 upstream from the parallel plates. A close-up shot of the entrance region to the parallel plates is shown in Fig. 78b. The bubble wire to the right is approximately two inches upstream from the plate and the wire in the center is 1/4 inch upstream from the plates. Some upstream influence can be identified but the major damping is achieved in the early section of the manipulator. The time-line in Fig. 79a gives a good qualitative indication of the velocity profiles emerging from this manipulator. The development of the shear layer instability is almost artistic in Figs. 79b and 79c and the subsequent development of turbulence is shown in Fig. 79d.

Records of the growth of the instability due to small disturbances on the upstream side of this manipulator when operating just near the critical Reynolds numbers, as well as flow conditions similar to those in Figs. 72 through 76, 78 and 79, are available on high-speed movies[62].

CHAPTER VI
DISCUSSION

The p ysical model of a manipulator outlined in the Introduction (viewed as a evice which operates by suppressing some of the incoming turbulence and generates urbulence) will be tested for consistency with the experimental results in this chapter. ne boundary of the device in an operational sense may extend beyond the physical boundary f the manipulator and, especially on the downstream side, is difficult to define. For our urposes we will define the incoming flow as that which exists in the test section at the eading edge of the manipulator in absence of the manipulator. The incoming flows are then haracterized by the data presented in Chapter III. The downstream boundary of the manipulator is considered, operationally, to be located at the station where the gradients in he streamwise direction of the mean and fluctuating velocities, $\partial\bar{U}/\partial x$ and $\partial u'/\partial x$, are pprox.ately equal to their value at the same station in absence of the manipulator. This efinition presents no ambiguities in the case of manipulation of turbulence where $\partial\bar{U}/\partial x$ s essentially zero at the boundary of the device. When we operate on nonuniformities of he mean flow we have to exercise personal judgment, just as Schubauer, et al.[2] did (for nstance, in their Fig. 15).

The turbulence reduction factors, F_i, are defined as the ratios of the effective u_i' at the inlet to the manipulator with the manipulator in place to the value of u_i' at the ame location in absence of the manipulator. The effective u_i' at the inlet (manipulator n place) is obtained by taking the value of u_i' at the operational downstream boundary of he manipulator and extrapolating back to the inlet using the decay curve of the turbulence n absence of the manipulator (see dotted lines in figure below). For the screens, this educes to the method used by Schubauer, Spangenberg and Klebanoff[2]. Utilizing the inlet is a reference point, manipulators of widely different characteristics can be compared on hree bases: efficacy in reducing the turbulence intensity, measured by the turbulence eduction factor, F_1; the pressure coefficient, K; and the effective length of the manipulator, ℓ_o. Shown below is a schematic representation of the axial u'/U_∞ profiles of hree different manipulators and that of the test flow condition in which they are placed (labeled as the free-stream). The three devices are of different physical lengths, ℓ, and exhibit different operational lengths, ℓ_o. The turbulence reduction factor, F_1, is defined n the figure and a graphical method of calculating it is outlined.

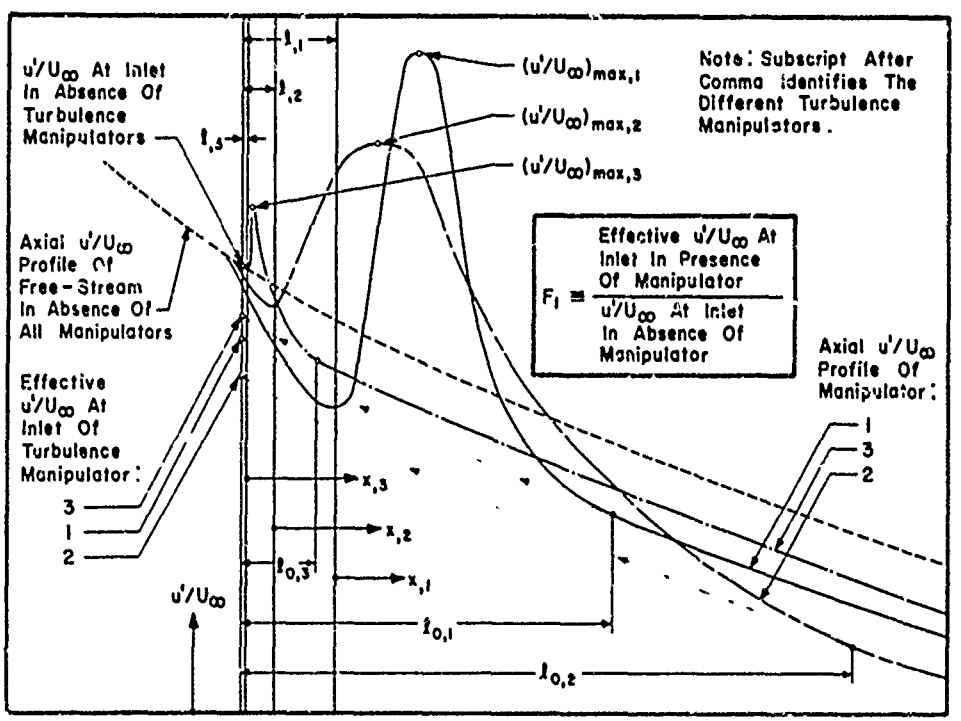

1) Suppression of Incoming Turbulence. Although no direct measurements of the damping mechanisms alone were made, qualitative information can be obtained from some of the hot-wire measurements (e.g., Figs. 25, 36 and 42) and hydrogen bubble visualization (Fig. 78 and recorded movies[62]). As would be expected, the straws are particularly effective in quenching the incoming turbulence. Figure 25 shows the axial profiles of u'/U_∞ for different straw lengths and provides approximate information on the level of the turbulence emerging from the straws. The flow exiting from the longest straws at $x = 0^+$ (which are closest to fully developed laminar flow: $Re_M = 1290$, $\ell/d = 61$), exhibits the largest reduction of the turbulence.

The hydrogen bubbles photographs of Fig. 78 illustrate the corresponding damping of incoming turbulence by the parallel plate manipulator. The suppression of the transverse fluctuating velocity component normal to the plates, u_2', by the constraining action of the parallel plates side walls and the consequent rapid decay of the fluctuating velocity component in the axial direction, u_1', are demonstrated in these photographs. Despite the small upstream influence of the parallel plate manipulator (discussed in part 8 of this chapter) it appears that the major contribution to the suppression mechanism, in the case of the honeycomb, is due to the thwarting of the transverse velocity components, u_2' and u_3', by the honeycomb side walls. This mechanism will, therefore, be particularly effective if the Reynolds number of the honeycomb cell is below the transition Reynolds number.

The short distance from the parallel plate leading edge in which the major portion of this suppression is achieved (see Fig. 78) suggests that much shorter honeycombs than the ones required to reach fully developed flow would be adequate. In light of the added benefits of smaller pressure drop and less turbulence generation by the shear layer instability, downstream of the manipulator (see part 2 of this chapter), the shorter honeycombs appear to be more attractive.

The drainage of energy from the low frequency, large scale eddies is best demonstrated by comparing the spectrum of the incoming flow, for condition "A" in Fig. 10, with the spectra for P.P. #3 in Fig. 39. Note that for condition "A" and P.P. #3, the locations x and $\zeta+6$ are equivalent so that spectrum b in Fig. 10A corresponds to spectrum e in Fig. 39. Spectrum a in Fig. 10A leads most directly to spectrum a in Fig. 39 but because the flow through the plate perforations is accelerated to 32 fps, the frequency scale is stretched and shifted toward higher frequencies. The concentration of energy near 1000 Hz is undoubtedly ascribable to instabilities of the shear layers and jets formed by the perforated plate. It is conjectured that its energy comes not only from the steady flow but also from the low-frequency motions which act in a quasi-steady manner with respect to the high frequency instabilities. At least spectrum e in Fig. 39 appears to have less low frequency content than spectrum b in Fig. 10A. However, direct proof is made difficult by the fact that the spectra are only one-dimensional. Convected skew waves of high frequency register as waves parallel to the hot-wire of much lower frequency (see the graphical construction of Corrsin[63]). Thus, much of the rise in the low frequency content of spectra b and c of Fig. 39 may be fictitious in the sense that it may correspond to skewing of the finer scale motion with respect to the x direction. This view is supported by the rapid drop in low frequencies of spectra d and e of the same figure. The drop exceeds any viscous decay rates for such frequencies, even when the deceleration of $\bar{U}$ is taken into account. Thus, the main message in the developments from spectrum a in Fig. 10A to spectra a through e of Fig. 39, rather than to the spectrum b of Fig. 10A, consists of the selective high-frequency upwelling (which spreads to the rest of the one-dimensional spectrum as it did for Roshko[64]) and the final spectrum with a decreased low frequency content.

2) Turbulence Generation by the Shear Layer Instability. The instability process which leads to the generation of this new turbulence is even more evident downstream of the straws. In fact, in the case of the long straws it may account for virtually all of the turbulence found far downstream. The rapid growth of u'/U_∞ in Fig. 25 is replotted in Fig. 80 using a logarithmic ordinate and an expanded abscissa. The exponential growth,

which is initially masked by the unsuppressed residuals of the incoming turbulence, suggests a linear instability mechanism, which persists to surprisingly large amplitudes. This extremely rapid amplification of the perturbations, present in the flow immediately downstream of the device, is finally controlled by nonlinear effects and the energy level of the fluctuating velocity components reaches saturation at the u' peak. This local instability will probably derive its energy through the Reynolds stress action on the mean flow as well as the large scale turbulent eddies; i.e., through the terms $\overline{u_i u_j}\partial U_i/\partial x_j$ of the Reynolds equations.

The measured spectral peaks (Figs. 26 and 27) and the regular scalloped structure that can be observed in the flow downstream of the 10-in. straws (Fig. 72), confirm the existence and growth of the shear layer instability. In the more easily visualized two-dimensional flow downstream of the parallel plate manipulator (Fig. 79), the growth of the instability and the subsequent randomization of the eddies leading to turbulence is classic.

For the screens and perforated plates where the damping of turbulence by the inhibition of the lateral components of the fluctuating velocity is less effective than for the straws, the spectral structure of the downstream flow remains discernible in flows of high incoming turbulence intensity. One has to look for it within the first 10-20 mesh lengths downstream of the manipulator and keep in mind that for fine-mesh screens the wire length averages over several shear layers (see also part 4 of this chapter). In flows with moderate turbulence intensity (test flow condition "B"), the shear layer instability character was clear in all the spectra (e.g., Figs. 20 and 40).

The multiple spectral peaks such as those in Fig. 40, probably indicate differences in shear layers and initial lack of communication between them. Multiple shear layers with multiple inflections are known to be susceptible to multiple instabilities, which may take place concurrently as, for instance, in Sato's jet[65]. Similarly, in the wakes of circular cylinders the single-layer (or Bloor) instabilities and the double-layer von Karman instability commonly occur simultaneously. One would also expect the presence of higher harmonics when the intensity of the organized fluctuations is high. These have indeed been observed repeatedly in the present experiments (e.g., see Fig. 20). It may be conjectured that the introduction of sound tuned to the sensitive frequency of the shear layer may promote a yet more organized instability.

3) Level, Structure and Decay of Generated Turbulence--Dependence on Shear Layers Characteristics. The influence of the shear layer scale is best documented in the series of tests on the different lengths of honeycomb-like matrices composed of straws having the same diameter. For this series of tests the only parameter is the length of the straws. Variation of this parameter leads to different length scales in the emerging mean velocity profiles: the longer the straws, the more developed the emerging flow and the wider the wall wakes. The largest obtainable length scale is associated with fully developed laminar pipe flow. It was almost achieved in the 10-in. straws. Qualitative differences between the velocity profiles 0.10 in. downstream of the 1- and 3-in. straws are evident in Figs. 22 and 23. The imperfections in packing the straws and the relatively small ratio between the hot-wire length and the straw diameter preclude the possibility of more quantitative comparisons.

Figure 25 displays the effect of the variation in straw lengths on the maximum level of u'/U_∞. The shorter straws with the narrowest shear layer reach the u' peak in approximately half the distance of the longest straws. The spectra of u in Figs. 26 and 27 identify the characteristic frequency, f^*_ℓ, of the instability of the shear layers for the straws of lengths ℓ.

The rate of decay of the generated turbulence also depends on the characteristic scales of the shear layers as evident from Fig. 81. Turbulence generated by the short straws decays more rapidly than that generated by the long straws. This behavior is con-

sistent with the spectral information of Figs. 26 and 27 which show the evolution of turbulence from a smaller scale instability in the case of the short straws.

In Fig. 25 the peak longitudinal fluctuations $(u'/U_\infty)_{max}$ differ substantially for the three lengths of straws as must the peaks of fluctuation energies, $\frac{1}{2}(u_1'^2 + u_2'^2 + u_3'^2)$. As Bradshaw[66] notes, the shear stress $\overline{u_1 u_2}$ in such transition regions can rise locally to double the value of that in fully developed turbulent shear layers. This should contribute to effective smoothing of mean velocity profiles and to extraction of energy from the mean flow and from the large quasi-steady eddies. The level of this activity, which exceeds that of the incoming turbulent flow, should make a challenging research target for both theory and experiment. In the case of the cross-sectionally similar straw-banks of Fig. 25, we must seek the explanation for the striking differences in just two features: the differences in the mean velocity profiles emerging from the straws and in their initial disturbances and disorganization. On the basis of Fig. 25 alone, one might be tempted to theorize that higher three-dimensional fluctuations at the exit from the straws tend to break up the correlated phase relationships required for the rapid growth of the instabilities and thereby thwart the "full capabilities of energy extraction." However, downstream of the perforated plate, P.P. #3, at 35 fps the values of $(u'/U_\infty)_{max}$ were 0.12 and 0.22 for incoming disturbances, u', equal to 5% and 0.08% of u_∞, respectively (see Chapter IV, part D-1). The dimensionless peaks of the fluctuations evidently depend on Reynolds number (primarily below 15 fps, the speed of most tests herein) but the u' peak of P.P. #3 in the high incoming turbulence exceeds that of the low incoming turbulence down to U_∞ of 5 fps. The contrast with trends of Fig. 25 only underscores our ignorance with respect to the role of the instabilities in the shaping of the turbulent structure downstream of the manipulators. We could speculate about competing trends with the aid of the differential equations for the Reynolds stresses but the central fact is our lack of knowledge about the genesis and early energetic stages of any turbulent field.

For grid-generated turbulence the rate of decay some distance downstream of the u' peak is

$$\left[\frac{U_\infty}{u'}\right]^2 = \frac{b}{C_D}\left[\frac{x-x_o}{M}\right] \qquad \text{(VI-1)}$$

where b is approximately 100, e.g., see Batchelor[41], p. 135, or Hinze[43], p. 214.

Lumley and McMahon[51] argue that this relation should also apply to the turbulence generated by honeycombs when C_D is interpreted as a measure of the energy in the exiting mean velocity profile. They show that for fully-developed laminar flow leaving a honeycomb matrix (neglecting blockage by the wall) the appropriate equivalent drag coefficient leads to a value of $C_D = 1$. However, the decay rate shown in Fig. 81 for the nearly fully developed 10-in. straws is considerably smaller than that predicted by the above equation with $b = 100$ and $C_D = 1$ (dotted line). It would appear that the mechanisms associated with the honeycombs and the grids are sufficiently distinct to differentiate between them. According to Batchelor[41], p. 135, there is a factor of nearly two difference in the value of b used in equation (VI-1) between a biplane grid and a simple row of rods. There seems to be no doubt that the grid geometry, or rather the topology of the downstream flow field, plays an important part in the subsequent generation and decay of turbulence.

While the emphasis in this section has been on the fields downstream of straw banks the relationship between the scales of the generated shear layers and the decay of the turbulence seems to be quite general. (See footnote on next page.) The concept of implanting finer shear layers to accelerate the decay when using two manipulators in tandem will be discussed in the next section.

4) Modification of Generated Turbulence by Passive Devices. The addition of a single fine-mesh screen at the exit plane of the straw matrix changes the decay rate of the generated turbulence dramatically. The cross-hatched band in Fig. 81 bounds the data for all three straw lengths followed by a single fine-mesh screen (same type screen listed in

Fig. 6). This band was obtained from the detailed data in Fig. 82, which are less regular than single manipulator data.*

The mechanism leading to the collapse of the strongly different decay curves of Fig. 81 into a single band with a higher decay rate must be associated with the replacement of the larger scales by more dissipative smaller scales generated by the screen shear layers and jets (compare Figs. 23 and 51). Figure 56 displays the axial decay of u'/U_∞ as the chopper screen is placed at different distances downstream from the 10-in. straws. Significantly, the screen is effective as long as it is located upstream of the point where appreciable growth of the large-scale instabilities had taken place (in the case of Fig. 56 this point is approximately at x = 1 in., i.e., 5.6 straw diameters).

The longer the straws, the more developed the exiting profiles (i.e., the smaller the mean velocity gradient, $\partial U_1/\partial r$), and the lower the initial input disturbance to the instability. Consequently, longer downstream distances are required for the growth of the instability for the longer straws (Fig. 80). Therefore, larger separation distance, Δx, can be used between the screen and the longer straws while still maintaining the improved performance of the combined manipulator.

It appears from Fig. 50 that when the finer screen is placed at the exit of the straws the substitution of the smaller dissipative scales for the larger scales of the original manipulator is almost complete. Some differences undoubtedly remain, but the striking common feature is the decoupling from much of the past history, achieved by the chopper screen. Apparently, the energies actually dissipated by the turbulent motions differ little while the drag coefficients, C_D, of the different ℓ's of straws with or without screen are vastly different. The measured values of the pressure drop coefficient, K, for the different manipulators are listed in Fig. 6. It is noteworthy that C_D or K of the screen alone is 0.86 so that the drag coefficients of straws and screen are nearly additive.

An important, but not yet well understood, relation must exist between the scales of the interacting shear layers of manipulators in series. As the shear layers produced by the upstream manipulator become sharper (shorter straws or presumably honeycombs) the effect of the downstream screen on the rate of decay of turbulence became smaller in our experiments. Compare Figs. 20 and 26 to Fig. 53, while paying special attention to the location of the spectral peaks.

When the same fine-mesh screen was affixed to the perforated plate, P.P. #3, (Figs. 57 and 58) essentially the same mean velocity profiles emerged as for P.P. #3 alone (compare to Figs. 32, 33, 37, 57 and 58). This lack of effect, in contrast to the near obliteration of the profiles by the screen in the case of the straws, led us to believe that a manipulator-matching disparity between P.P. #3 and the screen may exist for $\Delta x = 0$. Additional evidence to this matching disparity is found in Figs. 36, 41, 60 and 61. It is clear that the shear layer instability associated with the perforated plate, which is characterized by the peak in u'/U_∞ near $x \simeq 0.8$ in. in Fig. 36, remains, though modified, when the screen is placed at $\Delta x = 0$ (Fig. 60). Although the screen instability is also present (peak at $x \simeq 0.15$ in. in Fig. 60), the plate instability, which leads to the larger scale of turbulence, persists. It was conjectured that the screen operated only on the high velocity jets emerging from the holes of the plate and not on the stagnant velocity pockets between the holes (see Fig. 74). These momentum-deficient pockets should indeed foster the reformation of the mean velocity waviness on the same scale as for the plate without the screen.

A series of experiments with increasing Δx between P.P. #3 and the screen, reported

*In comparing decay rates in the form of Eq.(VI-1) as in Figs. 81, 82, 83 and 85 the reader should keep in mind that when the level of turbulence in the denominator gets low errors due to "noise" lead to large irregularities. The bands into which the resulting graphs fall are indicated by cross-hatching in Figs. 81, 83 and 85.

in Chapter IV, section B-3, demonstrated that the screen can be made as effective as in the case of the straws if distance is allowed for the stagnant pockets to close upstream of the finer screen. The back pressure of the screen is believed to aid the homogenization process. On the other hand, if Δx is large enough so that the plate instability occurs upstream of the screen, the screen ceases to be effective as in the case of the 10-in. straws in Fig. 56. As indicated in part B-3 of Chapter IV, the optimum Δx is 0.125 in. This Δx corresponds to the upstream foot of the instability rise in absence of the screen, where most regular fluctuations are generally observed. Examination of the axial profiles of u'/U_∞ for P.P. #3 with screen at Δx of 0.125 to 0.15 in. disclosed no evidence of the plate instability downstream of the screen. The decay rates demonstrated the effectiveness of perforated plates with screen in tandem as a compact turbulence suppressor. To what extent the addition of the screen may degrade the effectiveness of P.P. #3 in decreasing mean flow nonuniformities has not been tested.

These results support the concept of modifying the turbulence generated by a manipulator through the use of follow-up passive devices which modulate the mean velocity profiles immediately downstream of the manipulator and generate smaller scales of turbulence. The proper selection of the combined manipulators, their solidities and length scales is undoubtedly complicated, as the two preceding examples illustrate. However, the concept shows promise of yielding very compact turbulence suppressors at minimum expense and acceptable pressure drops.

An additional example which deals with a different type of "instability" occurring farther downstream in the case of high-solidity manipulators is discussed in the following paragraphs. It was conjectured that this so-called anomalous behavior develops rather slowly and that the application of the above smoother-chopper concept might prevent it from occurring. Later it was realized that Corrsin[11] arrived at essentially the same stabilization technique for his 83% solid plate with two-dimensional jet slots by different reasoning.

5) Anomalous Performance of P.P. #1 (A Manipulator of High Solidity). As noted in Chapter IV, the flow downstream from P.P. #1 exhibited some characteristics which were not common to the other two plates. In particular, certain irregularities in the mean velocity profile (Fig. 30) developed and persisted far downstream. Also, the decay of u'/U_∞ downstream from P.P. #1 was much slower than that downstream from the other two plates. This behavior is emphasized in Fig. 35 where the turbulence decay, plotted as $(U_\infty/u')^2$ vs. x/M, for P.P. #2 and P.P. #3 for two flow conditions, fall within a relatively narrow band while that for P.P. #1 is grossly lower. One possible explanation for this disparity lies in the coalescing of the jets issuing from high-solidity grids and multiple jets noted by Corrsin[11], Bradshaw[32], Schubauer, et al.[2] and others (see section A-6 of Corrsin's[1] article). This explanation is supported by the hydrogen-bubble visualization of the flow immediately downstream from P.P. #1 shown in Fig. 75a.

A series of experiments (not reported here in detail) were performed to investigate the effect of a passive device, namely the same 30-mesh Dacron screen, on this anomalous behavior. The screen was placed downstream of P.P. #1 at separation distances, Δx, equal to 0, 0.125, 0.25, 0.375 and 1.375 in., and the axial profiles of u'/U_∞ downstream of the combined manipulators were recorded. All these profiles yield a much higher rate of decay than that due to P.P. #1 alone (recorded in Figs. 34 and 85). While different turbulence reduction factors, F_1, were obtained for the different off-sets, Δx, the screen reduced the anomalous level of turbulence by a factor of approximately four at $x = 8.0$ in. Curiously, for $x = 8.0$ in., the screen placed directly against the plate appeared to be as effective as the other Δx positions, although the early decay was slower. The large reduction achieved by tandem screen opens up the prospect of curing the anomaly of wind tunnels in which higher solidity devices have been inadvertently installed.

6) Influence of Structure of Upstream Flow on the Performance of the Manipulator. An important point to keep in mind in selecting a system for turbulence reduction is the

fact that the performance of the manipulator should not be expected to be identical for all incoming flow field structures. The structure of the incoming flow field may be characterized by the level of turbulence, its macroscale, the spatial distribution of the mean and fluctuating velocity components, and the spectral distribution of the energy of the fluctuating velocity components (e.g., Tsuji[13,14]).

The rate of decay of turbulence downstream of a single screen when placed in three different test flow conditions is compared directly in Fig. 18 and in the Batchelor coordinates in Fig. 83. It is clear that the screen is rather ineffective for condition "A". In fact, the corresponding axial profile in Fig. 18 indicates anomalous growth and a plateau after an initial decay of screen-generated turbulence (subsidence of high frequencies above 600 Hz between curves a and b in Fig. 19A). Apparently the intense large-scale structure of turbulent condition "A" (including a possible swirl component and slowly varying secondary flows) barely responds to the fine 30-mesh screen with the low pressure drop K of 0.86. The spectra of Figs. 19A and 19B suggest that the anomalous growth is related to the low-frequency, large-scale structure. It is conjectured that "A"-like flows need to be tackled first with honeycomb-like flow straighteners and perhaps with larger-mesh grids (perforated plates) with larger pressure drops to remove the turbulence regenerative conditions which led to response "A" in Fig. 18. (Straw-banks with a juxtaposed screen did tame the anomalous tendencies of condition "A" when conditions "B" and "C" were engineered.)

The validity and limitations of the linear law of Batchelor and Townsend, Eq.(VI-1), embodied in straight line plots in Figs. 81 and 83, has been discussed from different points of view by Tsuji[67], Uberoi and Wallis[23], and Comte-Bellot and Corrsin[25], even for pure turbulence generated by a single "grid." Although Batchelor and Townsend[20] labeled it as the law for the initial period of decay, they excluded the first 20 to 30 mesh lengths (usually transversely inhomogeneous) from the region of its applicability. Since in the manipulator applications the turbulence stems from multiple sources, the departure from linearity of given decay data or a lower coefficient b in Eq.(VI-1) do not necessarily reflect negatively on the particular manipulator. The reader will find Tsuji's two studies of decay[13,14] of turbulence behind two grids with variable separation most helpful for appreciating the effects of the double, but still rather pure, turbulent structure. In Fig. 83, the relatively rapid decay of the purer turbulence downstream of the screen in condition "B" and the slower decay in the disturbed condition "C" appear consistent with the trends observed by Tsuji.

The turbulence reduction factor, F_{1n}, for n screens placed in series, which was measured in condition "A", proved to be consistently different from the results of the controlled experiments of Dryden and Schubauer[3]. The present data, shown in Fig. 84, correlate well according to $F_{1n} = 1/(1+K)^{n/2.7}$. Comparison with the correlation $F_{1n} = 1/(1+K)^{n/2}$ of Dryden and Schubauer [3] again hints at the lessened effectiveness of the screens in the adverse condition "A".

Another observed dependence of the screen performance on the incoming turbulence is related to operations near "critical shedding" condition. Detailed measurements downstream of above-critical and below-critical screens can be found in the classical work of Schubauer, Spangenberg and Klebanoff[2] (e.g., see their Figs. 5 and 6). In Fig. 13 of their report, the empirical critical Reynolds number of the screen (based on wire diameter and free-stream velocity) is plotted as a function of the screen solidity.

A series of tests (to be reported later) was performed on seven different screens for both conditions "A" and "B": three of the screens are below critical, three are above critical and one is just subcritical, according to Fig. 13 of Schubauer, et al.[2], for a free-stream velocity, U_∞, of 15 fps. Moderate instability peaks were observed in the axial development of u' downstream of the subcritical screens when the incoming flow was in the highly disturbed condition "A". Even the milder disturbances of condition "B" generally exhibited peaks and the tell-tale spectral growth in discrete high frequencies. For

example, in Fig. 20 the screen (mesh 0.033 in., thread diameter 0.005 in., pressure coefficient 0.86) operated in the subcritical regime according to Fig. 13 of Schubauer, et al.[2] (Re = 40, σ = 0.28). However, discrete spectral growth, near 1800 Hz, is observed at 0.25 in. or 7.5 mesh lengths downstream of the screen, i.e., near the instability peak (Fig. 17). This spectral excitation appears consistent with subcritical instabilities in presence of finite disturbances downstream of Taneda's cylinder as discussed by Morkovin[68]. These observations should be compared with the remarks on p. 15 of Schubauer, et al.[2]: "...critical Reynolds numbers were unchanged when the incident turbulence was raised..." It was suspected that the difference between the turbulence of Schubauer, et al.[2], u'/U_∞ of 0.7% for the precritical cases, and 1.5% and 8% for conditions "B" and "A", respectively, could account for the difference in observations. Special conditions were engineered with u'/U_∞ of 0.7% and 0.2%. The corresponding sudden onset of regular fluctuations, immediately downstream of the screen, occurred at 16 and 20 fps. Thus, subcritical instabilities indeed appear to depend on the level of the finite disturbances.

An apparently different sensitivity to the incoming turbulence was observed by Kellogg[47] and Kellogg and Corrsin[48] for their very subcritical "zither" (0.003 in. dia. parallel wires, 0.064 in. apart, i.e., solidity of 0.05, examined at Reynolds number of 25 and incident u'/U_∞ of 2.1%). Kellogg's[47] Figures 10 and 11 indicate that a transversely inhomogeneous peak of u'/U_∞ far in excess of the incoming level must exist within the first 100 wire diameters (4.7 mesh lengths) downstream of the zither. The authors conjecture on two not necessarily independent mechanisms of general interest. The incident large-scale turbulence makes the sharp new wakes "flop" and wrinkle. A fixed hot-wire senses even a purely kinematic (frozen) unsteady transverse translation of the wake profile as u' (roughly proportional to the displacement and to $\partial U_1/\partial x_2$). The trarsverse component of this motion is likely to induce a dynamic effect as well, leading to generation of $\overline{u_1 u_2}$ in the nominally isotropic field and to new turbulence through the production $\overline{u_1 u_2}\ \partial \bar{U}_1/\partial x_2$. Order of magnitude arguments bear out the feasibility of the mechanisms.

These mechanisms are undoubtedly present for supercritical grids and screens in addition to the instability mechanism. It is not clear how rapidly these mechanisms operate and to what extent they help to generate the observed early shifts to higher frequencies. The instability mechanism (defined by the inoperativeness of the term $\omega_j \partial \bar{U}_i/\partial x_j$ in the equation for the growth of vorticity ω_i) is known to evolve exponentially until inhibited by nonlinearities. Spectra of postcritical u' peaks, even though distorted by their one-dimensional nature, suggest that a substantial portion of the energy increase is due to the narrow-band process, which is subsequently randomized. For example, in the post-peak spectra of Fig. 20 (for $x \geq 0.25$ in.) the high frequency upwelling is significant. It is unfortunate that Kellogg and Corrsin[47,48] did not report any spectra in the growth region of u' which might help to assess the tell-tale rate of growth and the relative importance of the different mechanisms. The basic equations (but not the approximations) which they used in their analyses are equally valid for the instability mechanisms.

7) Structure of Generated Turbulence and Uniformization of Mean Velocity Profiles. One general subjective observation gained from the present experiments is: the larger the scale of turbulence downstream from a manipulator, the more rapid the demise of mean velocity nonuniformities. This effect can be discerned from the evolution of the radial profiles of mean velocity downstream from all manipulators. The reader should appreciate, however, that the scale of the nonuniformities of U(r) and the scale of the generated turbulence are related for all cases except those in flow condition "D". Thus, it is more revealing to compare mean velocity development downstream from the same primary manipulator but with altered downstream turbulence. In particular, compare mean velocity defects downstream from P.P. #3, Fig. 37, with those downstream from P.P. #3 plus a single screen, Fig. 58. In spite of the presence of a screen, which increases the pressure drop across the combined manipulator, the basic defect pattern in the plate re-emerges after about 0.5 in. and then decays slower than in the case of P.P. #3 without the screen. In our inter-

pretation the screen has generated smaller scale turbulence at the expense of energy from the mean flow and the "quasi-steady" large scale eddies. Directly or indirectly the larger-scale content is relatively more depleted or starved and the remaining turbulence is less effective in homogenizing the mean velocity profile. In principle, the same argument could be applied to the flow downstream from the straws plus screen (Fig. 51 compared to Fig.23). In that case, however, the larger-scale and the finer-scale velocity defects decay hand-in-hand in a nearly balanced manner so that the basic mean periodicity does not re-emerge (except perhaps when the flow is almost uniform, Fig. 51).

The turbulence downstream from the tested samples of the porous foam material also appeared to suffer from an unbalance of energy among the scales, e.g., Figs. 43-45. It is conjectured that the high pressure drop, K = 6.6, erases most of the dependence on the incoming turbulence and that as in the case of the long straws, the downstream turbulence is set primarily by the emerging velocity profiles. These, in turn, are conditioned by the fine-scale pores, from which irregular streams jet out, and by the apparently unavoidable random larger-scale nonuniformities of the material. The irregular fine jets apparently set up intense small-scale turbulence which decays very rapidly (Figs. 44 and 45, $x < 1$). An anomalous regeneration is often indicated (see discussion of Fig. 45 in Chapter IV, section A-4) followed by a very slow decay of both the mean velocity defects and the remaining medium- and large-scale turbulence (Figs. 43-45).

It is believed that without the larger-scale nonuniformities (incurred in manufacturing, handling and installing), porous materials would exhibit only the first phase without the undesirable persistence of velocity nonuniformities. A spectacular display of the nonuniformities was presented in the runs with P.P. #1 plus foam. The high-solidity perforated plate alone behaved in an "abnormal" manner (see section 5 of this chapter) leading to highly irregular radial distributions of $\overline{U}$ and u'/U_∞. When foam was affixed to the downstream side of this plate, these irregularities became much more persistent. The two axial profiles in Fig. 67 illustrate the remarkable persistence of mean and fluctuating velocity differences at two radial locations as well as the lack of decay past $x = 4.0$ in.

Some feeling for the scale of turbulence downstream from the foam can be obtained from the hydrogen bubble picture at a lower Reynolds number, Fig. 76. Nonuniformities in $\overline{U}$ appear frozen in the flow field. (Care must be taken in interpreting the integrating effect of the visualization technique. A persistent nonuniformity in $\overline{U}$ results in a growing distortion of the black time-lines while a pattern of frozen time-lines indicates a uniform velocity field.)

Thus far in this section we have outlined our current but incomplete perception of self-uniformizing wakes, i.e., of decay of mean-flow inhomogeneities which were introduced by the manipulators themselves. Several histories of progressive uniformization of pre-existent inhomogeneities in test condition "D" are presented in Chapter IV-C and are incorporated in Figs. 68-71. The dimensionless pressure drop across P.P. #3 and across the 3-in. straws plus screen are 1.5 and 2.9, respectively.

Unfortunately, the last measured profiles for P.P. #3 at $x = 2.5$ in., Fig. 68 ($\zeta = 4.0$ of Fig. 14) are located 8 in. upstream of the last data for 3-in. straws plus screen at $x = 6.5$ in., Fig. 71 ($\zeta = 12$ of Fig. 14). Our impression is that P.P. #3 is definitely more effective than the 3-in. straws plus screen in removing the mean flow nonuniformity at a cost of originally higher turbulence level, but at a lesser pressure loss.

Another comparable test consisted of three basic Dacron screens (same type described in Fig. 6) 0.5 in. apart, with net pressure coefficient K of 2.58. Referring to the conditions at $x = 2.5$ in. ($\zeta = 4.0$ in.) for P.P. #3 alone, Fig. 68, we found the percent nonuniformity in both $\overline{U}(r)$ and $u'(r)/U_\infty$ one inch farther downstream, at $\zeta = 5.0$ in., to be inferior for the three screens, but at roughly half the turbulence level. However, this turbulence gave indication of an unbalance between the larger and finer scales in the sense used in connection with Fig. 58 in this section. The considerable transverse inhomogenei-

ties behind the three screens (comparable in character to those in Fig. 71) may have been continuously generating new turbulence where $\partial\overline{U}_1/\partial x_2$ was high, feeding the peaks in u'/U_∞ (as in Fig. 71). In the meantime, the less intense smaller-scale activity at the maxima and minima of $\overline{U}$ apparently contributed only mildly to their eradication.

If these subjective observations are correct, the mesh size of the manipulator should not be grossly mismatched with the transverse scale of the pre-existent inhomogeneities. The Taylor-Batchelor theory[7] indicates that the downstream decay does scale with this transverse characteristic length. Experiments[1,12,41] suggest that the decay of turbulence generated by grids scales with the mesh length (except in the immediate vicinity of the grid). Obviously, if we made the mesh equal to the transverse scale of inhomogeneities, we would make little progress. Experiments with foam (very fine mesh) in test condition "D" once again underscored the undesirability of its very rapid decay of turbulence coupled with the persistence of large-scale nonuniformities for the longest distances. Between these extremes it should be possible to achieve a "balance between the decay rate of the largest mean inhomogeneity and the decay rate of the grid-generated turbulence." Clearly much remains to be done before this concept can be considered truly substantiated. Lest the reader be over-influenced by these ideas, he should study Figs. 14 and 15 of Schubauer, Spangenberg and Klebanoff[2], who tested systematically a number of single screens in four conditions of mean-flow inhomogeneities (but unfortunately do not cite the corresponding turbulence levels). They report no adverse evidence on the performance of fine-mesh screens of solidity below 0.45 and recommend the usage of several low-K screens in series (see also section 11 of this chapter).

8) Extent of Upstream Influence of the Turbulence Manipulators. The manipulators can exert upstream influence through pressure fields associated with irrotational velocity fields which are anchored to singularities within the physical boundaries of the "obstruction." The Taylor-Batchelor mechanism[7], investigated experimentally by Townsend[10], and the mechanisms discussed by Hunt[37,38] are of this character. During the present measurements occasional glimpses of the nature of this effect for different manipulators were obtained.

As described in section A-3 of Chapter IV, it was possible to penetrate upstream of perforated plate #3 through its 0.25 in. openings. The necessary corrections for the interpretation of such traverses as in Figs. 36, 41 and 42 were discussed in Chapters II and IV. With these in mind we can trace the upstream influence on u' and $\overline{U}$ along the centerline to a distance equal to two hole diameters or less. This is in accordance with the aforementioned theories and with the measurements of Uberoi[69] on effects of wind-tunnel contractions. Along the streamline passing through the hole center the effect is primarily one of stretching, with a consequent drop in u', which seems surprisingly large for the nonlinearly disturbed condition "A" in Fig. 36, even when we allow for corrections on the order of +0.1 for the minimum of u'/U_∞. The slight drop of $\overline{U}$ in Fig. 42 was identified as fictitious in section A-3 of Chapter IV. It is likely then that the influence on $\overline{U}$ upstream of the blocked stagnation lines also extends roughly over 0.4-0.5 inches. This would agree with the measurements of Bearman[40] upstream of a two-dimensional obstruction if we allow for the decreased reach in our quasi-axisymmetric configuration.

Bearman's[40] turbulence measurements and Hunt's theory[37,38] make it clear that the response of the oncoming turbulence to the potential strain fields along the above-mentioned two lines and in between them will be a function of the scale distribution of the turbulence. Thus, even the upstream effects of the manipulators should depend on the turbulence structure as contended in section 6 of this chapter.

The net effect, averaged over the area of the opening of the manipulator, is unlikely to exceed the 10-40% changes in u' indicated by Figs. 42 and 36. The changes due to these various mechanisms would then appear rather small in comparison to the downstream changes leading to the instability peaks in Figs. 36, 41 and 42. It is difficult to see how this large increase in u' can be ignored. It is also difficult to see where it is

taken into account in the existing theories for passage of turbulence through screens and grids (except perhaps in the Kellogg-Corrsin approach[47,48] or most indirectly through the linearized pressure drop and its floating parameter K).

The other glimpse of upstream influence is provided by hydrogen bubble visualization of the parallel-plate simulation of honeycombs in Fig. 78. The reader is urged to refer to the discussion of the geometry and the location of the bubble-generating wires in Chapter V-B before attempting to interpret the photographs. Generalizing from the preceding discussion we could expect upstream influence for a distance of approximately three slot openings for this two-dimensional configuration. Comparison between the formations downstream of the first wire on the right-hand side of the lower photograph in Fig. 78 and those downstream of the second wire indicates that the latter have indeed adjusted substantially to the proximity of the nearby plates. Unfortunately, since the emphasis was on the accommodation to the constraint on transverse velocities through the parallel plates, no additional wires somewhat farther upstream were utilized.

9) The Characteristics of Passive Devices as a Function of Speed. The weak dependence of the turbulence reduction factor, F_1, and the decay rates, $(U_\infty/u')^2$, for the velocity range from 5 fps to 40 fps (described in part D of Chapter IV) is in agreement with the earlier understanding (see Corrsin[1,70]). The experiments were limited to P.P. #1, P.P. #3, and the 10-in. straws and their main purpose was to verify that no surprises lurked in this speed range (commonly used in settling chambers) for these less often investigated devices. The appearance of different regular instabilities including those associated with sound fields deserves some attention.

The narrow band instabilities of the shear layers do not seem to diminish with the increase in Reynolds number--they merely shift to higher frequencies. They also lead to aerodynamic sound which probably contains dipole components and intensifies rapidly with increasing speed (dynamic pressure). The "singing" of the perforated plate above 35 fps was intense indeed.

Discrete frequency sound waves time and again regularize and coordinate instability phenomena through upstream and cross-stream feedback (edge-tones, Parker modes[71], etc.) and at higher frequencies can couple with velocity-independent resonant modes of the duct or tunnel. (Even the straw-banks exhibit such resonance--650 Hz for the 10-in. straws and 1270 Hz for the 5-in. straws in the test duct.) As Morkovin, et al.[72] commented, the acoustic modes in wind tunnels are easier to observe than to predict or analyze (see also Batchelor[73]). And, as remarked earlier, in part 2 of this chapter, multiple shear layers often possess multiple instabilities. It would be of little use, therefore, to speculate on which instabilities and which acoustic feedbacks and resonances are likely to occur in general. Rather, we should be aware of the possibility if not probability of encountering instability-acoustic coupling as speed is increased. This may have a bearing even on the design of turbulence management devices for transonic and supersonic wind tunnels, where sound fields from the settling chambers may be influencing the transition of boundary layers (according to experiments of Beckwith and Stainback[74]).

In flows of water the relatively high density of the fluid often leads to coupling of shear instabilities with elastic resonant modes of the immersed structures. One could conjecture that the "singing screens" of Lumley and McMahon[51] manifested hydroelastic coupling. This tendency of screens to sing restricted if not eliminated their use in water tunnels. Recently Klebanoff and Spangenberg pointed out that our experiences with fine-mesh screens at the exit of the straw-banks may allow for the effective usage of chopper screens (see section 4 of this chapter) attached to the downstream end of honeycombs (the present favorite suppressor of turbulence in water tunnels).

10) Present Findings and the Classical Theories and Experiments. The spectral information and the flow visualization records presented in this report tend to focus the attention on the region immediately downstream of the devices, which had remained unexplored.

In the language of Morkovin[75]: "We were able to enlarge somewhat upon the state of knowledge previously described by Corrsin[1], Schubauer, et al.[2], Lumley and McMahon[51] and others, primarily through the identification of...(an) 'instability flow module'" in all manipulators and a "...suppression flow module..." in the straw-banks (honeycombs). Based on the presented evidence there seems to be little question that there is an instability mechanism or module besides the older, well-established mechanisms. Since a fair amount of knowledge was available on the properties of unstable free shear layers, an attempt was made to "manipulate" these properties by combining the passive devices. The reader can assess for himself the degree of success of these attempts which are discussed in parts 4 and 5 of this chapter.

In the presence of this documented instability and the associated generation of new finer-grain turbulence, the mechanisms which form the basis of the available theories do not model the downstream mean or fluctuating flows completely. For instance, in the Taylor-Batchelor theory for nonuniformity of mean flow[7], the stream function for the downstream region, Eq.(2.9) will need correction. Some of the instability effects will be reflected in the pressure drop parameter K which remains undetermined in the theory. To the extent that the theory uses the K obtained experimentally in presence of the instability, the mechanism associated with the action of the turbulence generated by the device would be automatically included in the theory. With empirically determined K one could expect satisfactory agreement between the Taylor-Batchelor theory[7] and the experiment as documented in Fig. 16 of Schubauer, Spangenberg and Klebanoff[2] for the changes of the mean velocity nonuniformities across a single screen with corrections for decay. The presence of instability is in no way inconsistent with the invoked basic principle[7] "that the local pressure drop across the gauze is determined by the local (mean) longitudinal velocity and by the resistance coefficient." The theoretical streamwise decay of the mean inhomogeneities, however, is purely inviscid so that it could not account for the difference in the performances of P.P. #3 and P.P. #3 plus screen, described in section 7 of this chapter and portrayed in Figs. 37 and 58. Those differences unquestionably stem from the turbulence structure conditioned by different instabilities.

As to turbulence itself, the check between experiment and theory for the turbulence reduction factor, F_1, in Fig. 9 of Schubauer, et al.[2], can hardly be considered satisfactory. One suspects that here the floating parameter K (linearized) applied to each Fourier component does not characterize the largest effects present: the narrow-band instability and the subsequent strong nonlinear interaction. A linear theory is the logical first step in modeling a complex phenomenon. Our results suggest where any linear theory had to fall short in this case.

The findings of the present work should not be surprising in view of the recently increased evidence that some turbulence is generated by eigen-type processes. This evidence, which can be found in the works of Brown and Roshko[77], Crow and Champagne[78], Lumley[79], Corino and Brodkey[80], Gupta, Laufer and Kaplan[81], and Kline, et al.[82] confirms the possible growth of these processes even in the presence of other turbulence. The above-mentioned examples cover a wide variety of flows ranging from turbulent boundary layers, to free shear flows, to clear air turbulence.

Our quest has been for qualitative understanding of trends for practical applications. The behavior of the flow and its modification in the region immediately downstream of passive devices appeared as one key to the control of downstream nonuniformities and turbulence levels. Our early results, together with the understanding of the mechanisms in the theories, became the intuitive engineering basis for conjectures concerning combinations of manipulators in tandem. With almost no exceptions, the conjectured trends were borne out by subsequent testing. Our qualitative and incomplete appreciation of the ingredients of the mechanisms may be subjective and nonrigorous, but it has been useful.

11) Toward a Uniform Stream With Low Turbulence. In this section we summarize the concepts we found useful, in the design of low turbulence wind tunnels and water channels in the form of a "subjective recipe":

a) Minimize non-axial components of the mean velocity associated with swirls and secondary flows through the use of honeycomb-like flow straighteners.

b) Operate on the remaining inhomogeneities in the mean velocity with larger-mesh devices and adequate pressure drop. The choice of the mesh size and the solidity of the device(s) depends on the magnitude and scale of the nonuniformity and remains a somewhat controversial art (section 7 of this chapter).

c) Operate on the remaining turbulence with manipulator(s) possessing high reduction factors, F_1, per unit pressure drop, with an eye on compactness requirements.

d) When extra low turbulence is desired, allow for ample time for the decay of the U_∞-convected debris within the settling chamber (Townsend[42]) and consider large area reduction upstream of the design flow (e.g., Corrsin[1]; Dryden and Schubauer[3]).

The first and second steps seem often but not always interchangeable. The caution advised classically[1,2] against screens with solidity in excess of 0.5 has been reinforced by Bradshaw's findings[32] on further possible anomalous consequences. We feel that slowly or inadequately suppressed mean-flow inhomogeneities may also lead to a type of anomalous behavior in which new turbulence is persistently generated (section 7 of this chapter).

All four steps (except the contraction section) also constitute the essential procedures for minimizing nonuniformities and fluctuations in scaler fields such as temperature (Townsend[42], pp. 58-62; Morkovin[76]).

To illustrate the selection of manipulators for turbulence reduction, a composite plot of the axial profiles of u'/U_∞ for several manipulators of approximately equal pressure drop is presented in Fig. 86. Of the devices tested, the most effective in this case of the highly disturbed condition "A" (suspected of harboring traces of swirl and unsteady secondary flows) was a combination of straws and a screen. Recalling that the performance of these devices depends on the incoming disturbed field (section 6 of this chapter), we feel that it is quite possible for the combination of the three screens or for P.P. #3 plus a screen properly separated (section 4 of this chapter) to turn out preferable in less disturbed flows, especially where compactness becomes a factor. The porous foam, although an effective attenuator of turbulence, if one has the ΔP to spend, was judged generally undesirable because of its tendency to introduce persistent nonuniformities in mean velocity. If the objective were to produce persistent nonuniformity in the mean velocity (e.g., a prescribed shear flow), the foam with a properly tailored thickness distribution might provide a solution.

The reader is again cautioned that the preceding views, though based on a large number of experiments spread over two and a half years, are subjective and not fully concurred with by previous investigators. There is a strong case for using primarily a series of fine-mesh screens with solidity on the order of 0.3. The issue centers on the relative combined effectiveness of steps (b) and (c). It was formulated very clearly in a private communication from G. Schubauer:

"It is important to remove spatial irregularities as completely and effectively as possible, but it seems to me that we need to know what we can remove more effectively with a coarse grid than we can with a fine screen. The reason for some concern is that it is also important to remove as much turbulence as possible, and the question of defeating this end by the introduction of more turbulence by a coarse grid should be considered. The overall pressure drop is also involved, and increasing it has unwanted effects, among which is a contribution toward making the tunnel fan produce more noise for a given flow."

A number of other ingredients for the ultimate trade-off decisions were discussed in section 7 of this chapter, in particular that of the persistent generation of turbulence through the lingering nonuniformities in the mean shear. At present, the evidence for either view remains far from compelling. At least the target for the next generation of research on flow inserts has been clarified.

CHAPTER VII
CONCLUSIONS

A series of experiments were performed to study the effect of several types of passive devices on the level and structure of free-stream turbulence and on the mean velocity distribution in duct flows. These devices, termed turbulence manipulators, included screens, perforated plates, porous foam, honeycomb matrices formed with closely packed plastic drinking straws and combinations of them placed in series. These manipulators are viewed as operators which suppress the level of the incoming turbulence and generate new turbulence. This newborn turbulence is characteristic of the geometry of the device and the Reynolds number through many mechanisms including newly identified narrow-band instability processes. In this sense these manipulators can be utilized to control, manage and/or modify the incoming turbulent flow field to yield the flow appropriate to the application.

The measurements were performed in air using hot-wire anemometry. Flow visualization in water using the hydrogen-bubble technique graphically confirmed the presence of inferred mechanisms associated with the instability of the fine shear layers downstream of the manipulators and with the suppression of incoming turbulence.

The results of the experiments indicate*:

1) The suppression of incoming turbulence in the case of honeycombs is largely due to the passive constraint of lateral components of the fluctuating velocity. For most manipulators it is conjectured that part of the energy contained in the undesirable larger scales of motion is drained away by the Reynolds stresses of the smaller-scale laminar instabilities and the corresponding turbulent motions.

2) The shear layer instabilities and growing turbulent Reynolds stresses generate new, vigorous turbulence. However, these high-frequency fluctuations dissipate rapidly, leading to turbulence reduction factors, F_1, smaller than one. Records of the nearly exponential growth of the longitudinal fluctuations u' and its early narrow-band spectral structure confirm the significance of the role of the instabilities.

3) The character of the fine shear layers emerging from the manipulators has a strong influence on the level, structure and decay of the turbulence farther downstream. Characteristics of honeycombs (straw-banks) of identical mesh size but of different streamwise depths, shown in Fig. 25, illustrate the substantial differences which can occur.

4) The level, structure and decay of the turbulence downstream of a manipulator can be easily modified by placing another device in close proximity of the first and thereby modifying its shear layers and consequently its instabilities. Thus fixing a fine-mesh (chopper) screen to the back of the straw-banks of Fig. 25 leads to the substantially different characteristics of Fig. 50. The resulting turbulence is characteristic neither of the original device nor of the superposition of the separate effects.

5) As noted by other investigators, manipulators of high solidity (larger than approximately 50%) tend to exhibit an "instability" of a different type. Individual jets through the narrow openings apparently coalesce into discrete groups of larger jets downstream of the manipulator, and lead to nonuniform and unsteady flow. This anomalous behavior engenders inflectional turbulence production and slower rates of decay.

6) The upstream flow structure (frequency spectra, level and spatial distribution) can influence the performance of the manipulators. This important effect was documented earlier by Tsuji[13,14] for grids. Consequently the published dependence of the reduction factors F_1 on the pressure coefficient K is not universal and may lead, for example, to unconservative estimates of the number of screens needed for a given design

*For the detailed discussion of each conclusion, see corresponding section number in Chapter VI.

(Fig. 84). In the presence of high upstream disturbances many normally subcritical screens exhibit regular instabilities.

7) Uniformization of mean velocity profiles depends on a balance of scales in the turbulence downstream of the manipulator. The efficacy of devices generating large scale turbulence (perforated plates) in smoothing out gross inhomogeneities in the mean velocity profiles is illustrated. By contrast, in flows with predominantly fine-scale turbulence, such as downstream of porous-foam slabs, mean velocity nonuniformities tend to persist. These effects operate alongside the old smoothing principle[7] which relates the changes in the local streamwise velocity $U(x_2)$ to the local pressure drop across the transversely homogeneous manipulators and to the uniform pressure coefficient K.

8) Turbulence manipulators display short upstream influence. The transversely periodic acceleration and straining of the fluid upstream of the openings in the manipulator is restricted to short distances upstream on the order of two to three mesh lengths.

9) In accord with previous information, only weak dependence on Reynolds number in the characteristics of the passive devices was observed in limited tests not exceeding 40 fps. However, the instabilities often lead to aerodynamic sound which intensifies rapidly with increasing speed (dynamic pressure). The designer should be aware of the likelihood that undesirable resonant coupling may ensue with acoustic modes of his air channel or with elastic modes of the inserts or other structural elements in his water duct.

10) Speculations on the relationship between the theoretical modeling of screen effects and their observed physical characteristics are offered in section 10 of Chapter VI.

11) A "subjective recipe" for improving flow uniformity and turbulence in ducts and tunnels is presented in section 11 of Chapter VI. It is also suggested that close coupling of manipulators in series may be more effective on the basis of equal pressure drop than individual manipulators and offers advantages of compactness.

The present findings enlarge somewhat on the previous state of knowledge, described by Corrsin[1] and Schubauer, et al.[2], primarily by focusing on the region immediately downstream of the manipulators and on the scale distribution of the emerging turbulence as a factor in accelerating homogenization of mean flow nonuniformities and in the ultimate decay of turbulence. For simultaneous homogenization of the mean flow and suppression of turbulence the relative merits of using a sequence of manipulators with decreasing mesh lengths versus a sequence of fine-mesh screens remain to be more conclusively documented by future research.

REFERENCES

1. Corrsin, S. — "Turbulence: Experimental Methods," Handbuch der Physik, 8, 2, 1963, p. 523.

2. Schubauer, G. B. Spangenberg, W. G. Klebanoff, P. S. — "Aerodynamic Characteristics of Damping Screens," NACA Tech. Note No. 2001, 1950.

3. Dryden, H. L. Schubauer, G. B. — "The Use of Damping Screens for the Reduction of Wind-Tunnel Turbulence," J. Aero. Sci., 14, 4, 1947, p. 221.

4. Prandtl, L. — "The Attainment of a Steady Air Stream in Wind Tunnels," translated as NACA Tech. Mem. No. 726, 1933.

5. Collar, A. R. — "The Effect of a Gauze on the Velocity Distribution in a Uniform Duct," Brit. Aero. Res. Coun., Rep. and Mem. 1867, 1939.

6. Batchelor, G. K. — "On the Concept and Properties of the Idealized Hydrodynamic Resistance," Australian Council of Aeronautics, Rep. A.C.A., 13, 1945.

7. Taylor, G. I. Batchelor, G. K. — "The Effect of Wire Gauze on Small Disturbances in a Uniform Stream," Quart. Journ. Mech. and Applied Math., 2, 1, 1949, p. 1.

8. Dryden, H. L. Schubauer, G. B. — Appendix to Reference 7.

9. MacPhail, D. C. — "Experiments on Turning Vanes at an Expansion," Brit. Aero. Res. Coun., Rep. and Memo. 1876, 1939.

10. Townsend, A. A. — "The Passage of Turbulence Through Wire Gauzes," Quart. Journ. Mech. and Applied Math., 4, 3, 1951, p. 308.

11. Corrsin, S. — "Investigation of the Behavior of Parallel Two-Dimensional Air Jets," NACA ACR No. 4H24, 1944.

12. Baines, W. D. Peterson, E. G. — "An Investigation of Flow Through Screens," Trans. ASME, 73, 5, 1951, p. 467.

13. Tsuji, H. — "Experimental Studies on the Characteristics of Isotropic Turbulence Behind Two Grids," J. Phys. Soc. Japan, 10, 7, 1955, p. 578.

14. Tsuji, H. — "Experimental Studies on the Spectrum of Isotropic Turbulence Behind Two Grids," J. Phys. Soc. Japan, 11, 10, 1956, p. 1096.

15. Naudascher, E. Farell, C. — "Unified Analysis of Grid Turbulence," J. Eng. Mech. Div., Proc. Am. Soc. Civ. Eng., 96, EM2, 1970, p. 121.

16. Davis, L. — "Measurements of Turbulence Decay and Turbulent Spectra Behind Grids," Jet Propulsion Laboratory Report No. 3-17, 1952.

17. Castro, I. P. — "Wake Characteristics of Two-Dimensional Perforated Plates Normal to an Air-Stream," J. Fluid Mech., 46, 3, 1971, p. 599.

18. Luxenberg, D. S. Wiskind, H. K. — "Some Effects of Air Injection on the Turbulence Generated by a Bi-Planar Grid," Division of Fluid, Thermal, and Aerospace Sciences, School of Engineering, Case Western Reserve University, Report No. FTAS/TR-69-42, 1969.

19. Liu, J. C. H. Greber, I. Wiskind, H. K. — "Experimental Measurements of Grid-Injection Turbulent Flows," Division of Fluid, Thermal, and Aerospace Sciences, School of Engineering, Case Western Reserve University, Report No. FTAS/TR-70-53, 1971.

20. Batchelor, G. K. Townsend, A. A. — "Decay of Isotropic Turbulence in the Initial Period," Proc. Roy. Soc. Lond. A, 193, 1948, p. 539.

21. Batchelor, G. K. Townsend, A. A. — "Decay of Turbulence in the Final Period," Proc. Roy. Soc. Lond. A, 194, 1948, p. 527.

22. Stewart, R. W. Townsend, A. A. — "Similarity and Self-Preservation in Isotropic Turbulence," Phil. Trans. Roy. Soc. Lond. A, 243, 1951, p. 359.

23. Uberoi, M. S. Wallis, S. — "Effect of Grid Geometry on Turbulence Decay," Phys. Fluids, 10, 6, 1967, p. 1216.

24. Uberoi, M. S. Wallis, S. — "Small Axisymmetric Contraction of Grid Turbulence," J. Fluid Mech., 24, 3, 1966, p. 539.

25. Comte-Bellot, G. Corrsin, S. — "The Use of a Contraction to Improve the Isotropy of Grid-Generated Turbulence," J. Fluid Mech., 25, 4, 1966, p. 657.

26. Batchelor, G. K. Proudman, I. — "The Effect of Rapid Distortion of a Fluid in Turbulent Motion," Quart. Journ. Mech. Applied Math., 7, 1954, p. 83.

27. Ribner, H. S. Tucker, M. — "Spectrum of Turbulence in a Contracting Stream," NACA Report-1113, 1953.

28. Friehe, C. A. Schwarz, W. H. — "Crid-Generated Turbulence in Dilute Polymer Solutions," J. Fluid Mech., 44, 1, 1970, p. 173.

29. Corrsin, S. Karweit, M. — "Fluid Line Growth in Grid-Generated Isotropic Turbulence," J. Fluid Mech., 39, 1, 1969, p. 87.

30. Elder, J. W. — "Steady Flow Through Non-Uniform Gauzes of Arbitrary Shape," J. Fluid Mech., 5, 3, 1959, p. 355.

31. Lau, Y. L. Baines, W. D. — "Flow of Stratified Fluid Through Curved Screens," J. Fluid Mech., 33, 4, 1968, p. 721.

32. Bradshaw, P. — "The Effect of Wind-Tunnel Screens on Nominally Two-Dimensional Boundary Layers," J. Fluid Mech., 22, 4, 1965, p. 679.

33. de Bray, B. G. — "Some Investigations Into the Spanwise Non-Uniformity of Nominally Two-Dimensional Incompressible Boundary Layers Downstream of Gauze Screens," British Aeronautical Research Council, Report No. 29-271, 1967.

34. Cowdrey, C. F. — "A Simple Method for the Design of Wind-Tunnel Velocity-Profile Grids," National Physical Laboratory Aero. Note 1055, 1967.

35. Turner, J. T. — "A Computational Method for the Flow Through Non-Uniform Gauzes: The Two-Dimensional Case," J. Fluid Mech., 36, 2, 1969, p. 367.

36. Livesey, J. L. Laws, E. M. — "The Simulation of Internal Flow Velocity Profiles by Means of Shaped Wire Gauze Screens," AIAA Paper No. 72-165, San Diego, California, 1972.

37. Hunt, J. C. R. — "The Effect of Single Buildings and Structures," Phil. Trans. Roy. Soc. Lond. A, 269, 1971, p. 457.

38. Hunt, J. C. R. — "A Theory of Turbulent Flow Over Bodies," To Be Published.

39. Bradshaw, P. — "Variations on a Theme of Prandtl," AGARD-CP-93, No. C, 1971.

40. Bearman, P. W. — "Some Measurements of the Distortion of Turbulence Approaching a Two-Dimensional Bluff Body," J. Fluid Mech., 53, 3, 1972, p. 451.

41. Batchelor, G. K. — The Theory of Homogeneous Turbulence, Cambridge University Press, 1967.

42. Townsend, A. A. — The Structure of Turbulent Shear Flow, Cambridge University Press, 1956.

43. Hinze, J. O. — Turbulence - An Introduction to Its Mechanism and Theory, McGraw-Hill Book Co., 1959.

44. Champagne, F. H. Harris, V. G. Corrsin, S. — "Experiments on Nearly Homogeneous Turbulent Shear Flow," J. Fluid Mech., 41, 1, 1970, p. 81.

45. Rose, W. G. — "Interaction of Grid Turbulence with a Uniform Mean Shear," J. Fluid Mech., 44, 4, 1970, p. 767.

46. Snyder, W. H. Lumley, J. L. — "Some Measurements of Particle Velocity Autocorrelation Functions in a Turbulent Flow," J. Fluid Mech., 48, 1, 1971, p. 41.

47. Kellogg, R. M. — "Evaluation of a Spectrally Local Disturbance in a Grid-Generated Turbulent Flow," Ph.D. Dissertation, The Johns Hopkins University, 1965.

48. Kellogg, R. M.
Corrsin, S.
"Response of Grid Generated Turbulence to a Spectrally Local Perturbation," Presented at the 18th Physics of Fluids Annual Meeting of the American Physical Society, 1965.

49. Charnay, G.
Comte-Bellot, G.
Mathiue, J.
"Development of a Turbulent Boundary Layer on a Flat Plate in an External Turbulent Flow," AGARD-CP-93, No. 27, 1971.

50. Lumley, J. L.
"Passage of a Turbulent Stream Through Honeycomb of Large Length-to-Diameter Ratio," J. Basic Eng., Trans. ASME, Series D, 86, 1964, p. 218.

51. Lumley, J. L.
McMahon, J. F.
"Reducing Water Tunnel Turbulence by Means of a Honeycomb," J. Basic Eng., Trans. ASME, Series D, 89, 1967, p. 764.

52. De Wiest, R. J. M.
Flow Through Porous Media, Academic Press, 1969.

53. Johnson, B. V.
"Exploratory Experimental Study of the Effects of Inlet Conditions on the Flow and Containment Characteristics of Coaxial Flows," NASA CR-107051, 1969.

54. Bennett, J. C.
Johnson, B. V.
"Experimental Study of One- and Two-Component Low-Turbulence Confined Coaxial Flows," NASA CR-1651, 1971.

55. Kunze, J. F.
Suckling, D. H.
Cooper, C. G.
"Flowing Gas, Non-Nuclear Experiments on the Case Core Reactor," NASA CR-120824, 1972.

56. Nagib, H. M.
Lavan, Z.
Fejer, A. A.
Wolf, L., Jr.
"Stability of Pipe Flow with Superposed Solid Body Rotation," Phys. Fluids, 14, 4, 1971, p. 766.

57. Hannemann, R. J.
"Evaluation of Tubular Flow Straighteners in a Small Scale, Low Speed Wind Tunnel," B.S. Thesis, Illinois Institute of Technology, 1970.

58. Yung, J. T.
"Experiments on Jet Mixing and an Environmental Wind Tunnel Evaluation," B.S. Thesis, Illinois Institute of Technology, 1972.

59. Nagib, H. M.
Way, J. L.
"On a Technique of Noise Measurements for Hot-Wire Systems and the Evaluation of Extremely Low Turbulence Intensities," To Be Published.

60. Tan-atichat, J.
"Construction and Evaluation of Passive Flow Manipulators in Water," B.S. Thesis, Illinois Institute of Technology, 1972.

61. Schraub, F. A.
Kline, S. J.
Henry, J.
Runstadler, P. W.
Littell, A., Jr.
"Use of Hydrogen Bubble for Quantitative Determination of Time Dependent Velocity Fields in Low-Speed Water Flows," J. Basic Eng., Trans. ASME, Ser. D, 87, 1965, p. 429.

62. Loehrke, R. I.
Nagib, H. M.
"Experiments on Management of Free-Stream Turbulence," Super 8mm Movie, 22 Mins., Available on loan from MMAE Dept., I.I.T., Chicago, Ill, 60616, U.S.A.; To be deposited in the Engineering Societies' Library, New York, in the near future.

63. Corrsin, S.
"Outline of Some Topics in Homogeneous Turbulent Flow," J. Geophysical Research, 64, 12, 1959, p. 2134.

64. Roshko, A.
"On the Development of Turbulent Wakes from Vortex Streets," NACA Report-1191, 1955.

65. Sato, H.
"The Stability and Transition of Two-Dimensional Jet," J. Fluid Mech., 7, 1, 1960, p. 53.

66. Bradshaw, P.
"The Effect of Initial Conditions on the Development of a Free Shear Layer," J. Fluid Mech., 26, 2, 1966, p. 225

67. Tsuji, H.
"A Contribution to the Energy Decay Law of Isotropic Turbulence in the Initial Period," Aero. Res. Inst., Univ. Tokyo, Report No. 345, 1959.

68. Morkovin, M. V.
"Flow Around Circular Cylinder - a Kaleidoscope of Challenging Fluid Phenomena," Symposium on Fully Separated Flows, ASME, 1964, p. 102.

69. Uberoi, M. S.
"Effect of Wind-Tunnel Contractions on Free-Stream Turbulence," J. Aeronaut. Sci., 23, 1956, p. 754.

70. Corrsin, S. — "Decay of Turbulence Behind Three Similar Grids," Dissertation for A.E. degree, Aero. Engineering Dept., California Institute of Technology, 1942.

71. Parker, R. — "Resonance Effects in Wake Shedding from Parallel Plates: Calculation of Resonant Frequency," Journal of Sound and Vibration, 5, 2, 1967, p. 330.

72. Morkovin, M. V.; Loehrke, R. I.; Fejer, A. A. — "On the Response of Laminar Boundary Layers to Periodic Changes in Free-Stream Speed," Proc. 1971 IUTAM Sympo. on Unsteady Boundary Layers, 1972. Also AFOSR-TR 71-2317.

73. Batchelor, G. K. — "Sound in Wind Tunnels," Australian Council of Aeronautics, Rep. A.C.A., 18, 1945.

74. Beckwith, I. E.; Stainback, P. C. — "Transition Research and Prospects for a Mach 3 to 7 Quiet Tunnel," NASA LWP-1064, 1972.

75. Morkovin, M. V. — "An Approach to Flow Engineering Via Functional Flow Modules," Deutsche Luft-und Raumfahrt, Forschungsbericht 72-27, Teil 2, 1972, p. 270.

76. Morkovin, M. V. — "On Supersonic Wind Tunnels with Low Free Stream Disturbances," J. Appl. Mech., Trans. ASME, Series E, 81, 3, 1959, p. 319; Discussion Ibid., 82, 2, 1960, p. 362.

77. Brown, G.; Roshko, A. — "The Effect of Density Difference on the Turbulent Mixing Layer," AGARD-CP-93, No. 23, 1971.

78. Crow, S. C.; Champagne, F. H. — "Orderly Structure of Jet Turbulence," J. Fluid Mech., 48, 3, 1971, p. 547.

79. Lumley, J. L. — "The Structure of Inhomogeneous Turbulent Flows," Proc. Int. Coll. Atmospheric Turbulence and Radio Wave Propagation, A.M. Yaglom, Editor, Moscow, 1965.

80. Corino, E. R.; Brodkey, R. S. — "A Visual Investigation of the Wall Region in Turbulent Flow, J. Fluid Mech., 37, 1, 1969, p. 1.

81. Gupta, A. K.; Laufer, J.; Kaplan, R. E. — "Spatial Structure in the Viscous Sublayer," J. Fluid Mech., 50, 3, 1971, p. 493.

82. Kline, S. J.; Reynolds, W. C.; Schraub, F. A.; Runstadler, P. W. — "The Structure of Turbulent Boundary Layers," J. Fluid Mech., 30, 4, 1967, p. 741.

APPENDIX

DETAILS OF WIND TUNNEL DESIGN

The wind tunnel design evolved during a senior research project of Robert Hannemann[57], aimed at the design and construction of a hot-wire anemometer calibration facility. Indeed, the genesis of the manipulator studies was Hannemann's early measurement on the reduction of turbulence through the use of straws.

An assembly drawing of the tunnel in the calibration configuration is shown in Fig. 87. Compressed air is introduced into an acoustically treated plenum chamber. Air from the plenum chamber enters a section of 2.84 in. i.d. plexiglas tubing. In the calibration configuration this section is 20 in. long; the first 10-in. segment is packed with a matrix of straws while the downstream segment provides decay time for the straw-generated turbulence. For calibration at low to moderate velocities the air is then accelerated through a nozzle which provides a 1-in. diameter free jet for probe calibration. This final contraction, area ratio 8:1, further reduces the fluctuation level in the calibration stream and yields a jet with a flat mean profile and u'/U below 0.05%. Mean velocities up to about 120 fps with shop air supply of about 100 psig are achieved with this arrangement.

Hannemann[57] designed the tunnel so that by simply removing the nozzle, probe access was provided to a 2.84-in. diameter, closed test section. He used this test section to evaluate candidates for turbulence dampers to be used in the calibration facility.

An assembly drawing of the test section in this configuration is shown in Fig. 88. The turbulence manipulators are held in place by compression between segments of tubing and making flanges, flange B. The Dacron screen segments were cut larger than the tube o.d. and folded back over the outer surface of the tube. The clearance between the tube o.d. and the matching flange i.d. was just sufficient so that when the two pieces were pressed together the screen is stretched taut across the test section. The straws were simply packed in a tube segment and held by friction.

Flange A is bolted through the plenum chamber to the bellmouth block and provides an anchor for the tie-rods which hold the entire test section assembly in compression. Additional support for the test section at the exit end, and for long test section assemblies, is provided by table mounted bases, one of which is shown in Fig. 87, midway between the plenum chamber and the exit. Construction details and dimensions of the major components of the tunnel are presented in Figs. 89 and 93.

The baffles and fiberglass lining in the plenum chamber were designed to absorb the noise associated with the high velocity jet from the compressed air inlet. With this treatment the lab noise level is low enough so that it does not interfere with normal conversation and is not fatiguing to the operator.

The nozzle and bellmouth contours are given in the detail drawings of these components. The constants in the equations are in inches for r and x.

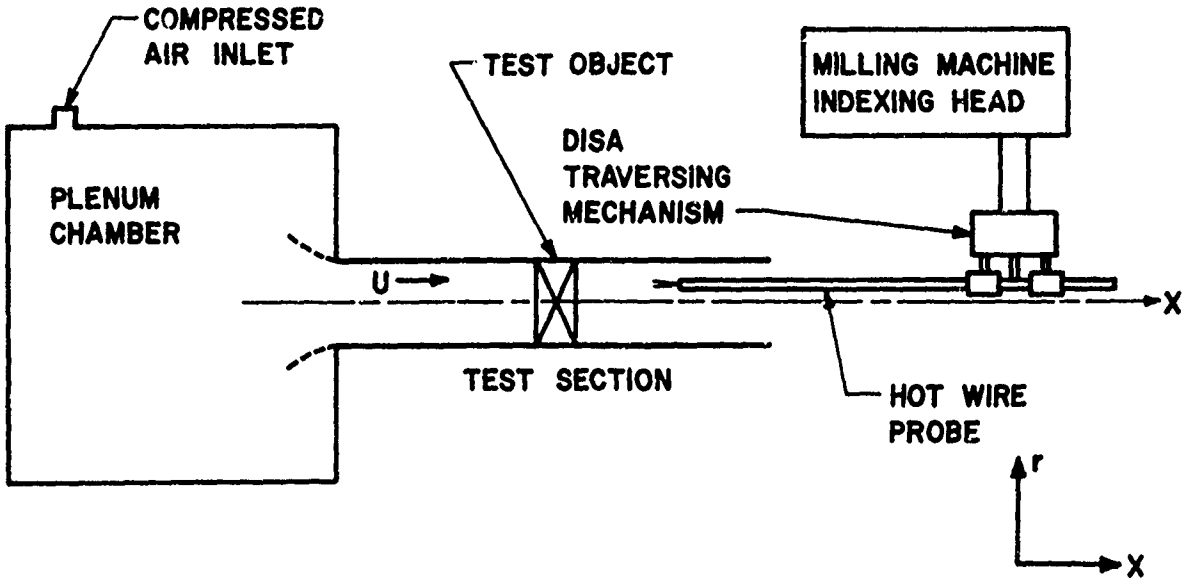

FIG. 1. SCHEMATIC OF WIND TUNNEL AND TRAVERSING MECHANISM SET FOR AUTOMATIC AXIAL TRAVERSING.

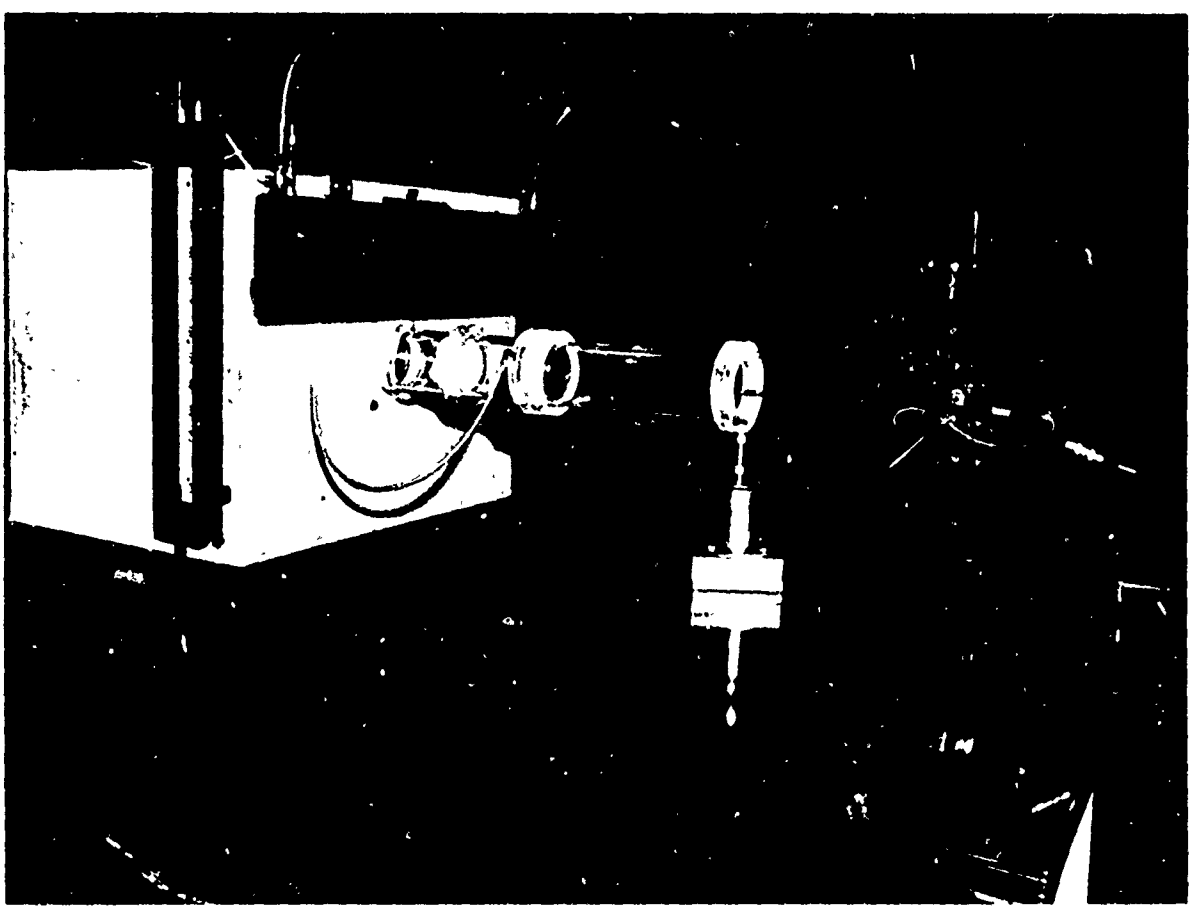

FIG. 2. PHOTOGRAPH OF WIND TUNNEL.

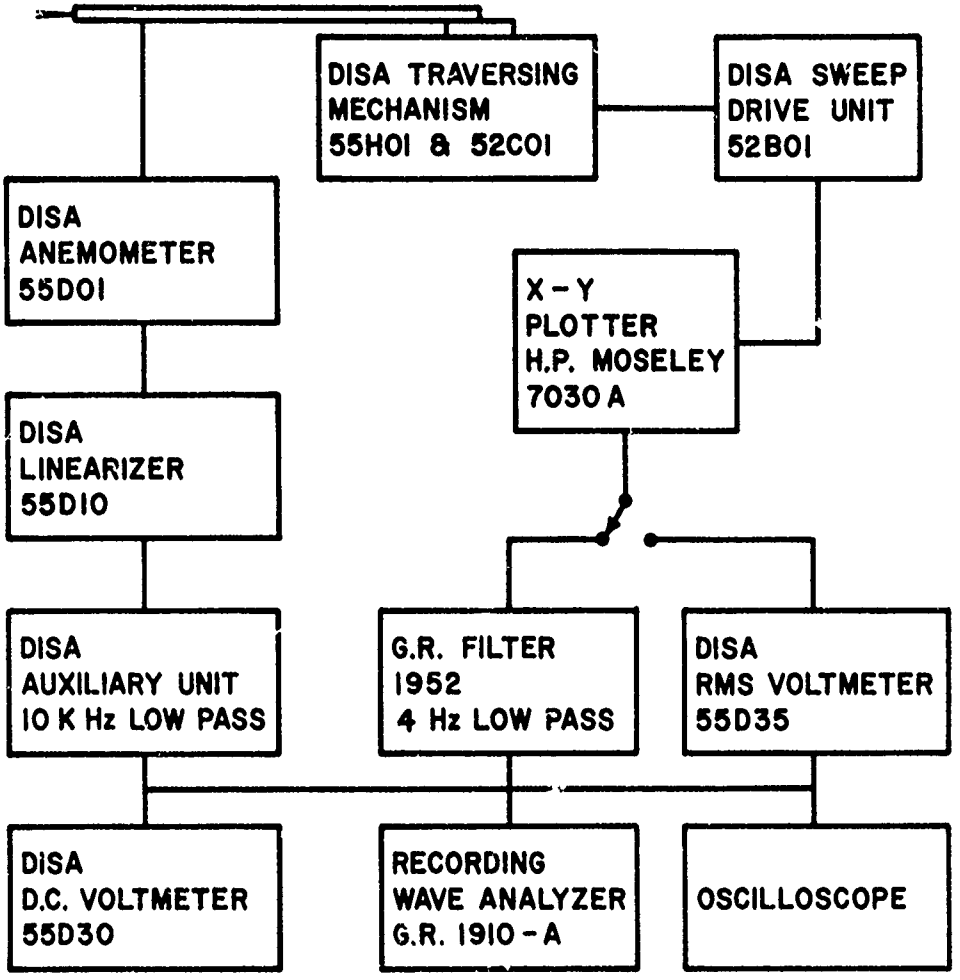

FIG. 3. INSTRUMENTATION SCHEMATIC.

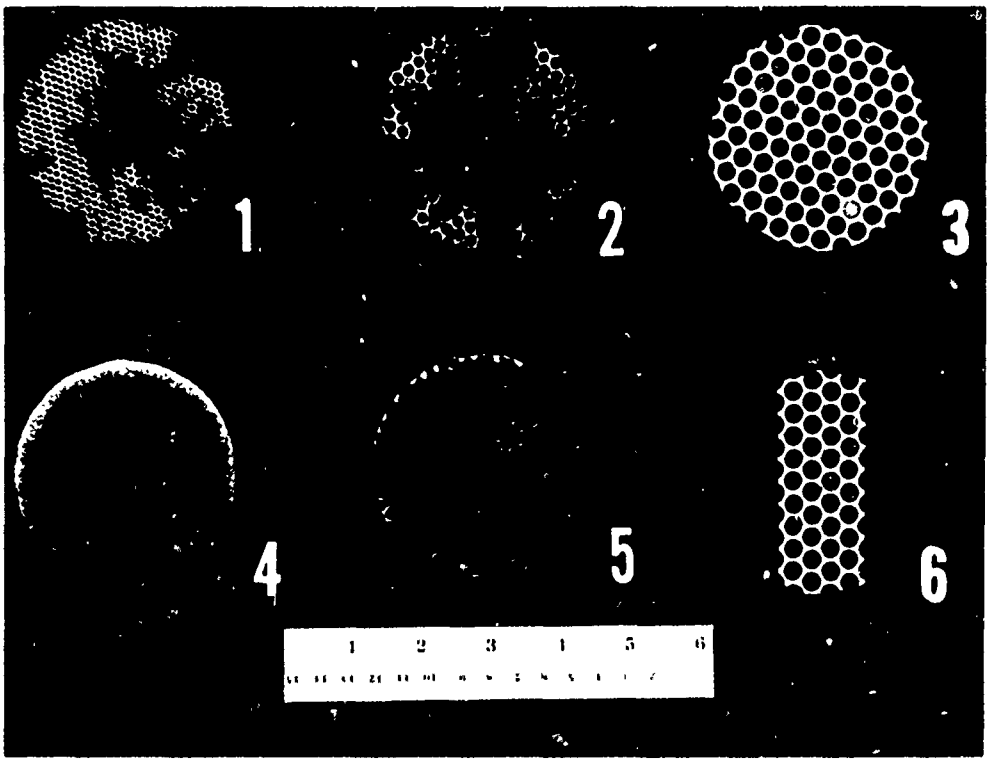

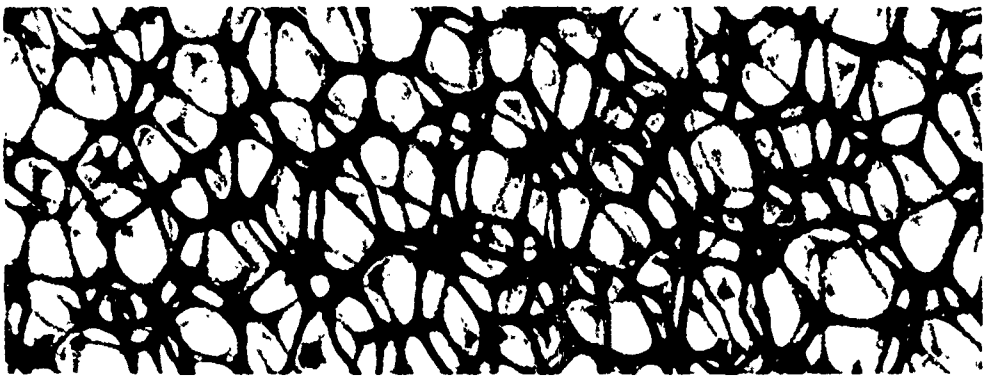

Enlarged Thin Section Of Foam Material

FIG. 4A. PHOTOGRAPHS OF TURBULENCE MANIPULATORS.

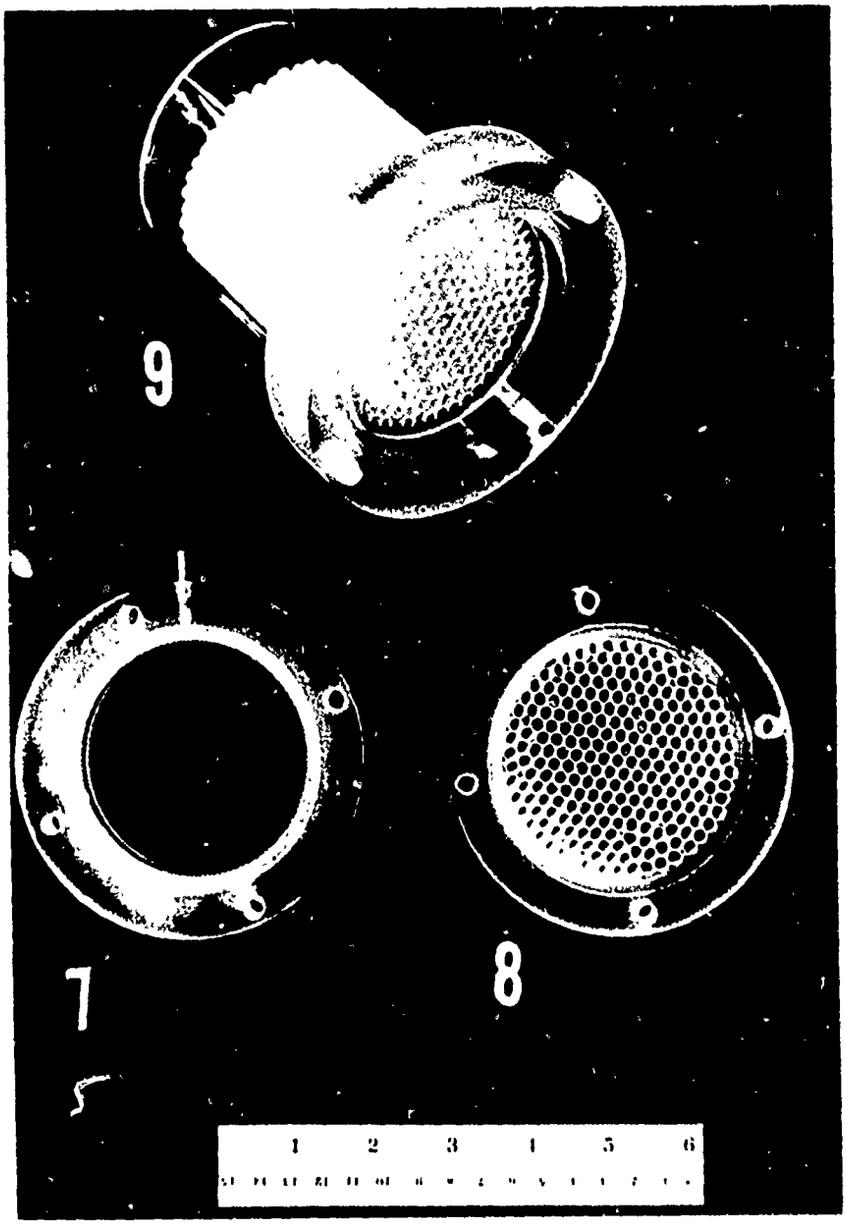

FIG. 4B. PHOTOGRAPHS OF TURBULENCE MANIPULATORS.

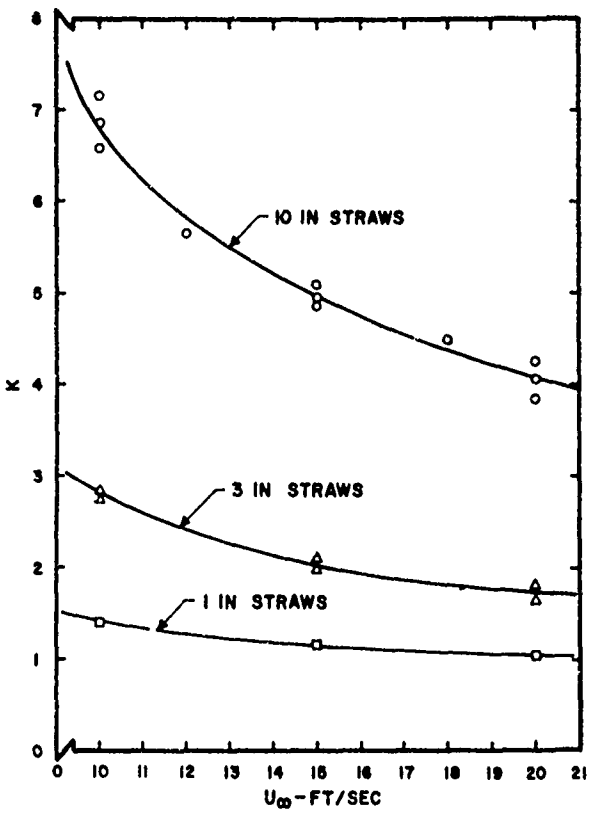

FIG. 5. PRESSURE DROP COEFFICIENT OF STRAWS VS. VELOCITY.

	M (IN)	σ	K*	ℓ (IN)	Re_M^*
SCREENS: 0.005 IN DACRON THREAD	0.033	0.28	0.86	0.005	245
STRAWS: PLASTIC 0.175 IN O.D. 0.006 IN WALL					
1 IN	0.175	0.20	1.2	1.0	1290
3 IN	0.175	0.20	2.1	3.0	1290
10 IN	0.175	0.20	5.0	10.0	1290
STRAWS AND SCREEN:					
1 IN			2.0	1.0	
3 IN			2.9	3.0	
10 IN			5.9	10.0	
FOAM: INDUSTRIAL "SCOTT" POLYURETHANE	0.022	0.03	6.6	0.25	163
PERFORATED PLATES: 1/16 IN STEEL					
P.P.#1 0.0625 IN HOLES	0.109	0.70	7.9	0.063	800
P.P.#2 0.120 IN HOLES	0.188	0.49	2.0	0.063	1380
P.P.#3 0.250 IN HOLES	0.313	0.42	1.5	0.063	2300
PERFORATED PLATES AND FOAM:					
P.P.#1			47	0.31	
P.P.#2			25	0.31	

* AT U_∞ = 15 FT/SEC

FIG. 6. TABLE OF TURBULENCE MANIPULATORS PROPERTIES.

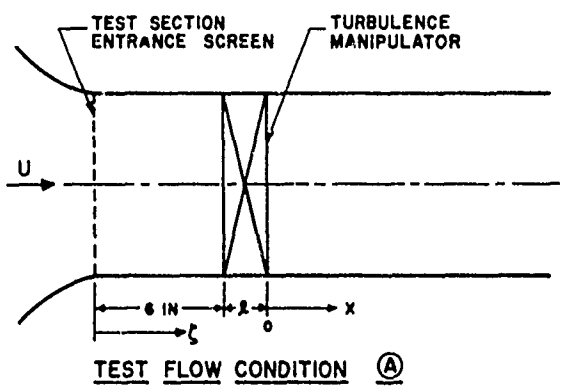

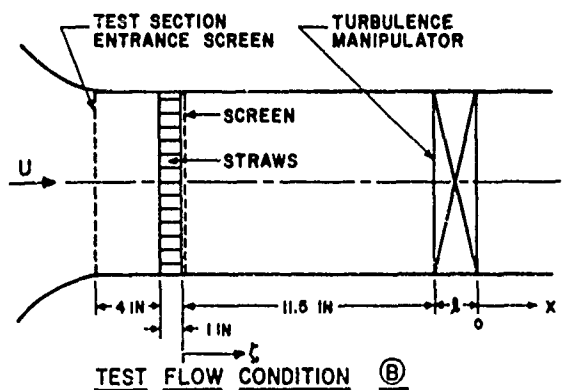

FIG. 7A. SCHEMATIC OF MEANS BY WHICH TEST FLOW CONDITIONS ARE GENERATED.

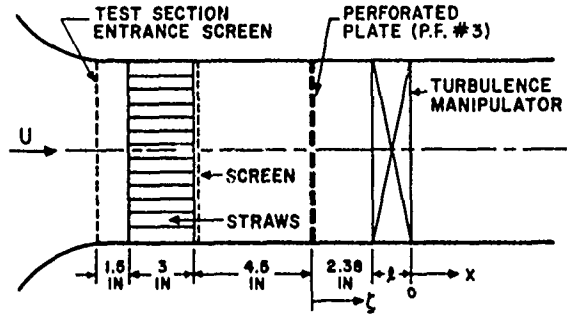

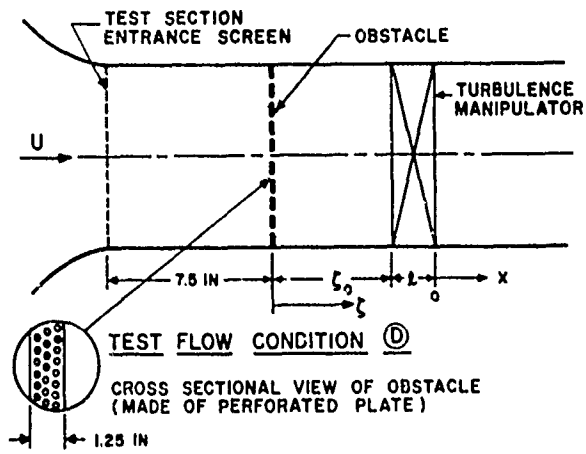

FIG. 7B. SCHEMATIC OF MEANS BY WHICH TEST FLOW CONDITIONS ARE GENERATED.

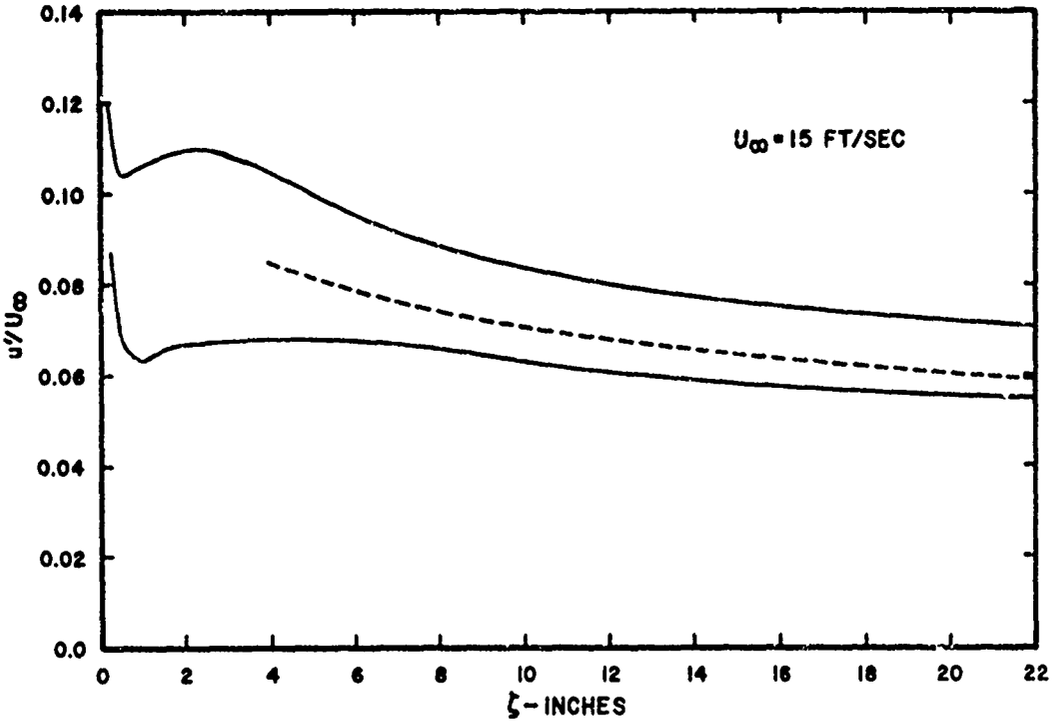

FIG. 8. AXIAL PROFILE OF u'/U_∞ FOR TEST FLOW CONDITION "A".

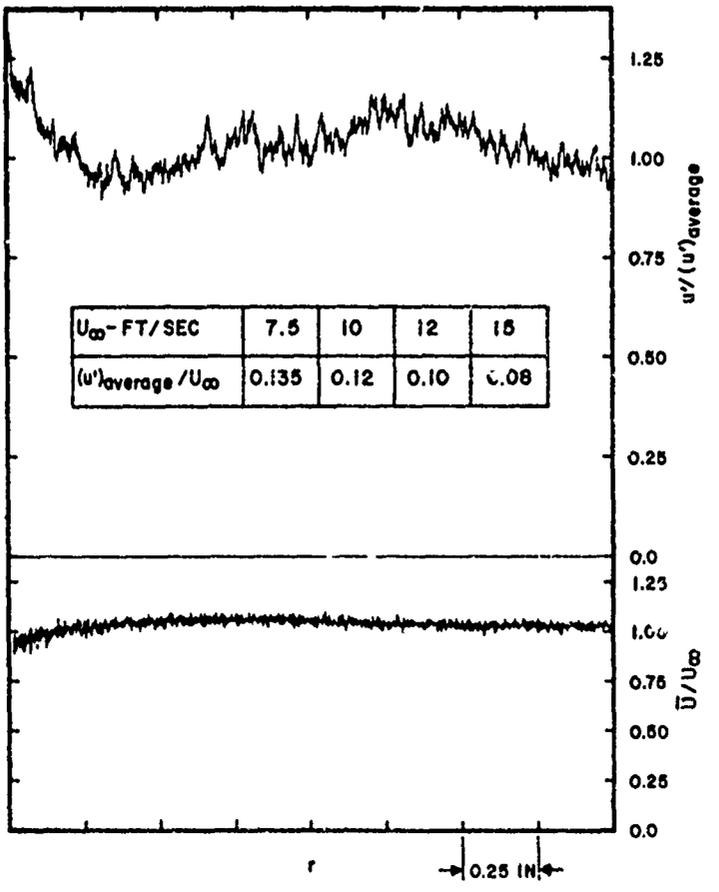

FIG. 9. RADIAL PROFILES OF $\bar{U}$ AND u'/U_∞ AT $\zeta = 6$ IN. FOR TEST FLOW CONDITION "A".

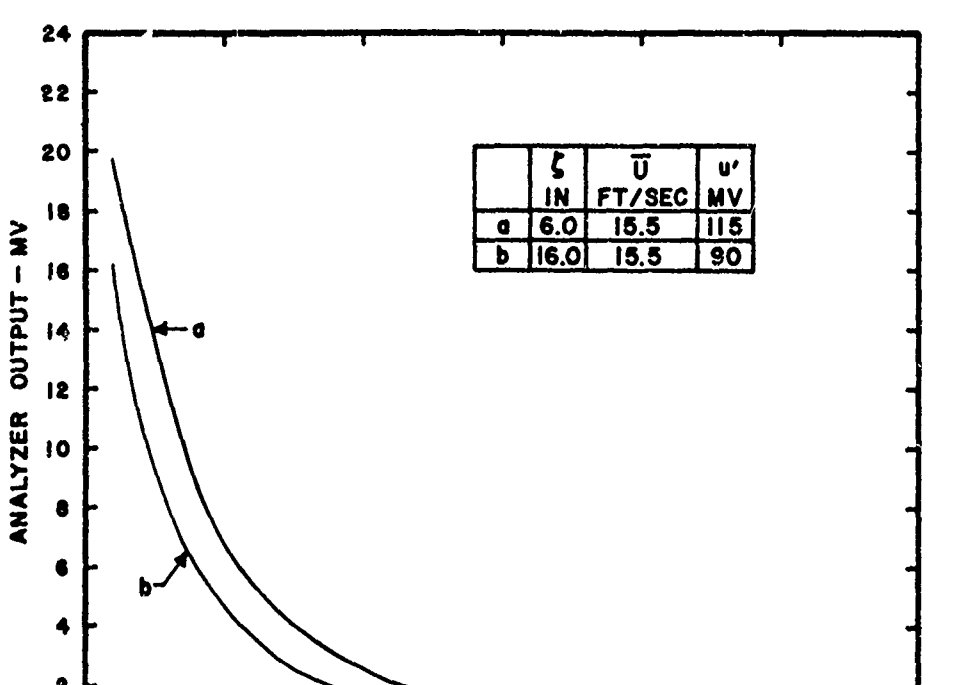

FIG. 10A. SPECTRA OF u AT DIFFERENT AXIAL LOCATIONS FOR TEST FLOW CONDITION "A".

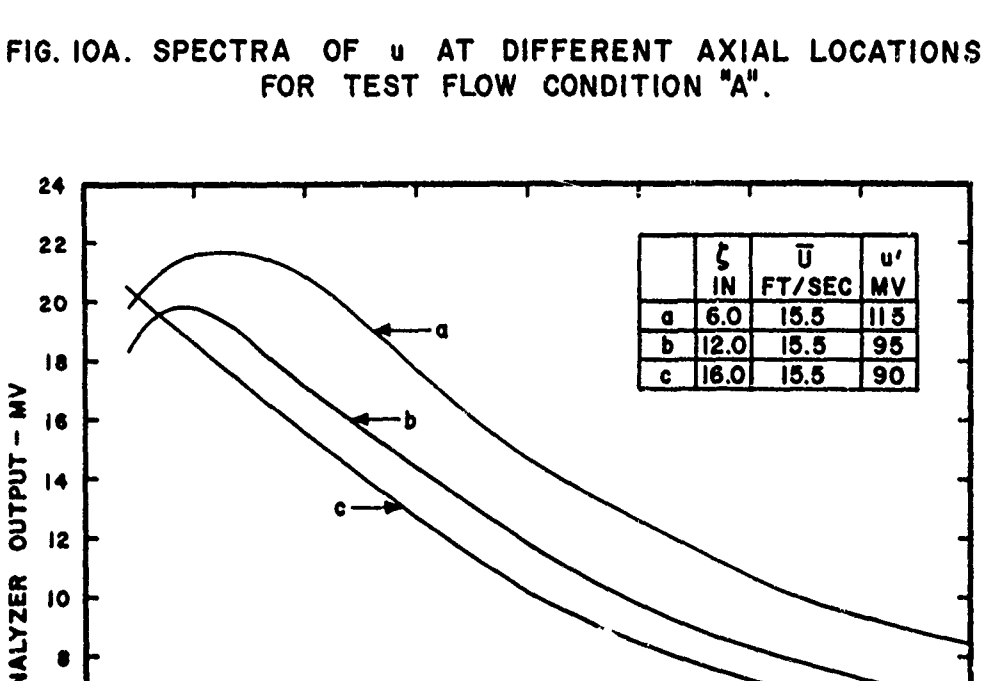

FIG. 10B. SPECTRA OF u AT DIFFERENT AXIAL LOCATIONS FOR TEST FLOW CONDITION "A".

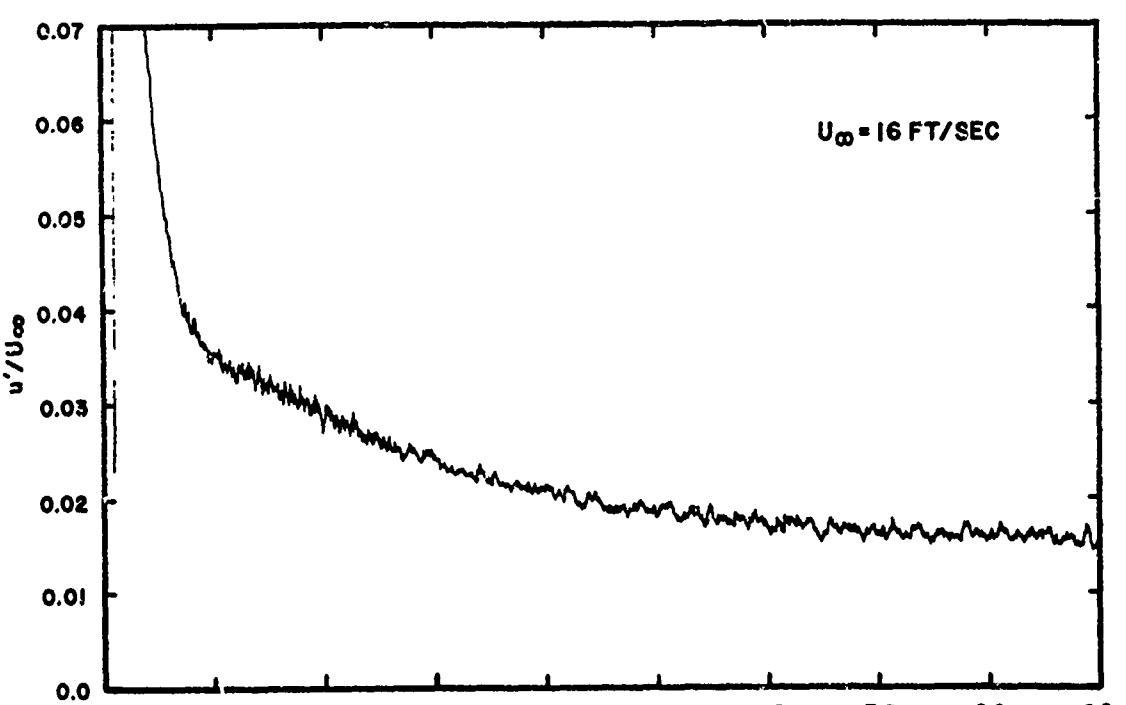

FIG. 11. AXIAL PROFILE OF u'/U_∞ FOR TEST FLOW CONDITION "B".

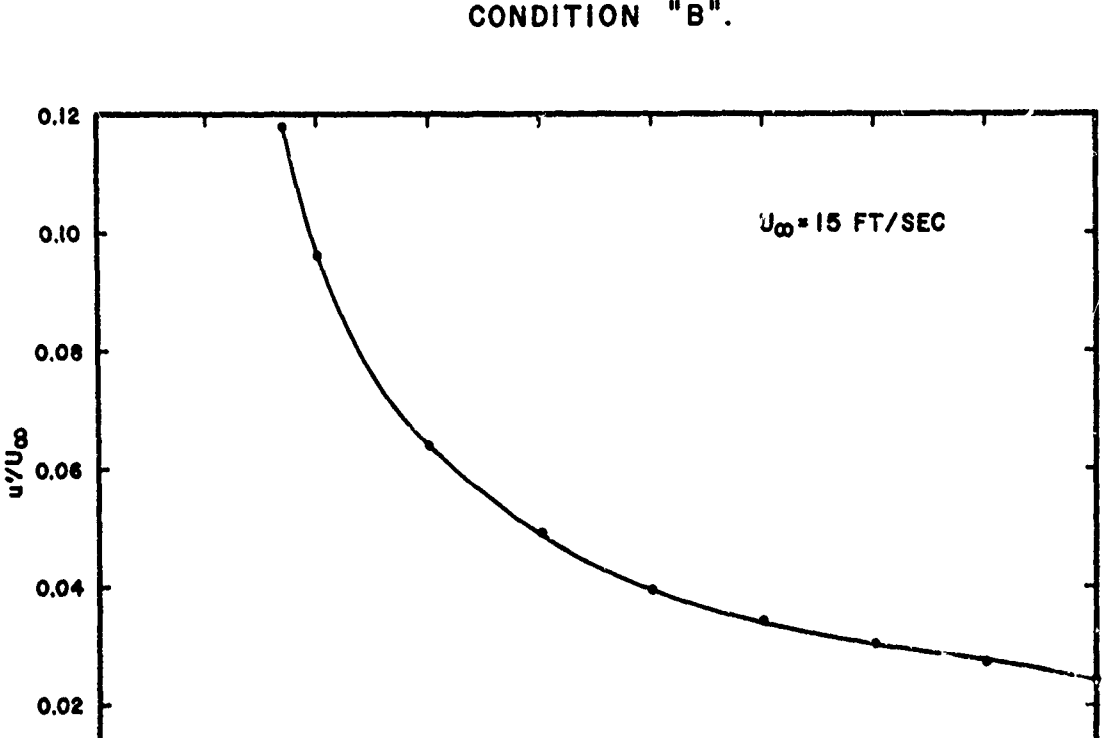

FIG. 12. AXIAL PROFILE OF u'/U_∞ FOR TEST FLOW CONDITION "C".

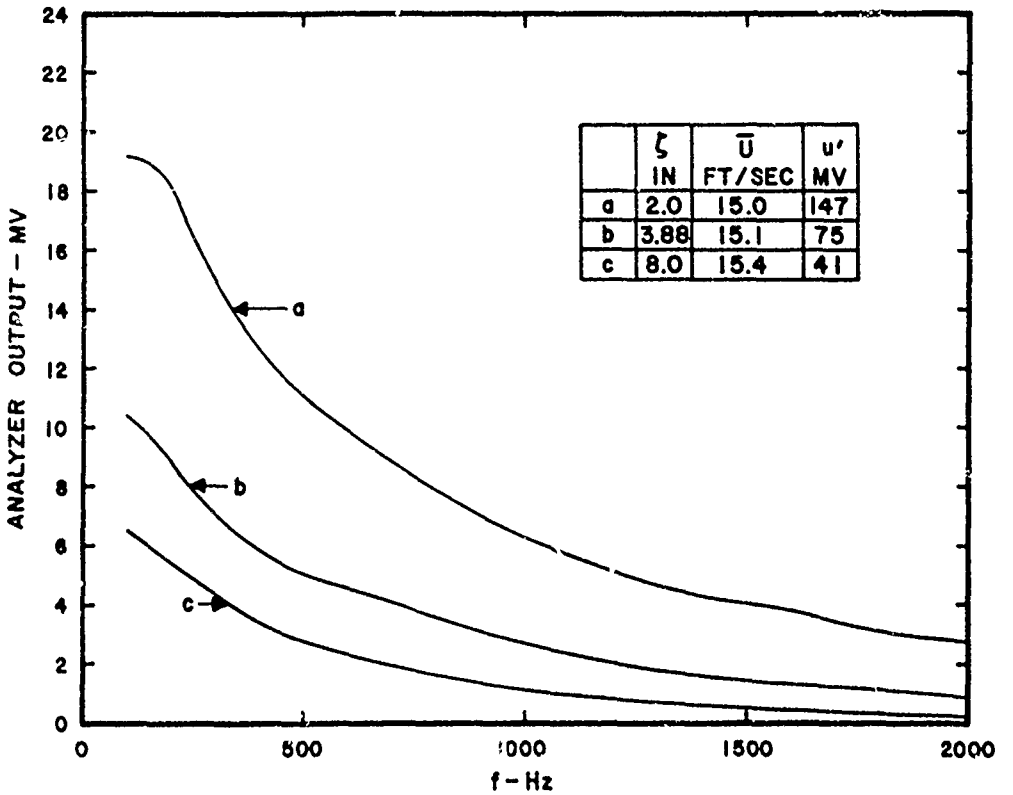

FIG. 13A. SPECTRA OF u AT DIFFERENT AXIAL LOCATIONS FOR TEST FLOW CONDITION "C".

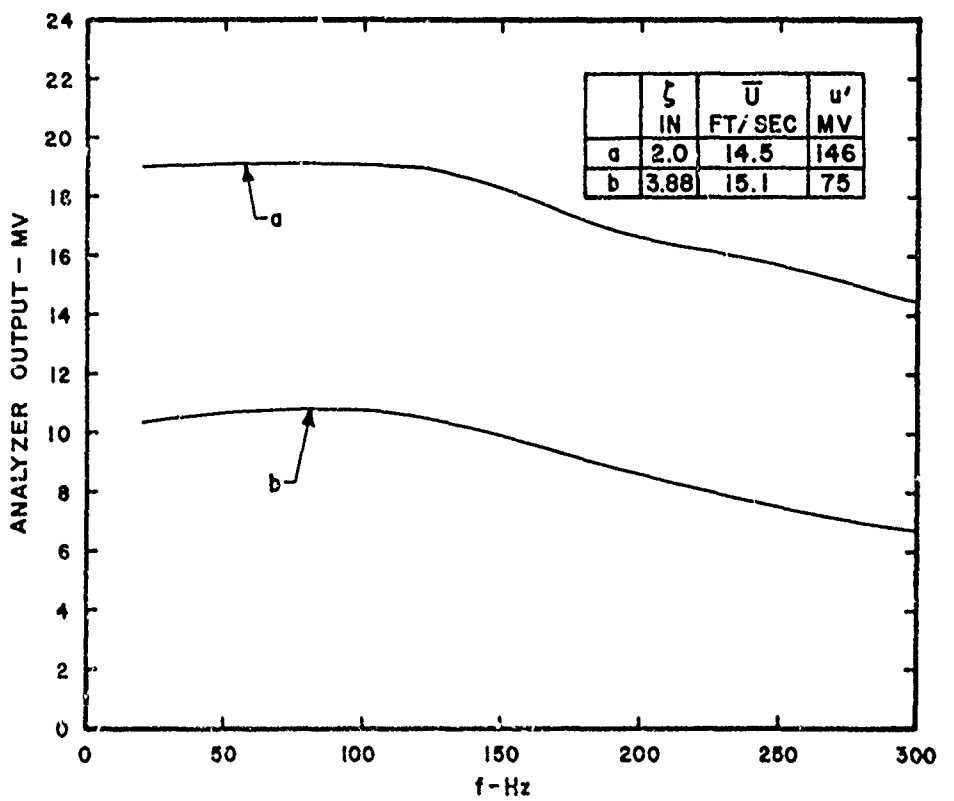

FIG. 13B. SPECTRA OF u AT DIFFERENT AXIAL LOCATIONS FOR TEST FLOW CONDITION "C".

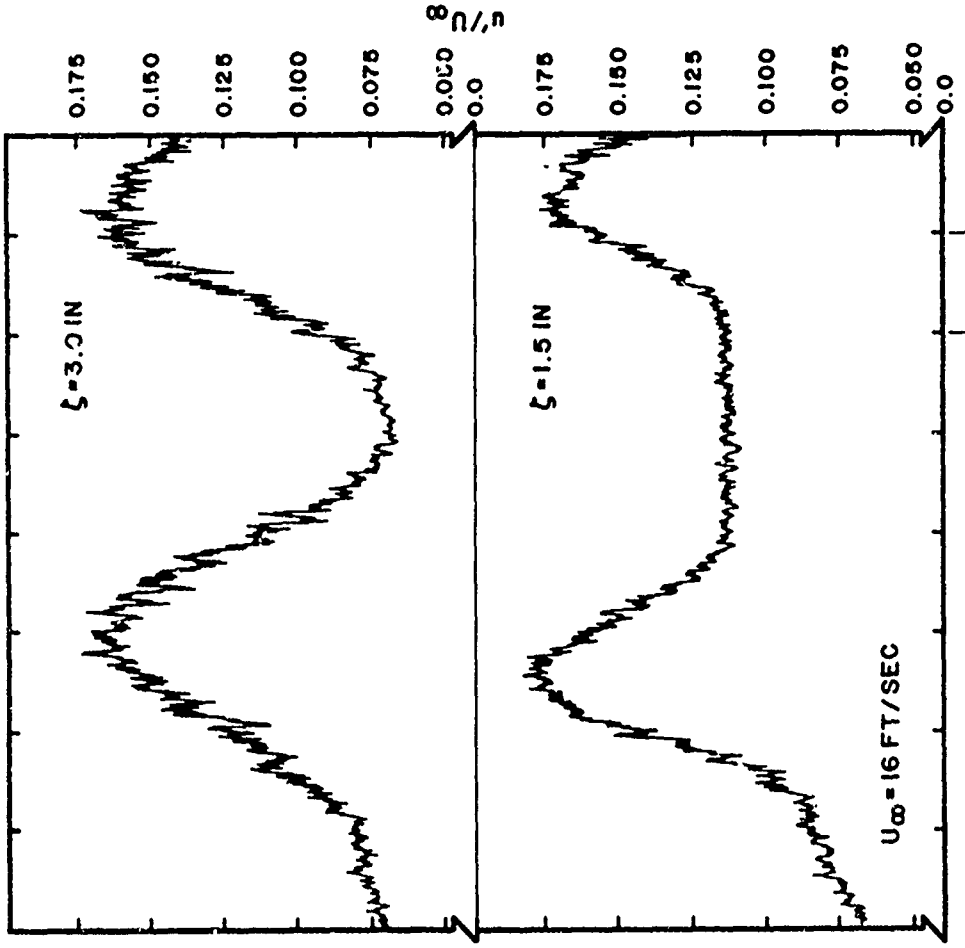

FIG. 14B. RADIAL PROFILES OF $\bar{U}$ AND u'/U_∞ AT ζ=1.5 AND 3 IN. FOR TEST FLOW CONDITION "D".

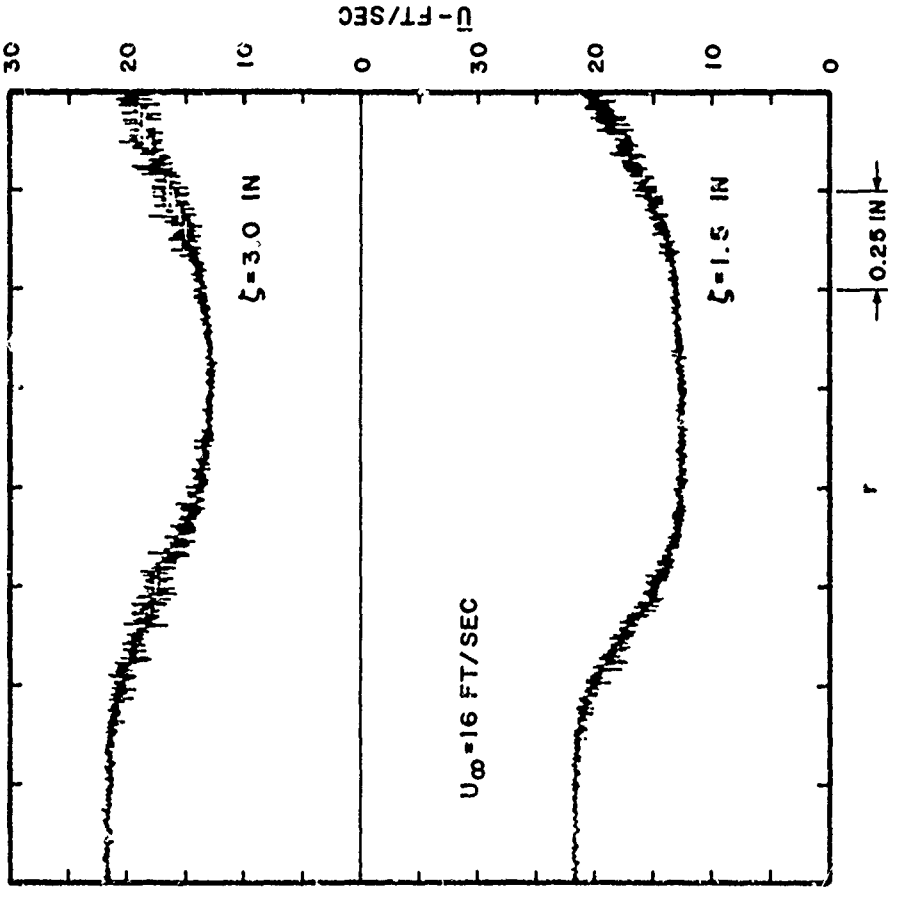

FIG. 14A. RADIAL PROFILES OF $\bar{U}$ AND u'/U_∞ AT ζ=1.5 AND 3 IN. FOR TEST FLOW CONDITION "D".

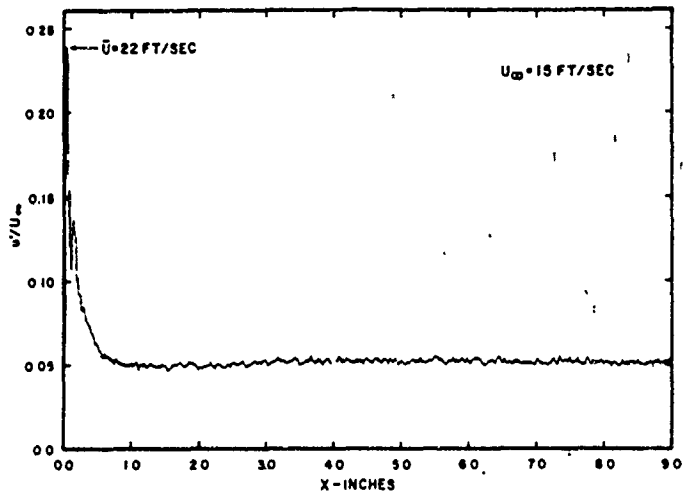

FIG. 15. AXIAL PROFILE OF u'/U_∞ FOR A SINGLE SCREEN IN TEST FLOW CONDITION "A".

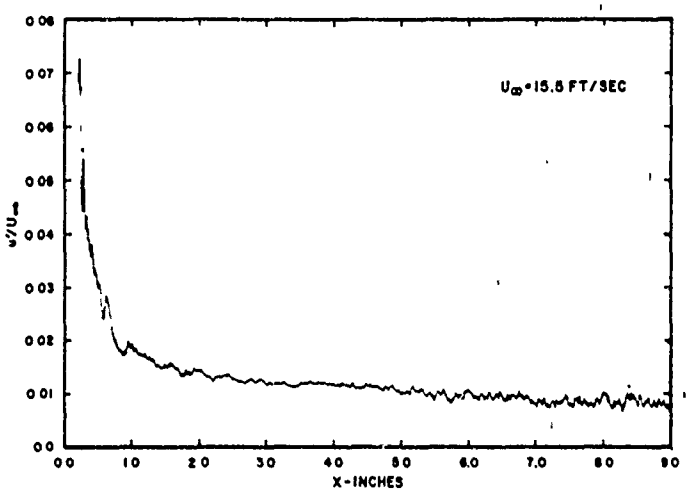

FIG. 16. AXIAL PROFILE OF u'/U_∞ FOR A SINGLE SCREEN IN TEST FLOW CONDITION "B".

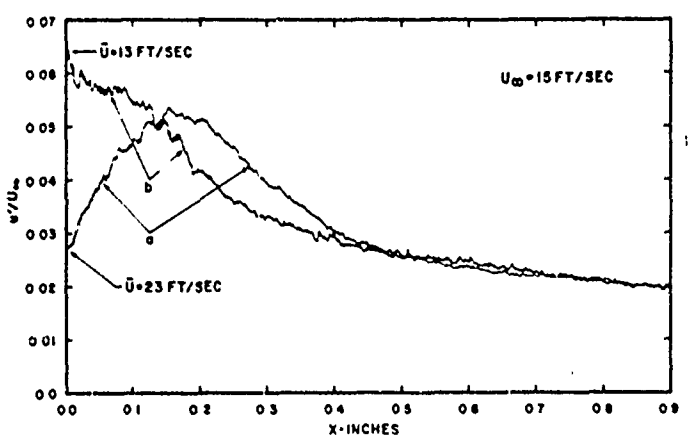

FIG. 17. AXIAL PROFILE OF u'/U_∞ FOR A SINGLE SCREEN IN TEST FLOW CONDITION "B", EXPANDED SCALE.

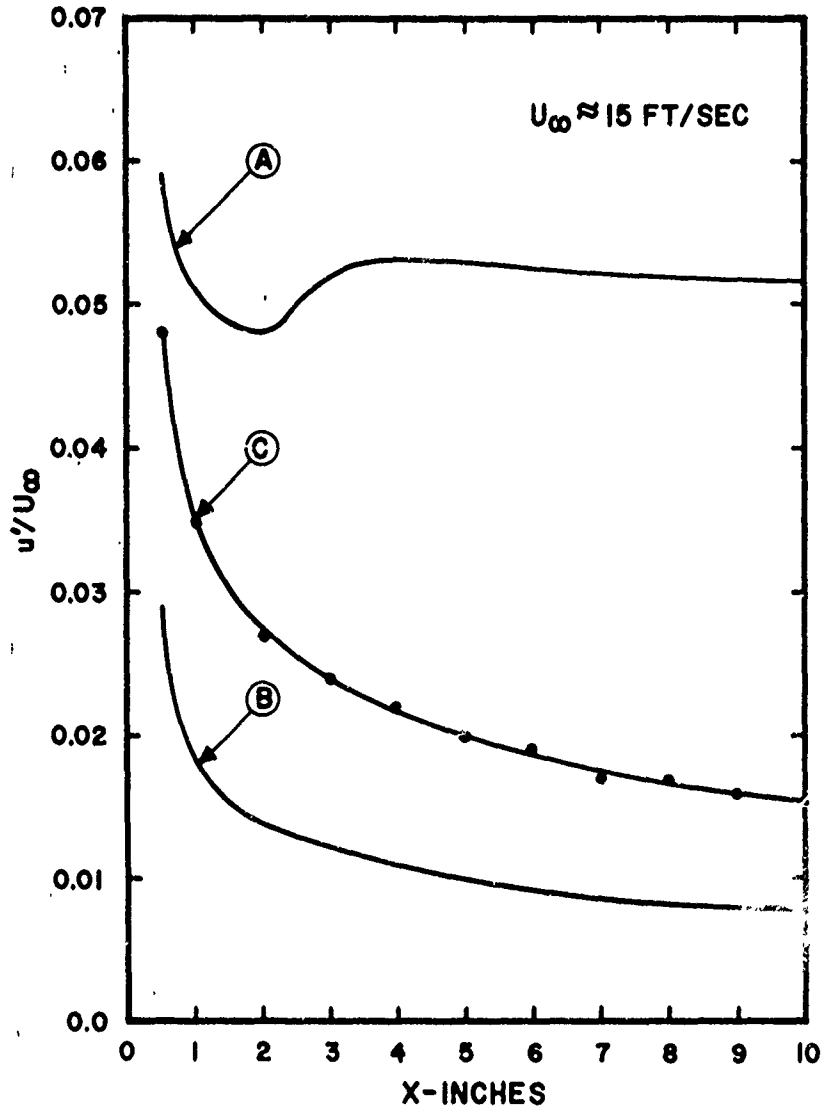

FIG. 18. COMPARISON OF AXIAL PROFILES OF u'/U_∞ FOR A SINGLE SCREEN IN TEST FLOW CONDITIONS "A", "B" AND "C".

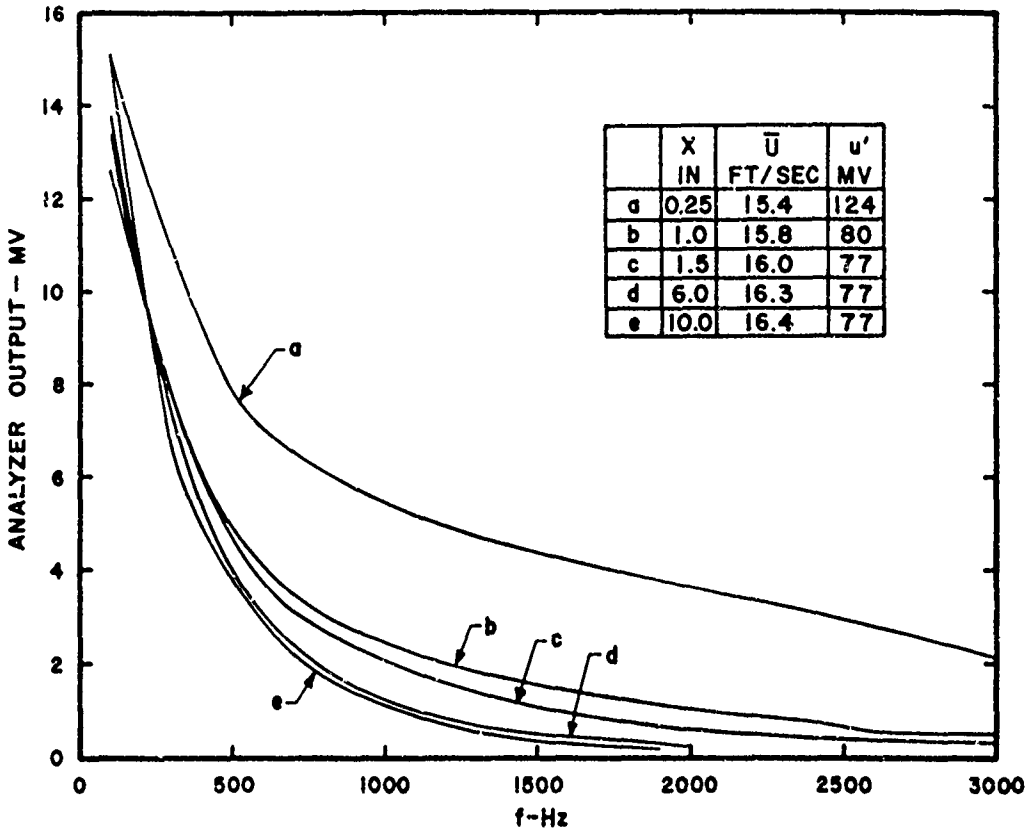

FIG. 19A. SPECTRA OF u AT DIFFERENT AXIAL LOCATIONS FOR A SINGLE SCREEN IN TEST FLOW CONDITION "A".

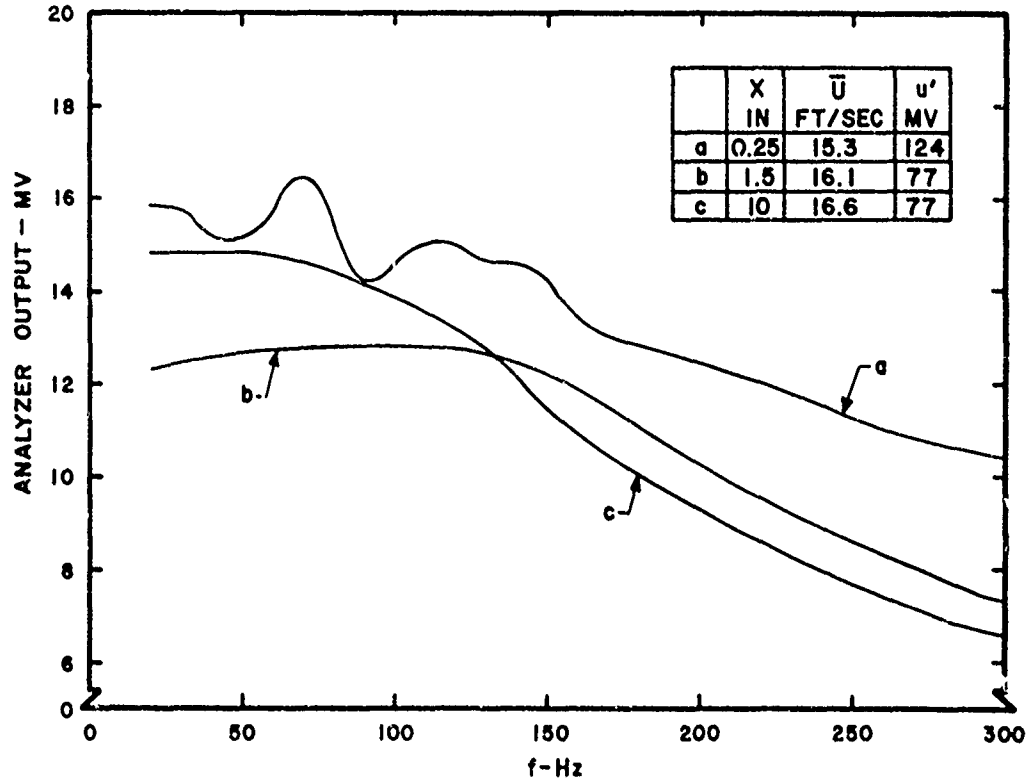

FIG. 19B. SPECTRA OF u AT DIFFERENT AXIAL LOCATIONS FOR A SINGLE SCREEN IN TEST FLOW CONDITION "A".

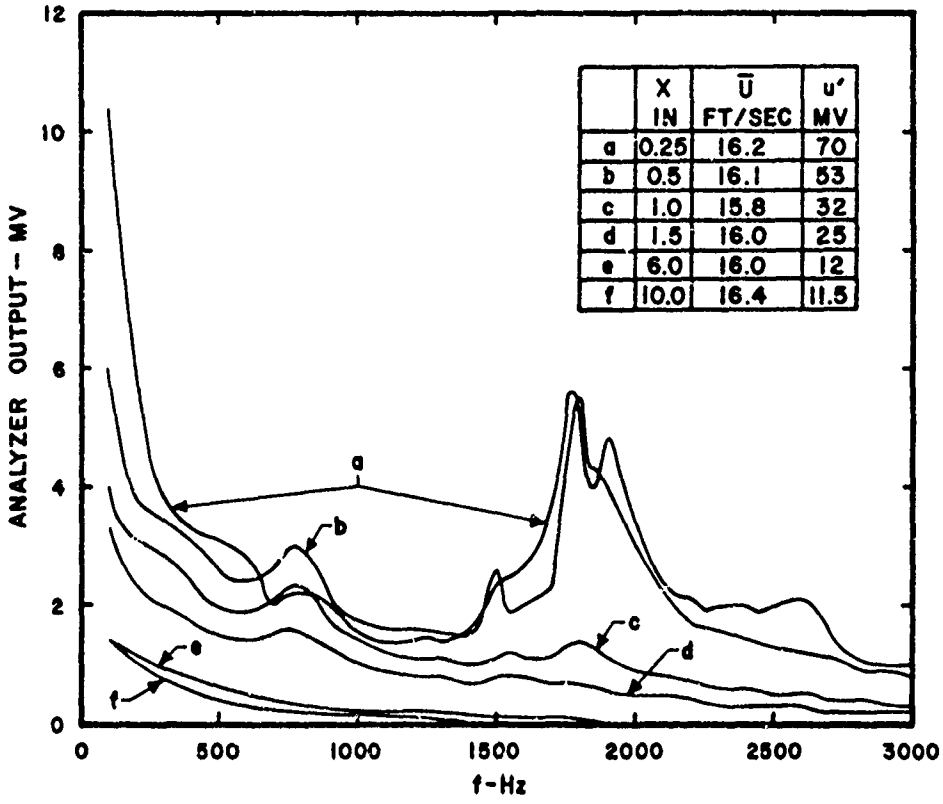

	X IN	$\bar{U}$ FT/SEC	u' MV
a	0.25	16.2	70
b	0.5	16.1	53
c	1.0	15.8	32
d	1.5	16.0	25
e	6.0	16.0	12
f	10.0	16.4	11.5

FIG. 20. SPECTRA OF u AT DIFFERENT AXIAL LOCATIONS FOR A SINGLE SCREEN IN TEST FLOW CONDITION "B".

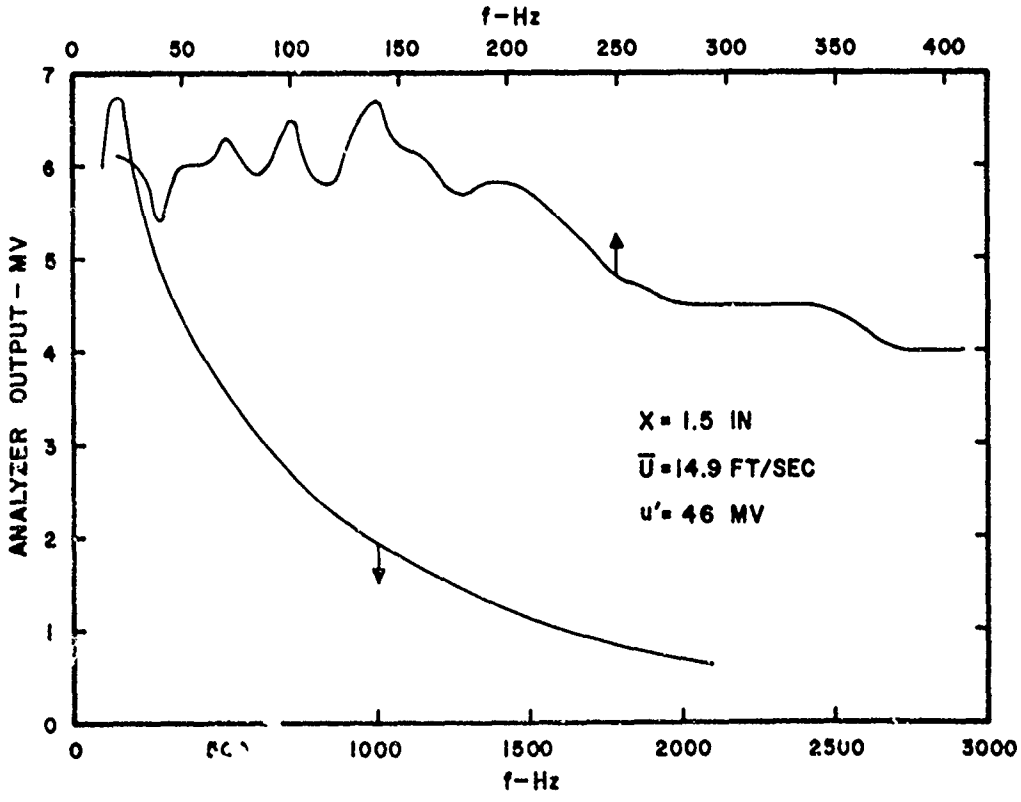

FIG. 21. SPECTRA OF u AT X = 1.5 IN. FOR A SINGLE SCREEN IN TEST FLOW CONDITION "C".

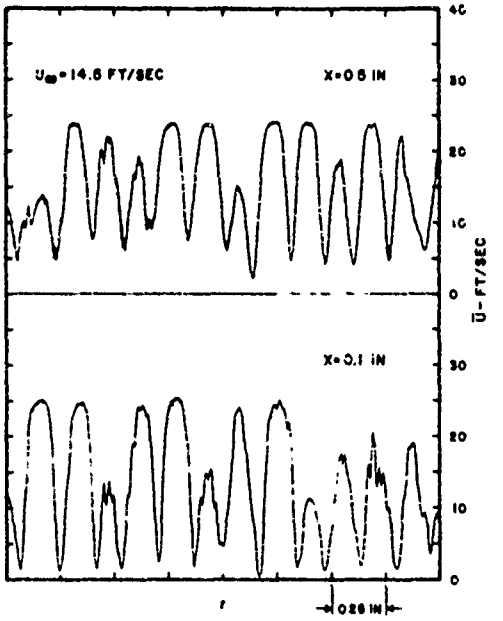

FIG. 22 A. RADIAL PROFILES OF $\bar{U}$ AT DIFFERENT AXIAL LOCATIONS FOR 1 IN. STRAWS IN TEST FLOW CONDITION "A".

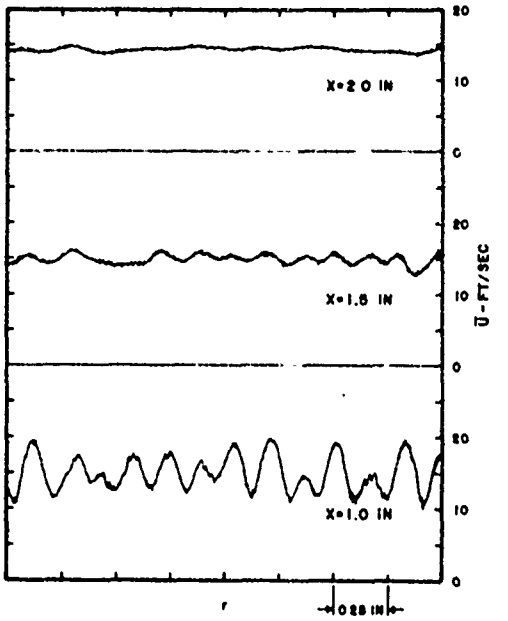

FIG. 22 B. RADIAL PROFILES OF $\bar{U}$ AT DIFFERENT AXIAL LOCATIONS FOR 1 IN. STRAWS IN TEST FLOW CONDITION "A".

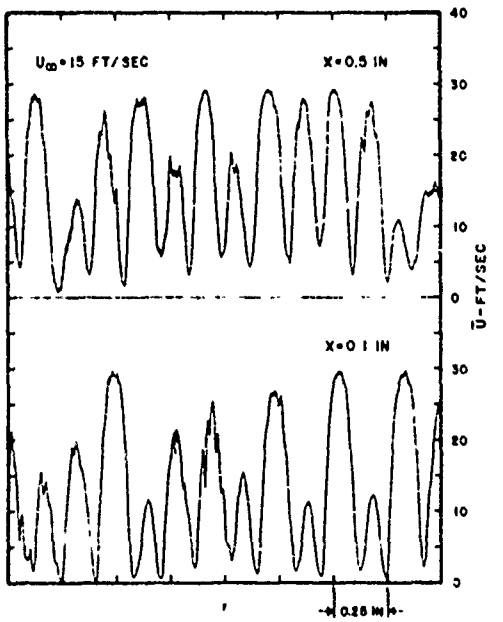

FIG. 23 A. RADIAL PROFILES OF $\bar{U}$ AT DIFFERENT AXIAL LOCATIONS FOR 3 IN. STRAWS IN TEST FLOW CONDITION "A".

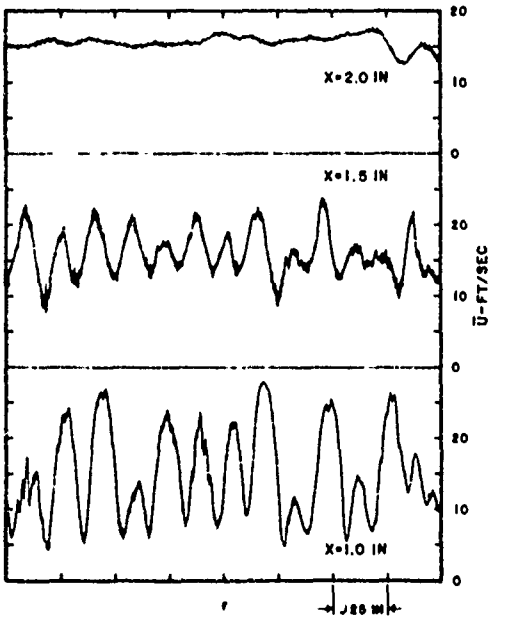

FIG. 23 B RADIAL PROFILES OF $\bar{U}$ AT DIFFERENT AXIAL LOCATIONS FOR 3 IN. STRAWS IN TEST FLOW CONDITION "A".

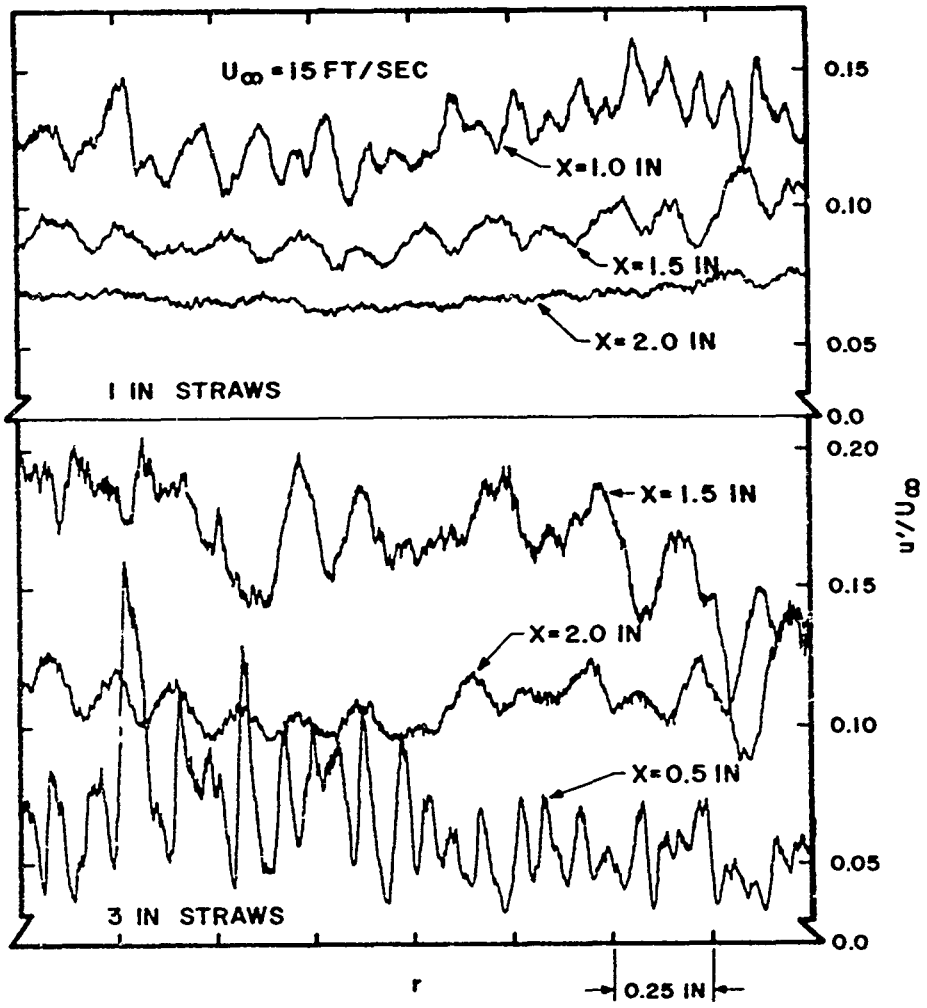

FIG. 24. RADIAL PROFILES OF u'/U_∞ AT DIFFERENT AXIAL LOCATIONS FOR 1 IN. AND 3 IN. STRAWS IN TEST FLOW CONDITION "A".

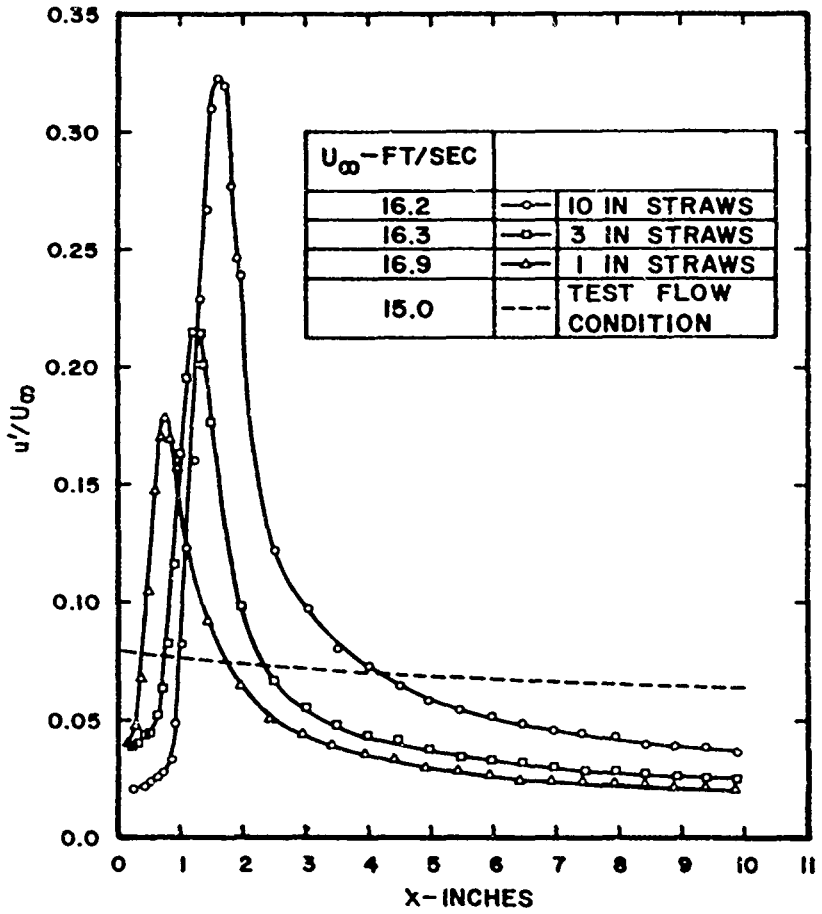

FIG. 25. AXIAL PROFILES OF u'/U_∞ FOR 1 IN., 3 IN., 10 IN. STRAWS IN TEST FLOW CONDITION "A" AND FLOW CONDITION "A".

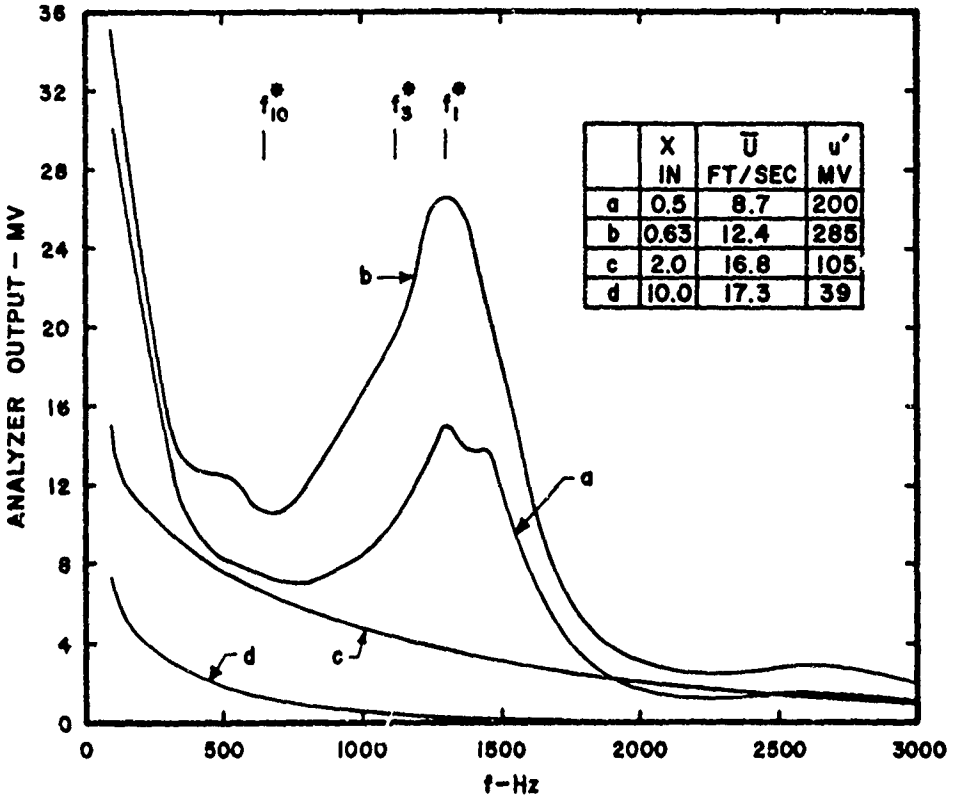

FIG. 26. SPECTRA OF u AT DIFFERENT AXIAL LOCATIONS FOR 1 IN. STRAWS IN TEST FLOW CONDITION "A".

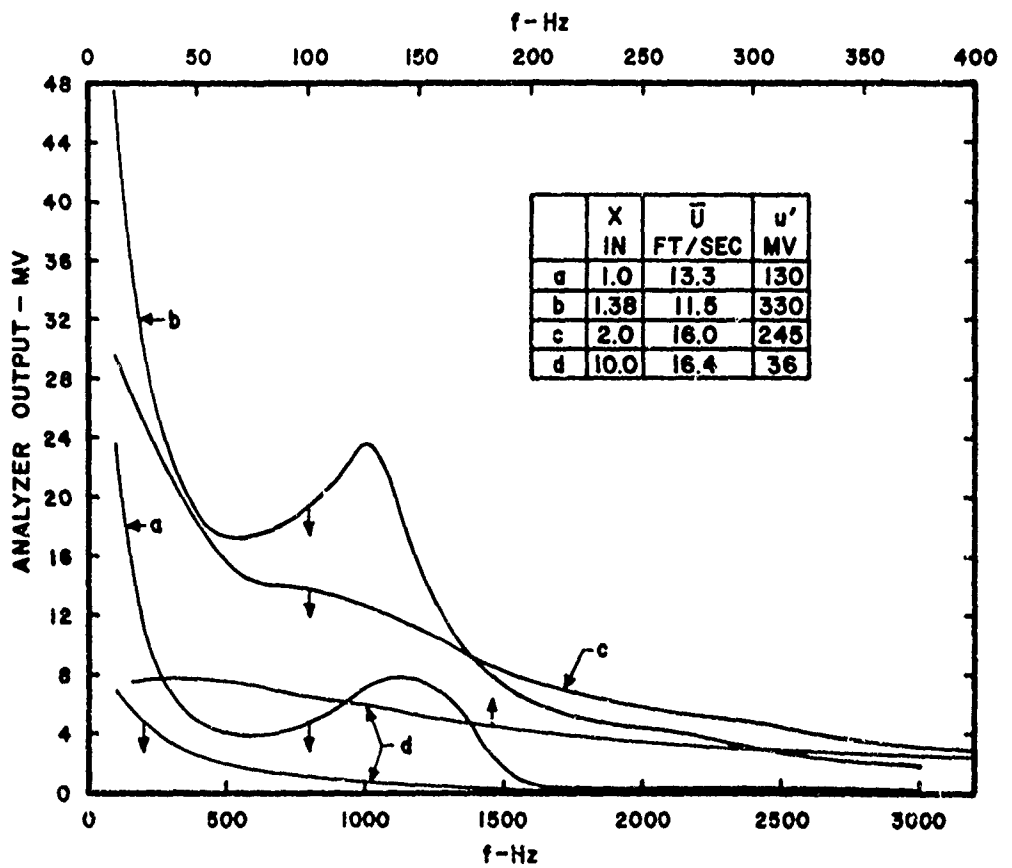

FIG. 27. SPECTRA OF u AT DIFFERENT AXIAL LOCATIONS FOR 3 IN. STRAWS IN TEST FLOW CONDITION "A".

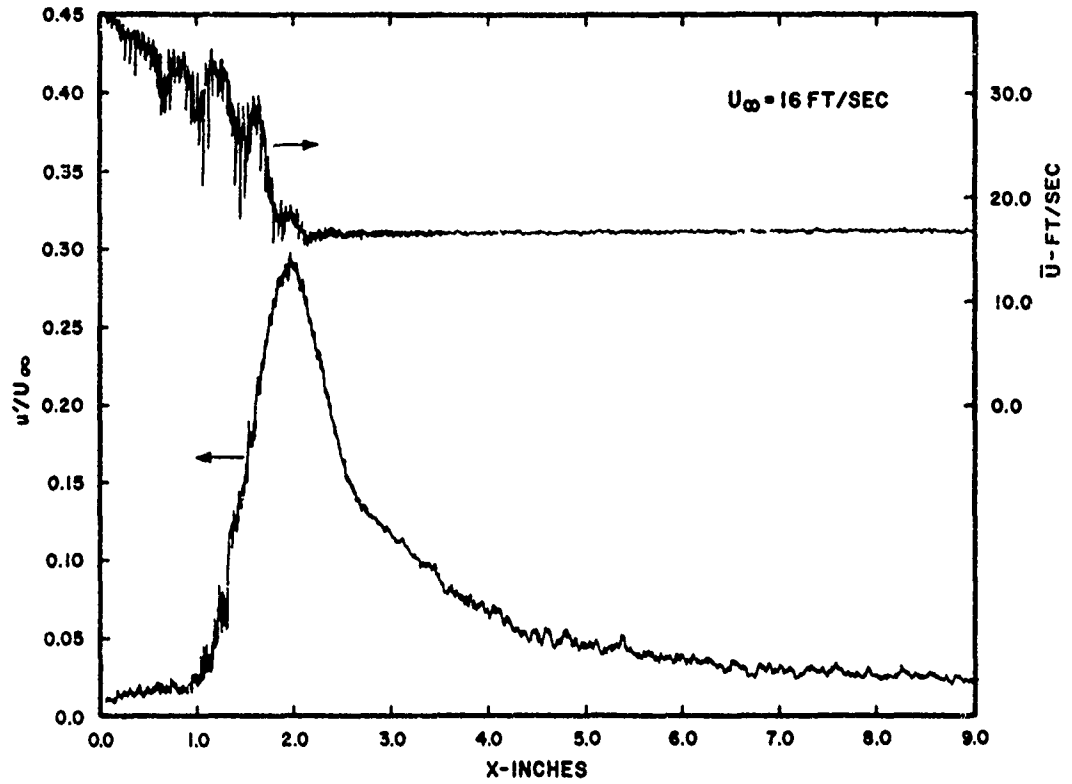

FIG. 28. AXIAL PROFILE OF u'/U_∞ AND $\bar{U}$ FOR 10 IN. STRAWS IN TEST FLOW CONDITION "A".

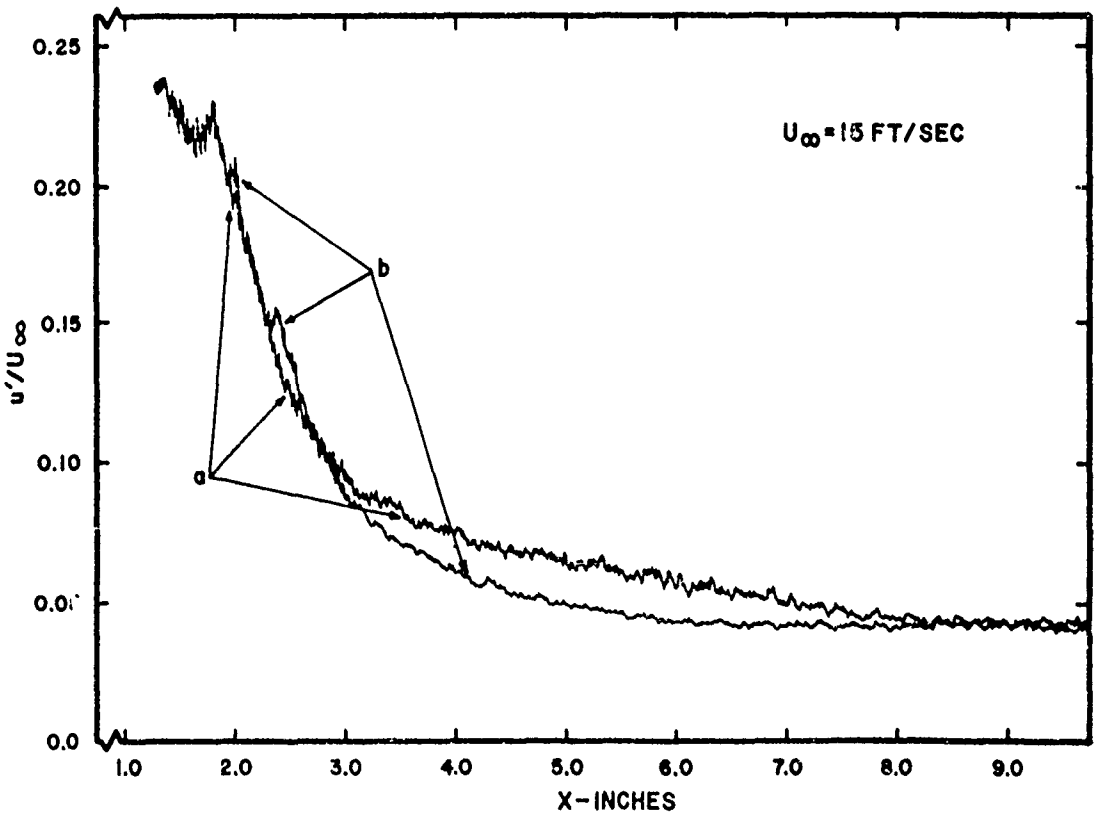

FIG. 29. AXIAL PROFILES OF u'/U_∞ AT TWO RADIAL LOCATIONS FOR 10 IN. STRAWS IN TEST FLOW CONDITION "A".

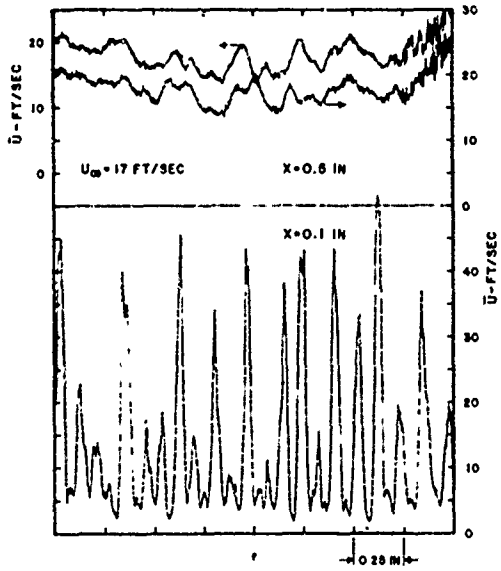

FIG. 30A. RADIAL PROFILES OF $\bar{U}$ AT DIFFERENT AXIAL LOCATIONS FOR P.P. # 1 IN TEST FLOW CONDITION "A".

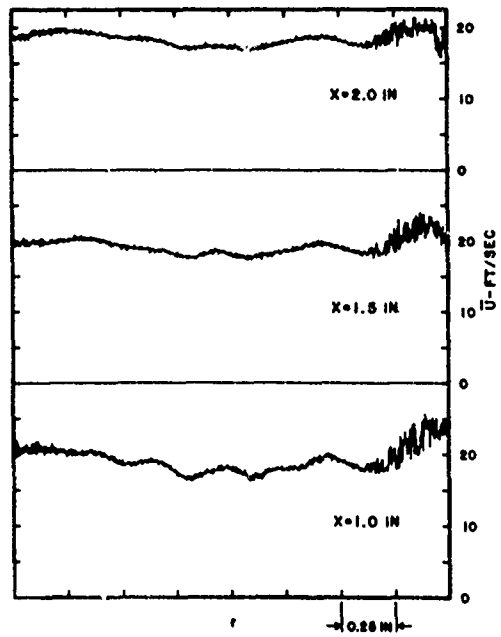

FIG. 30 B. RADIAL PROFILES OF $\bar{U}$ AT DIFFERENT AXIAL LOCATIONS FOR P.P. # 1 IN TEST FLOW CONDITION "A".

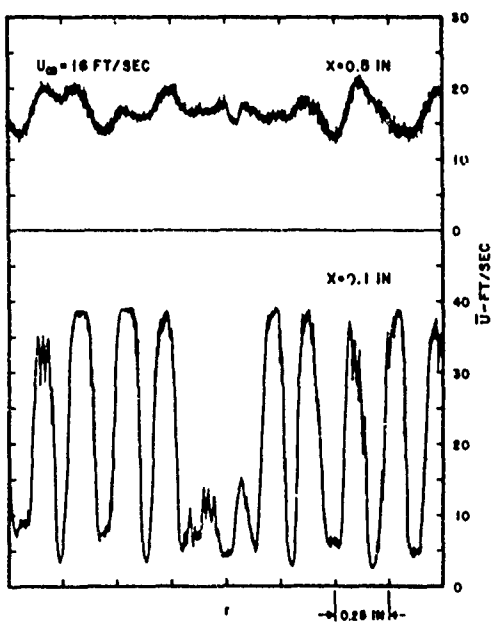

FIG. 31A. RADIAL PROFILES OF $\bar{U}$ AT DIFFERENT AXIAL LOCATIONS FOR P.P. # 2 IN TEST FLOW CONDITION "A".

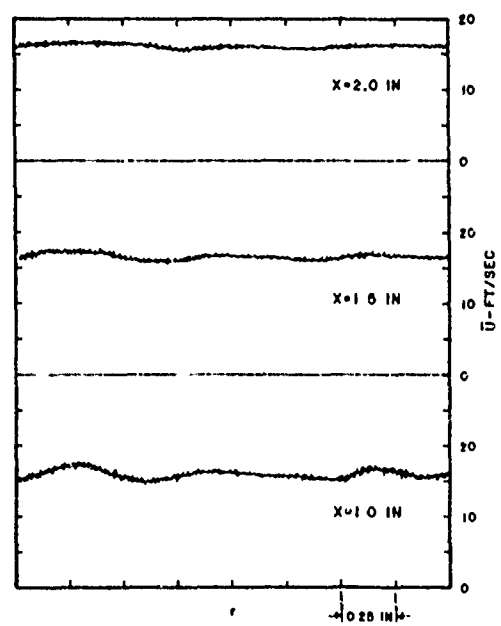

FIG. 31 B. RADIAL PROFILES OF $\bar{U}$ AT DIFFERENT AXIAL LOCATIONS FOR P.P. # 2 IN TEST FLOW CONDITION "A".

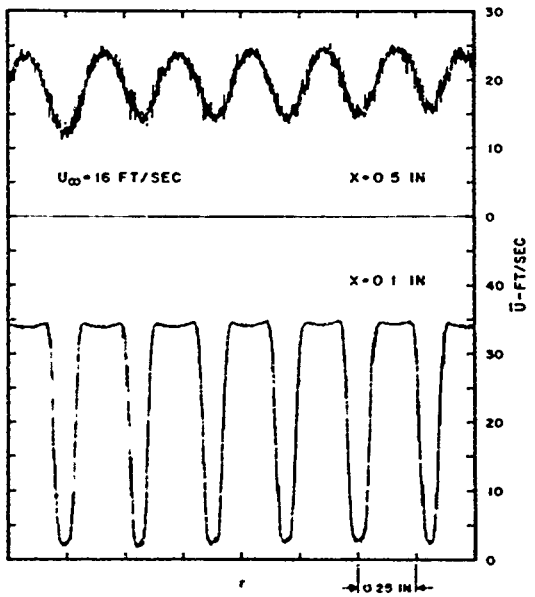

FIG. 32A. RADIAL PROFILES OF $\bar{U}$ AT DIFFERENT AXIAL LOCATIONS FOR P.P. #3 IN TEST FLOW CONDITION "A".

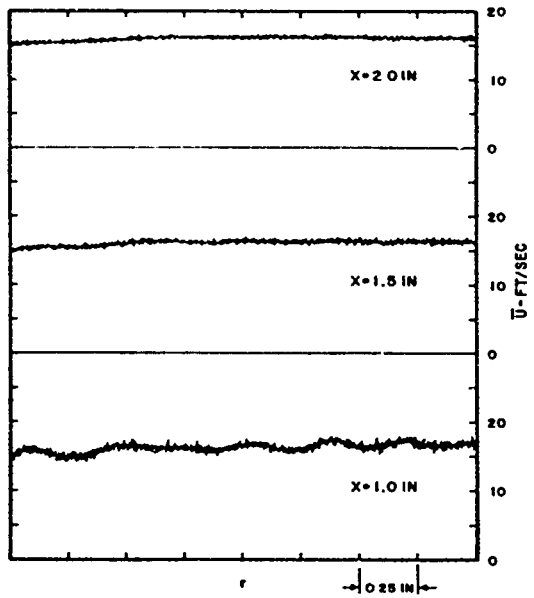

FIG. 32B. RADIAL PROFILES OF $\bar{U}$ AT DIFFERENT AXIAL LOCATIONS FOR P.P. #3 IN TEST FLOW CONDITION "A".

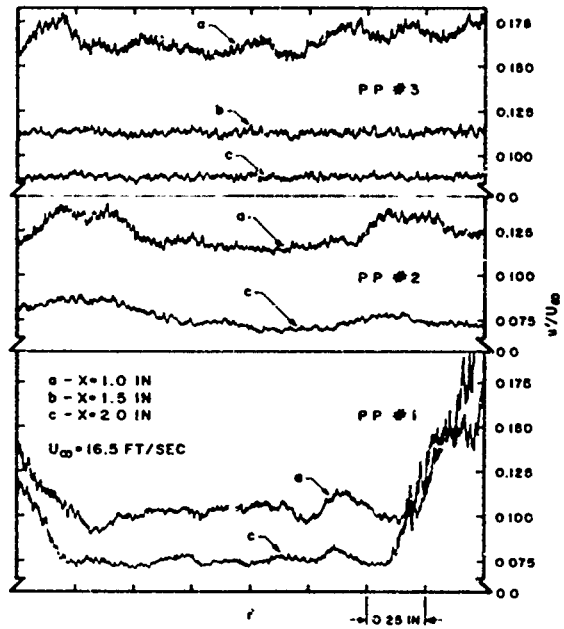

FIG. 33. RADIAL PROFILES OF u'/U_∞ AT DIFFERENT AXIAL LOCATIONS FOR P.P. #1, P.P. #2 AND P.P. #3 IN TEST FLOW CONDITION "A".

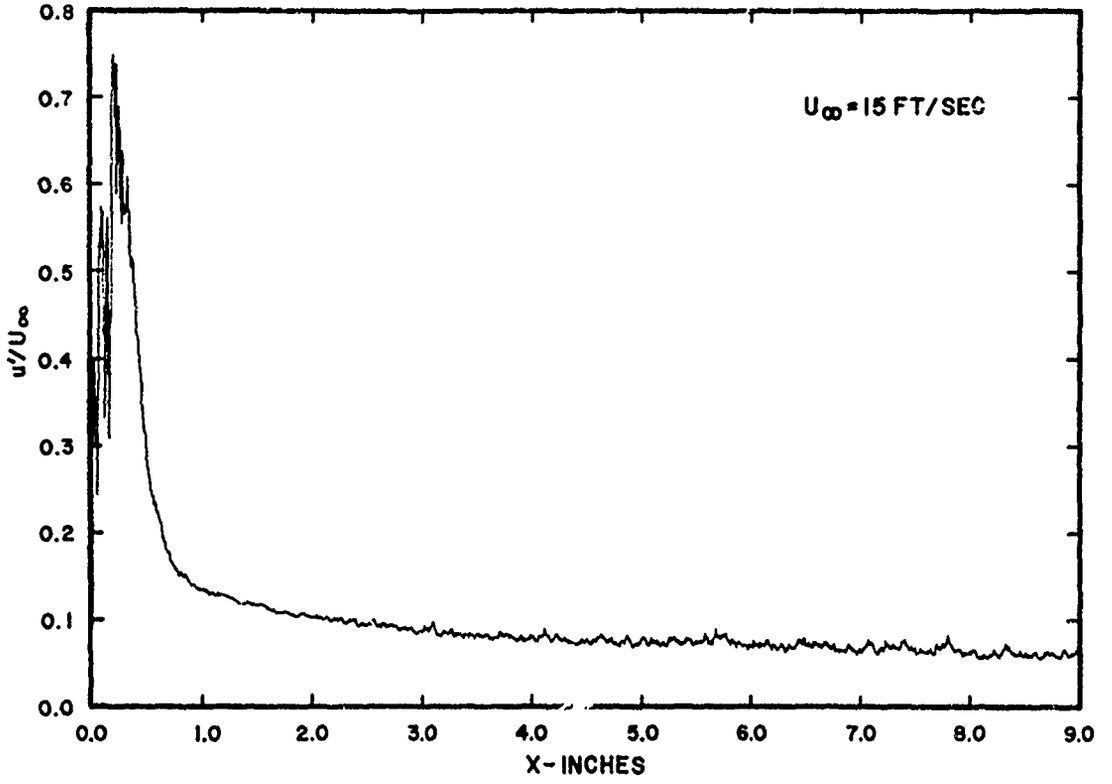

FIG. 34. AXIAL PROFILE OF u'/U_∞ FOR P.P. #1 IN TEST FLOW CONDITION "A".

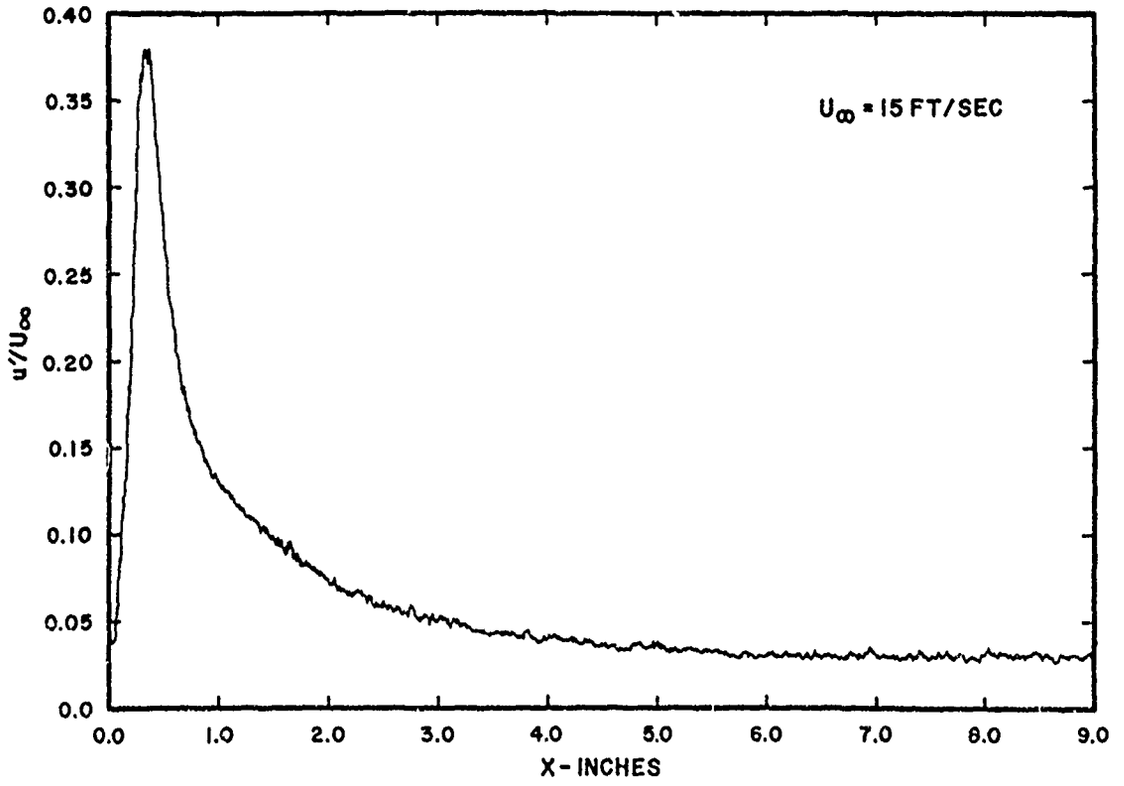

FIG. 35. AXIAL PROFILE OF u'/U_∞ FOR P.P. #2 IN TEST FLOW CONDITION "A".

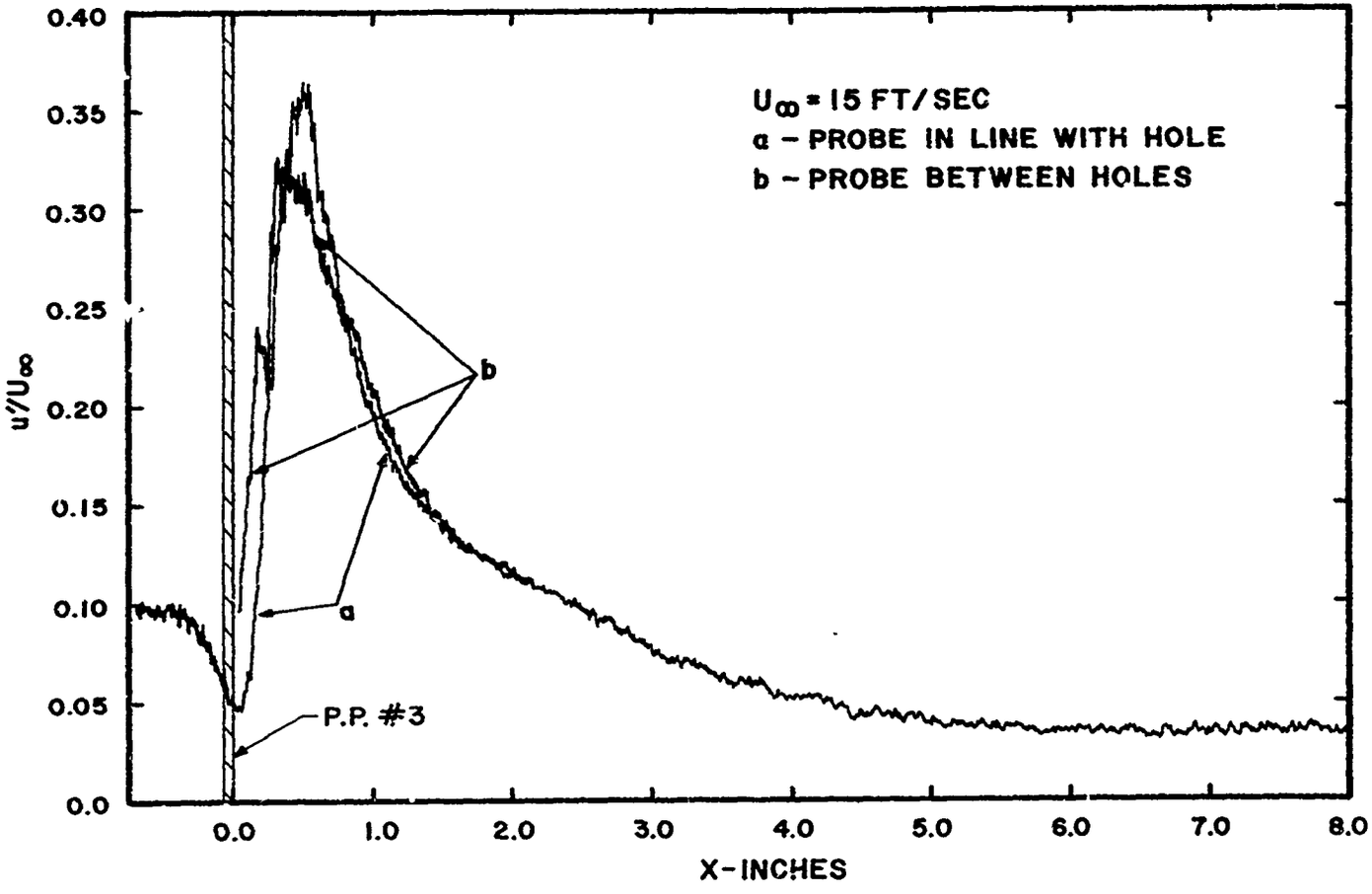

FIG. 36. AXIAL PROFILE OF u'/U_∞ FOR P.P. #3 IN TEST FLOW CONDITION "A".

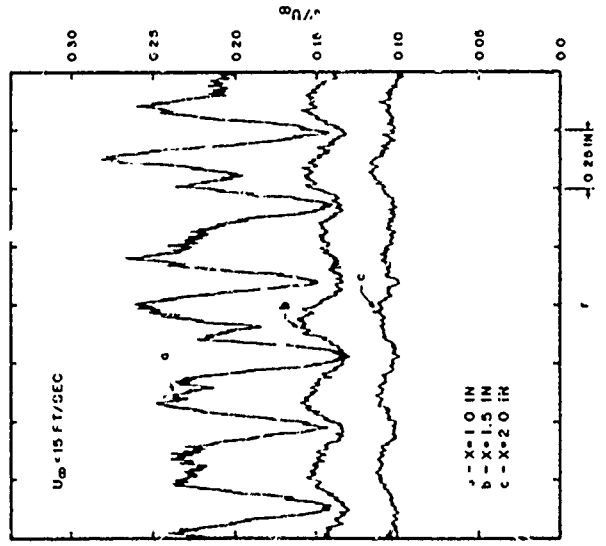

FIG. 38. RADIAL PROFILES OF u'/U_∞ AT DIFFERENT AXIAL LOCATIONS FOR P.P. #3 IN TEST FLOW CONDITION "B".

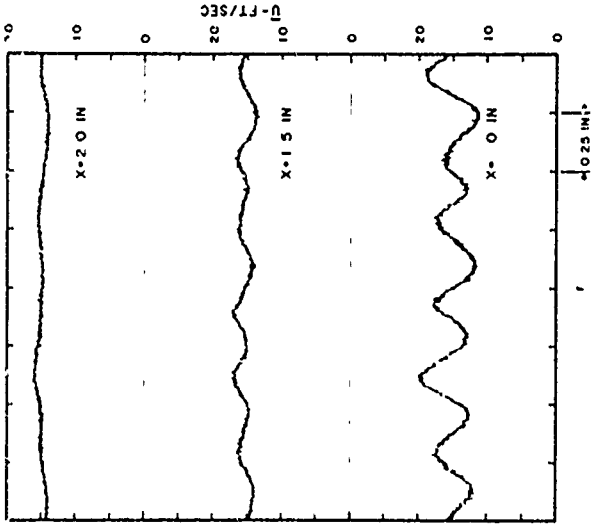

FIG. 37B. RADIAL PROFILES OF $\bar{U}$ AT DIFFERENT AXIAL LOCATIONS FOR P.P. #3 IN TEST FLOW CONDITION "B".

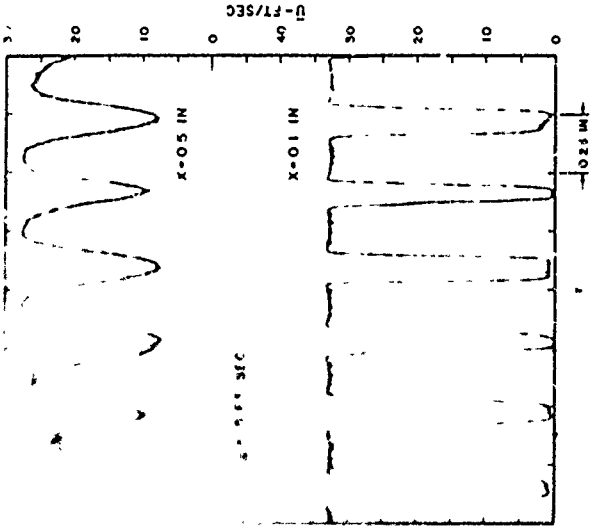

FIG. 37A RADIAL PROFILES OF $\bar{U}$ AT DIFFERENT AXIAL LOCATIONS FOR P.P. #3 IN TEST FLOW CONDITION "A".

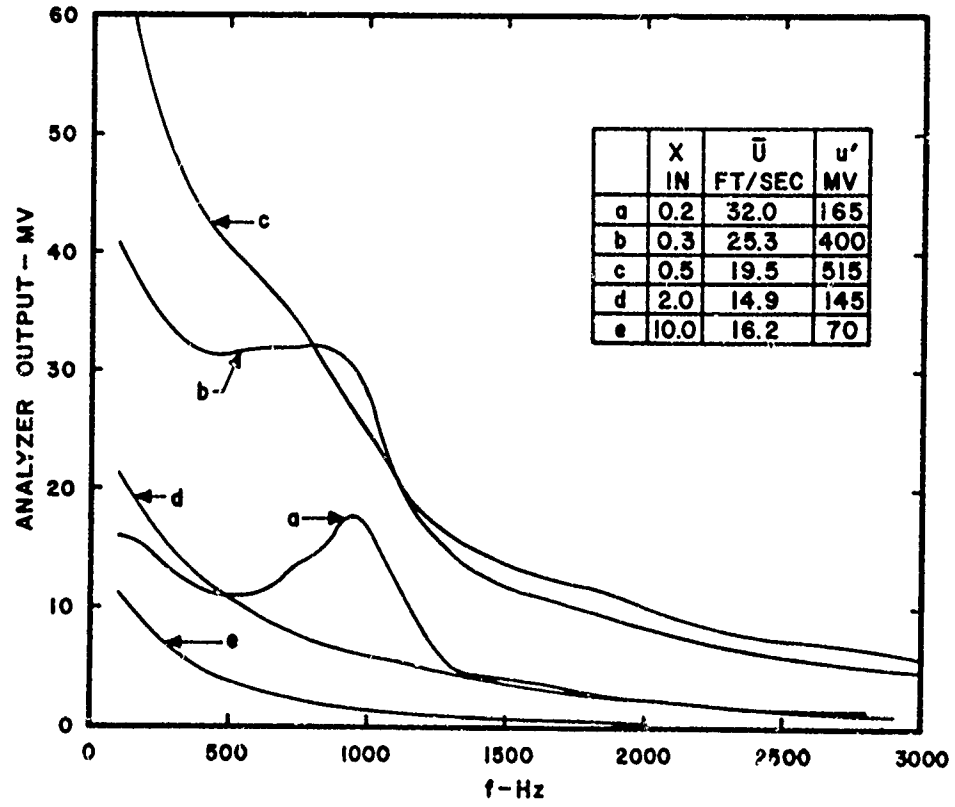

	X IN	$\bar{U}$ FT/SEC	u' MV
a	0.2	32.0	165
b	0.3	25.3	400
c	0.5	19.5	515
d	2.0	14.9	145
e	10.0	16.2	70

FIG. 39. SPECTRA OF u AT DIFFERENT AXIAL LOCATIONS FOR P.P. #3 IN TEST FLOW CONDITION "A".

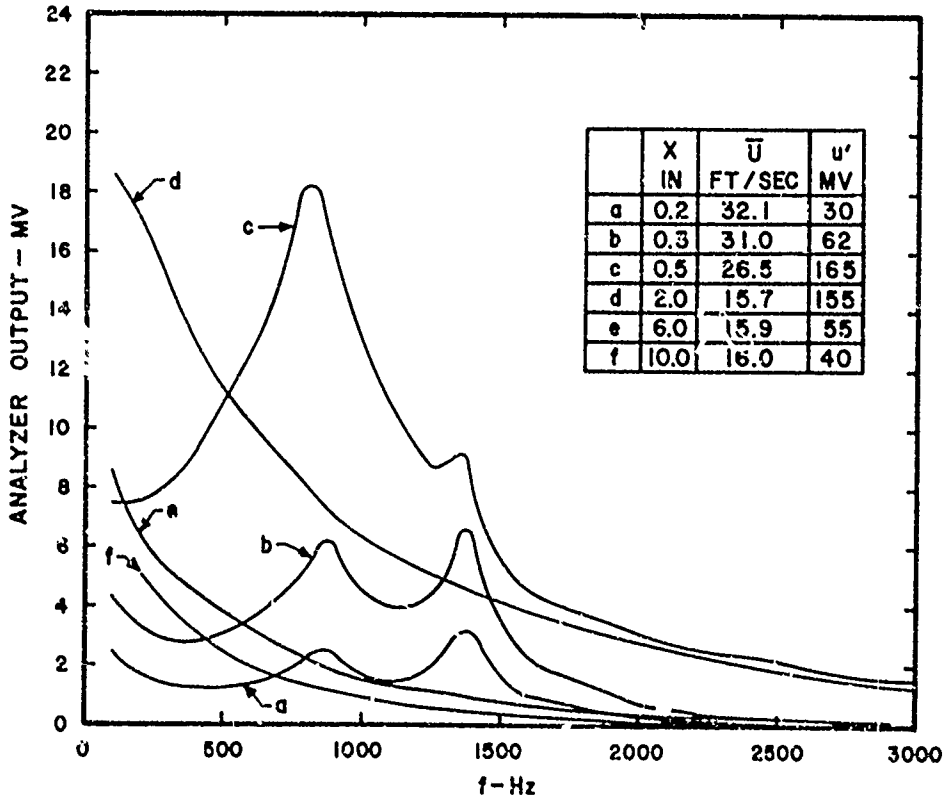

	X IN	$\bar{U}$ FT/SEC	u' MV
a	0.2	32.1	30
b	0.3	31.0	62
c	0.5	26.5	165
d	2.0	15.7	155
e	6.0	15.9	55
f	10.0	16.0	40

FIG. 40. SPECTRA OF u AT DIFFERENT AXIAL LOCATIONS FOR P.P. #3 IN TEST FLOW CONDITION "B".

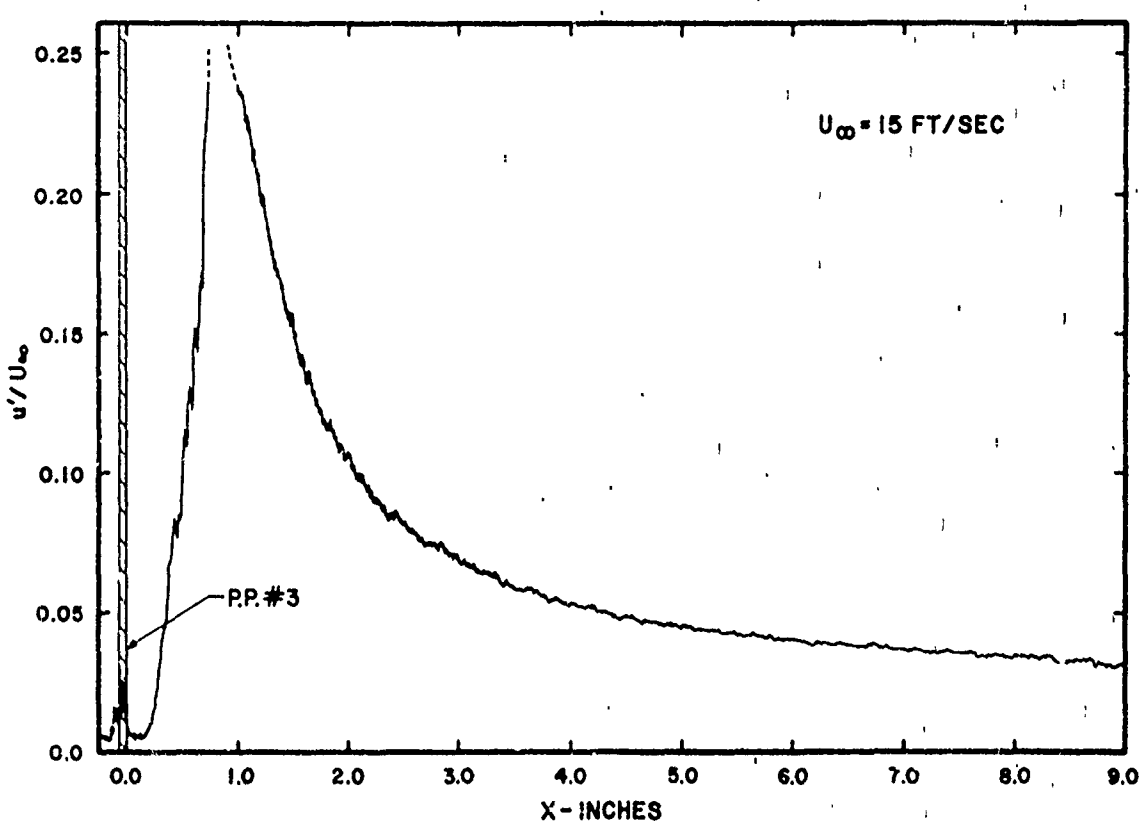

FIG. 41. AXIAL PROFILE OF u'/U_∞ FOR P.P. #3 IN TEST FLOW CONDITION "B".

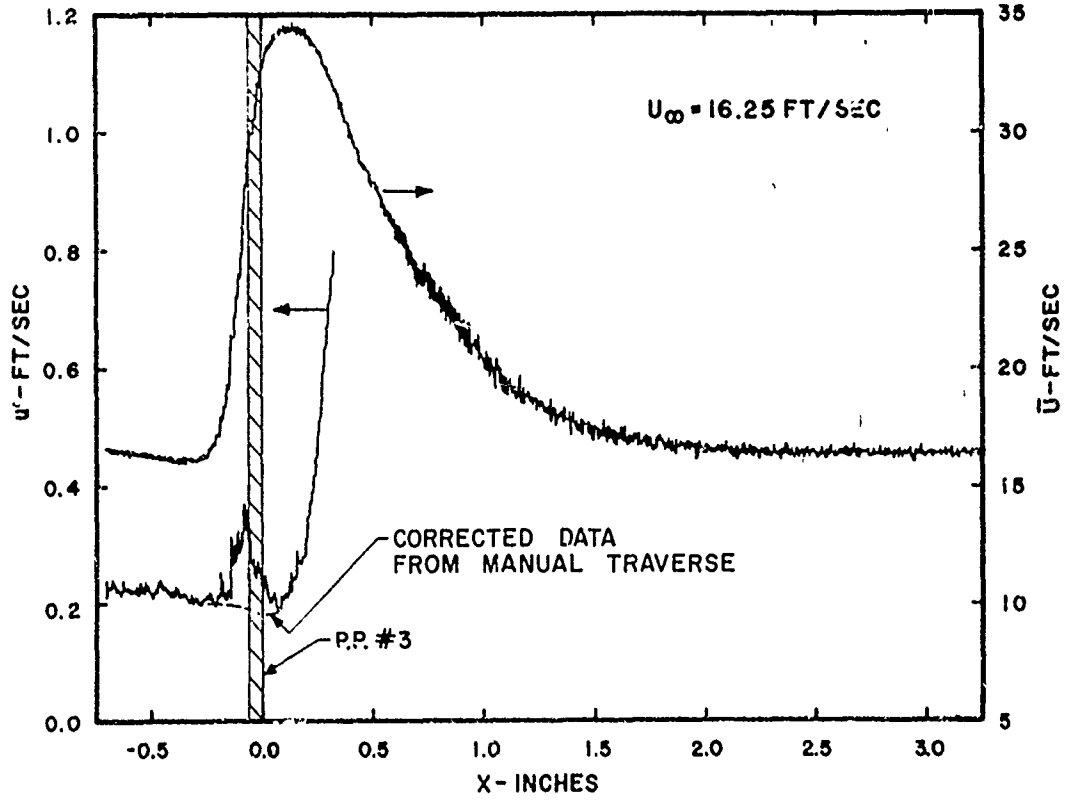

FIG. 42. AXIAL PROFILE OF u'/U_∞ AND $\bar{U}$ FOR P.P. #3 IN TEST FLOW CONDITION "B", EXPANDED SCALE.

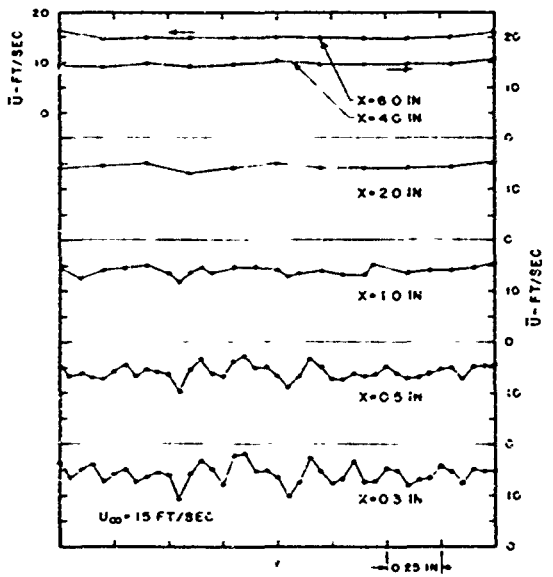

FIG 43. RADIAL PROFILES OF $\bar{U}$ AT DIFFERENT AXIAL LOCATIONS FOR POROUS FOAM IN TEST CONDITION "A".

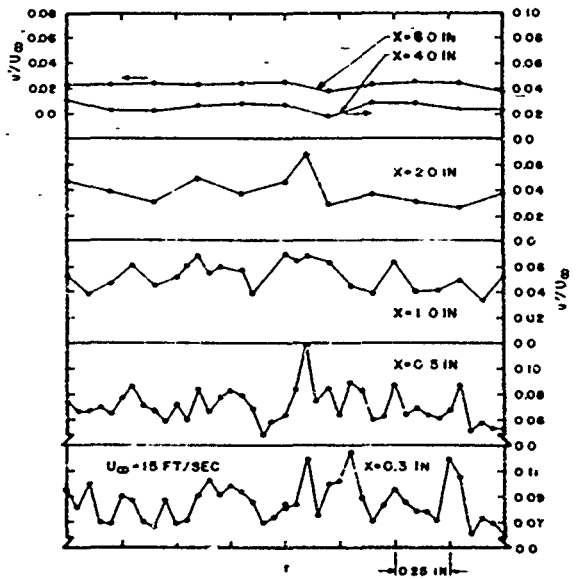

FIG. 44. RADIAL PROFILES OF u'/U_∞ AT DIFFERENT AXIAL LOCATIONS FOR POROUS FOAM IN TEST FLOW CONDITION "A".

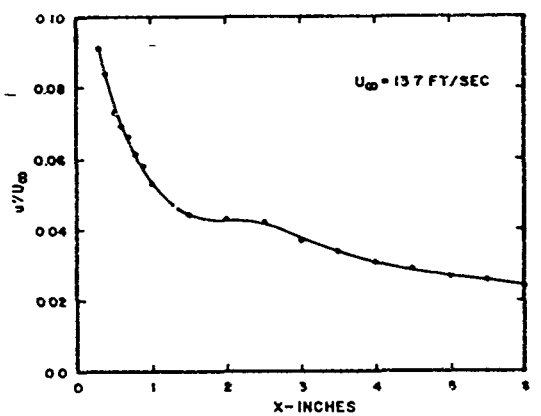

FIG. 45. AXIAL PROFILE OF u'/U_∞ FOR POROUS FOAM IN TEST FLOW CONDITION "A".

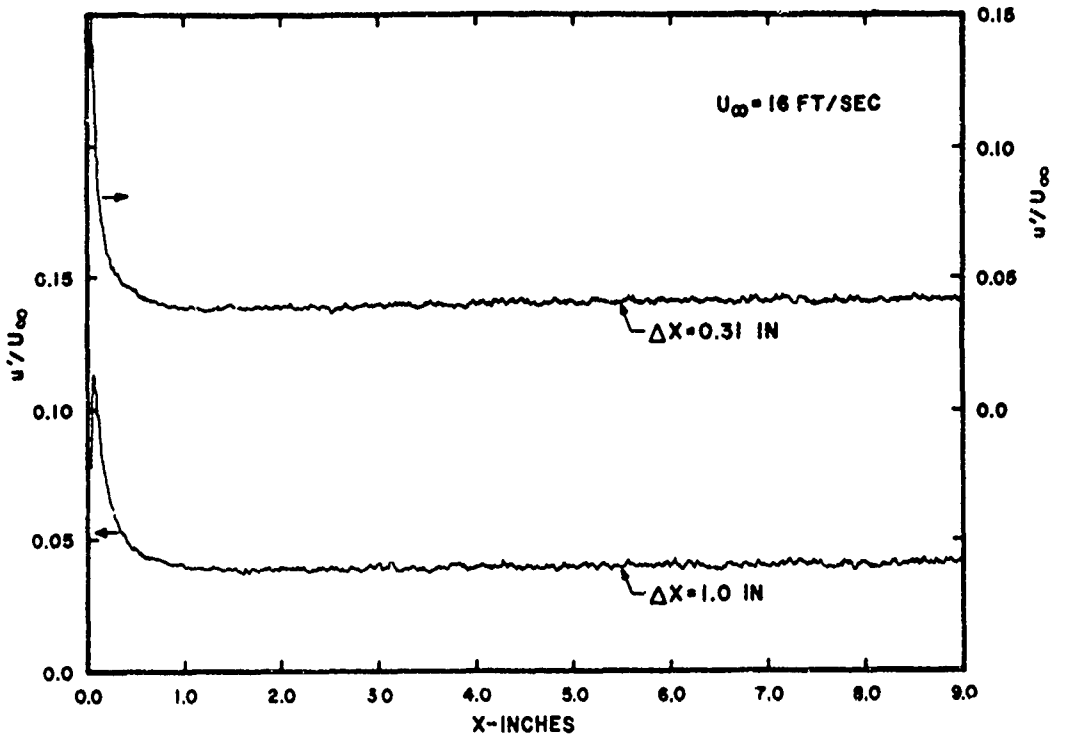

FIG. 46. AXIAL PROFILES OF u'/U_∞ FOR TWO SCREENS WITH X=0.31 AND 1.0 IN. IN TEST FLOW CONDITION "A".

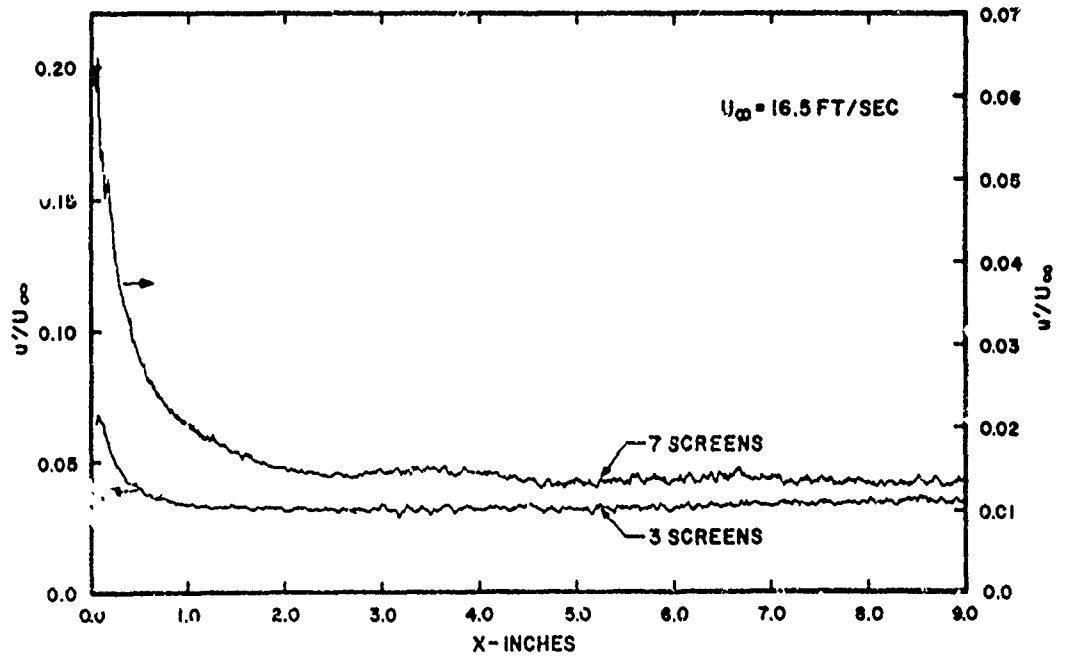

FIG. 47. AXIAL PROFILE OF u'/U_∞ FOR 3 AND 7 SCREENS IN SERIES IN TEST FLOW CONDITION "A".

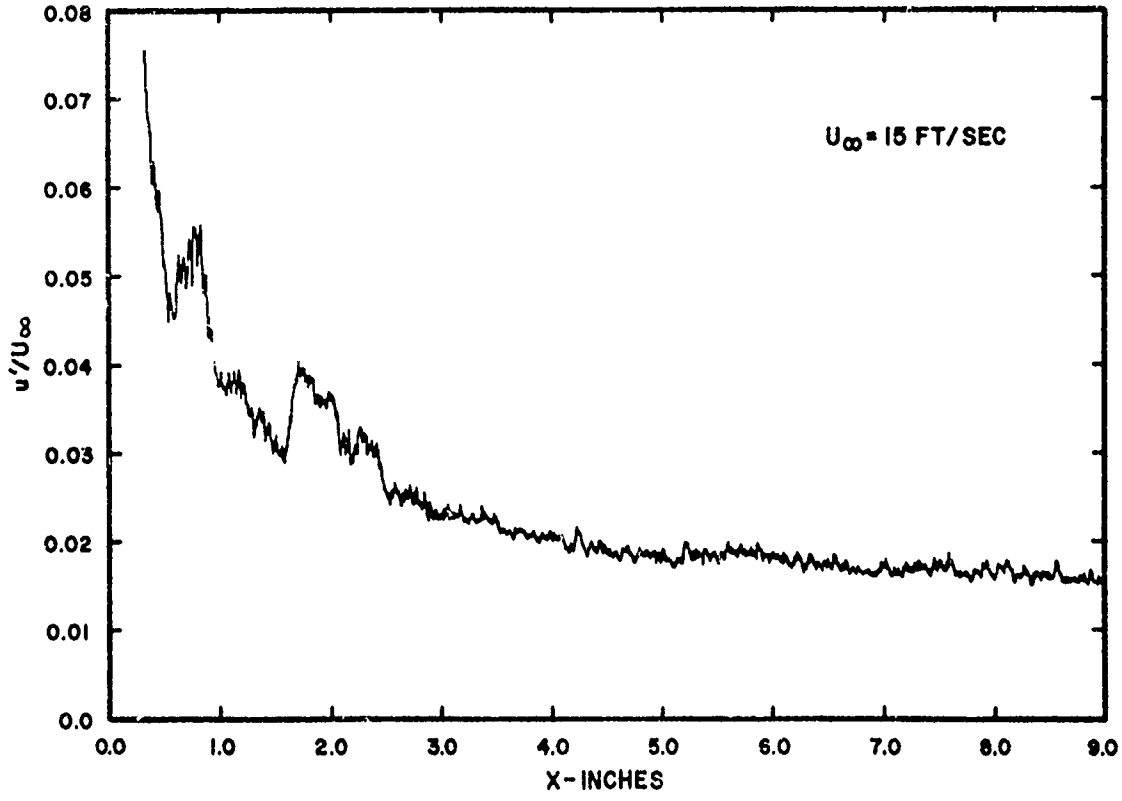

FIG. 48. AXIAL PROFILE OF u'/U_{∞} FOR 1 IN. STRAWS PLUS SCREEN IN TEST FLOW CONDITION "A".

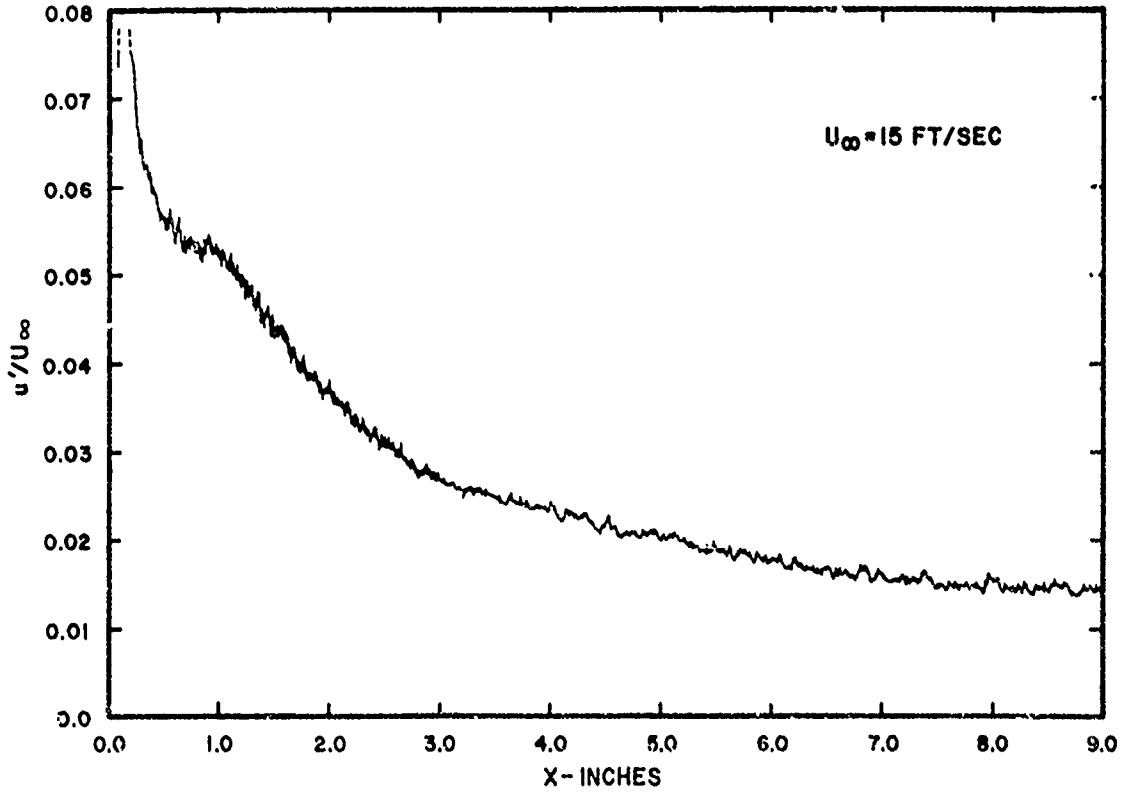

FIG. 49. AXIAL PROFILE OF u'/U_{∞} FOR 3 IN. STRAWS PLUS SCREEN IN TEST CONDITION "A".

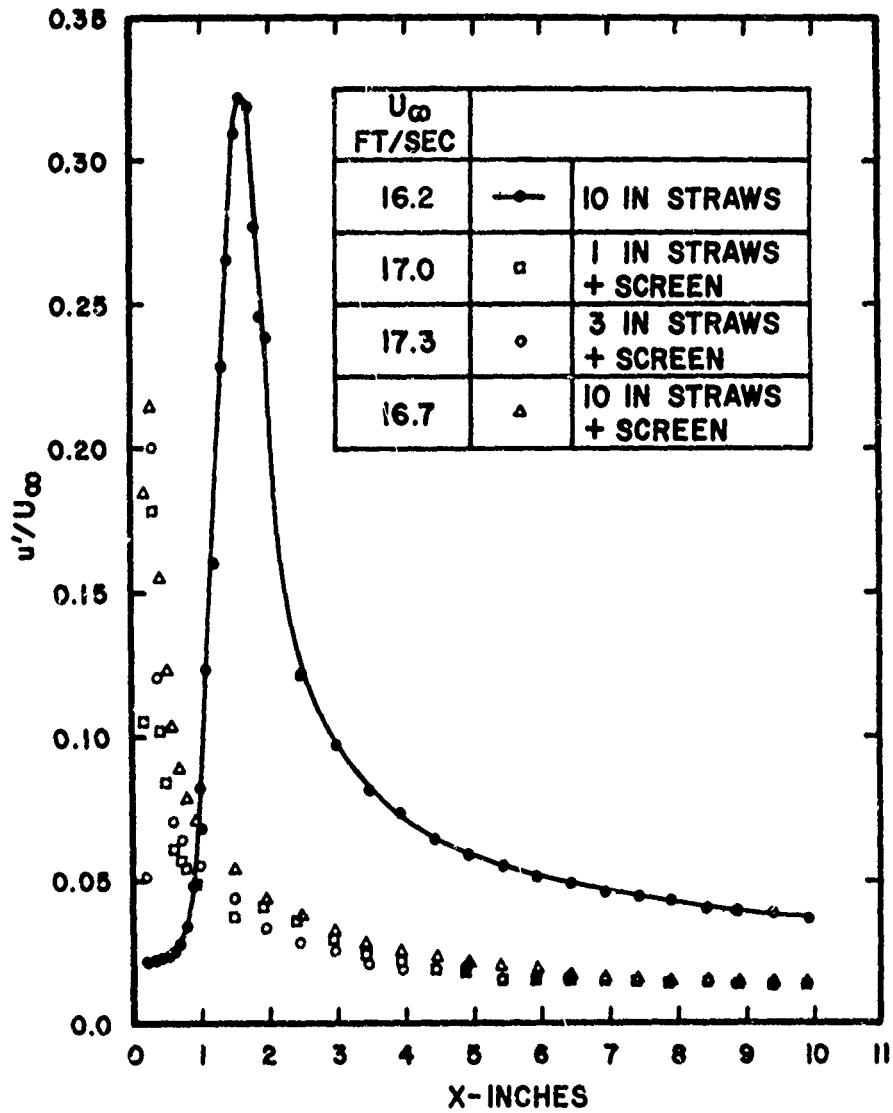

FIG. 50. AXIAL PROFILES OF u'/U_∞ FOR 1 IN., 3 IN. AND 10 IN. STRAWS PLUS SCREEN IN TEST FLOW CONDITION "A".

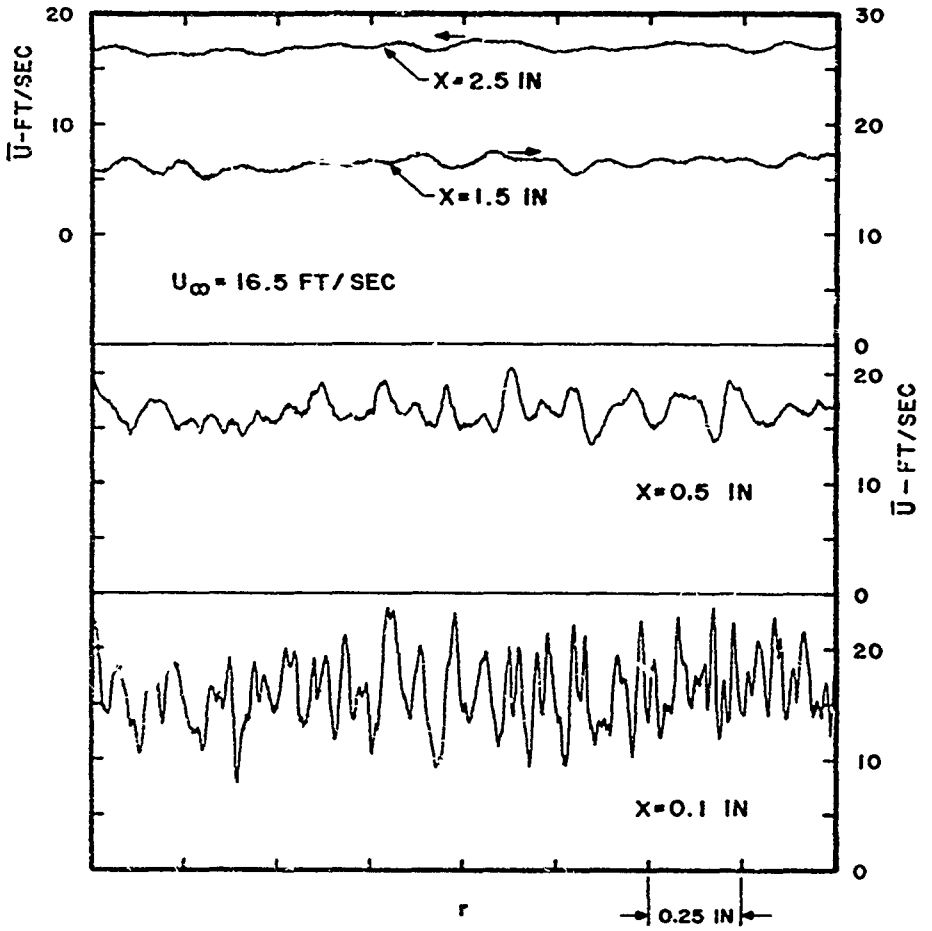

FIG. 51. RADIAL PROFILES OF $\bar{U}$ FOR 3 IN. STRAWS PLUS SCREEN IN TEST FLOW CONDITION "A".

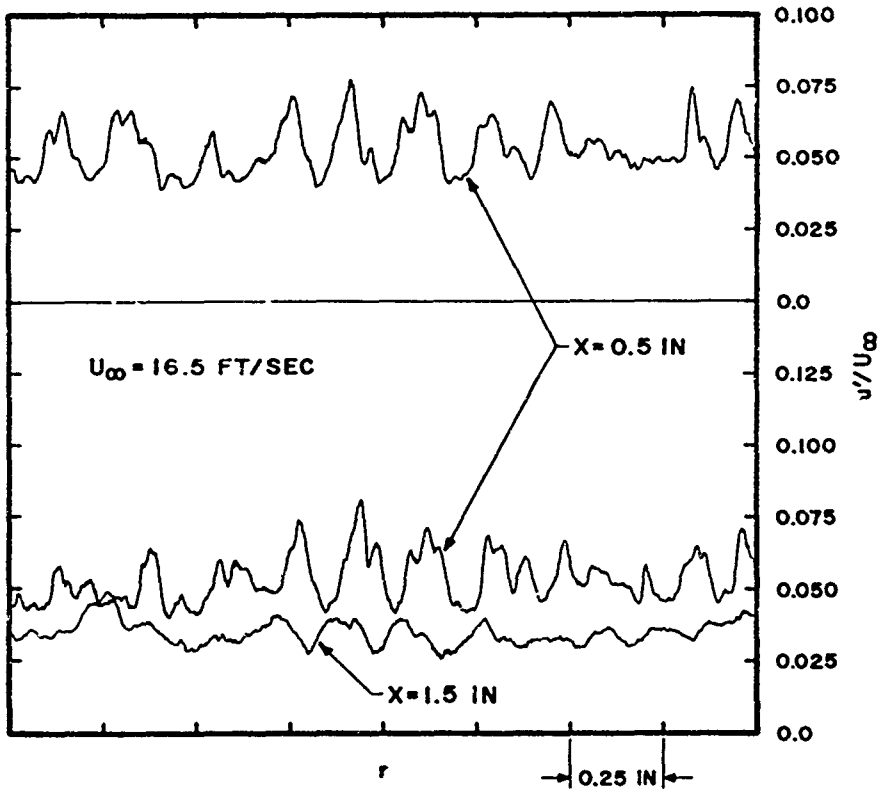

FIG. 52. RADIAL PROFILES OF u'/U_∞ FOR 3 IN. STRAWS PLUS SCREEN IN TEST FLOW CONDITION "A".

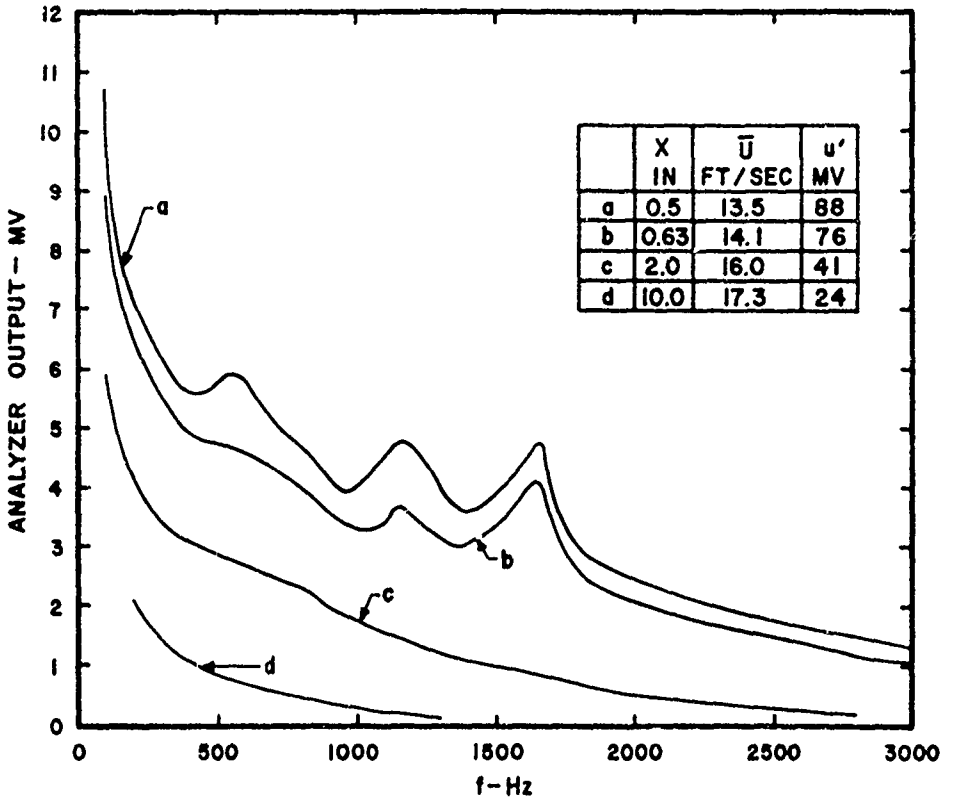

FIG. 53. SPECTRA OF u AT DIFFERENT AXIAL LOCATIONS FOR 1 IN. STRAWS PLUS SCREEN IN TEST FLOW CONDITION "A".

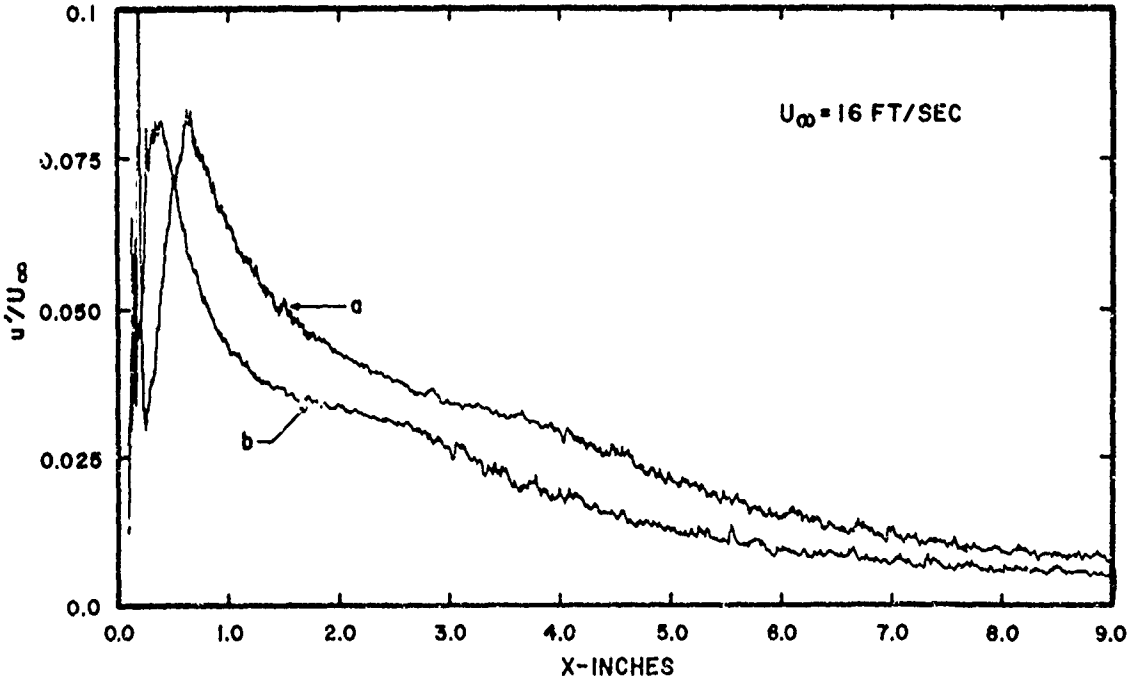

FIG. 54. AXIAL PROFILES OF u'/U_∞ FOR 10 IN. STRAWS PLUS SCREEN AT TWO RADIAL LOCATIONS IN TEST FLOW CONDITION "A".

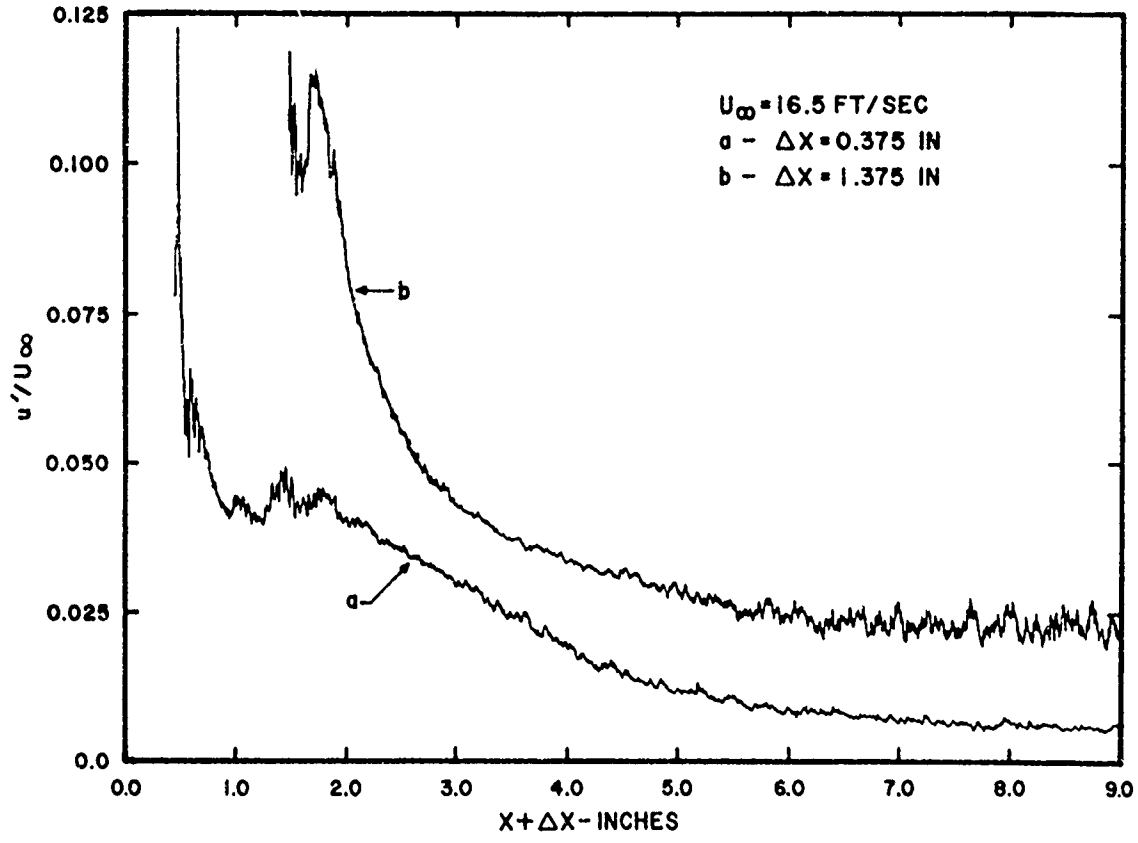

FIG. 55. AXIAL PROFILES OF u'/U_∞ FOR 10 IN. STRAWS PLUS SCREEN WITH $\Delta X = 0.375$ IN. AND 1.375 IN. IN TEST FLOW CONDITION "A".

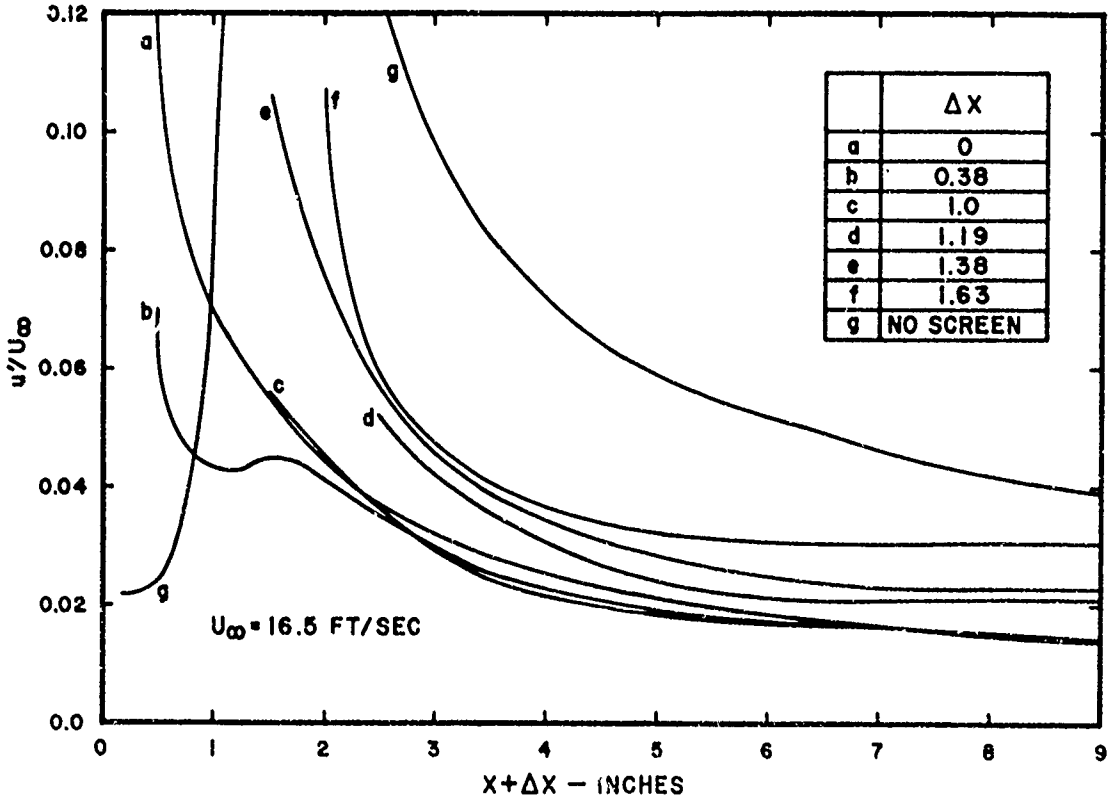

FIG. 56. AXIAL PROFILES OF u'/U_∞ FOR 10 IN. STRAWS PLUS SCREEN FOR SEVERAL SCREEN SEPARATION DISTANCES IN TEST FLOW CONDITION "A".

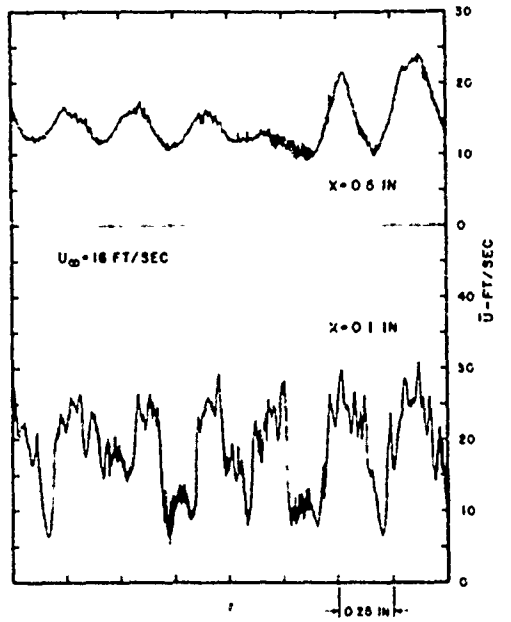

FIG. 57A. RADIAL PROFILES OF $\bar{U}$ FOR P.P. # 3 PLUS SCREEN AT DIFFERENT AXIAL LOCATIONS IN TEST FLOW CONDITION "A".

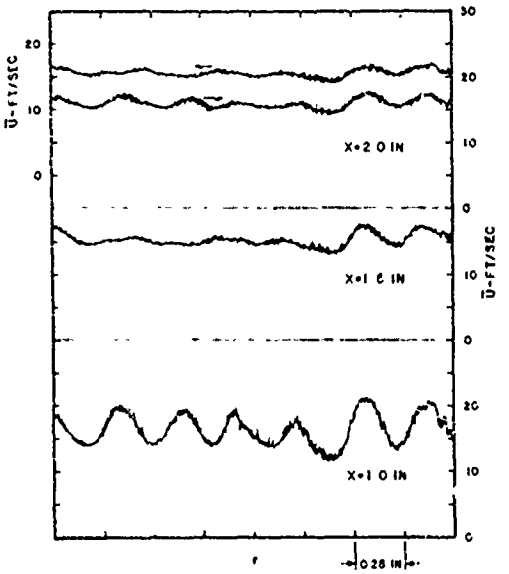

FIG. 57 B. RADIAL PROFILES OF $\bar{U}$ FOR P.P. # 3 PLUS SCREEN AT DIFFERENT AXIAL LOCATIONS IN TEST FLOW CONDITION "A".

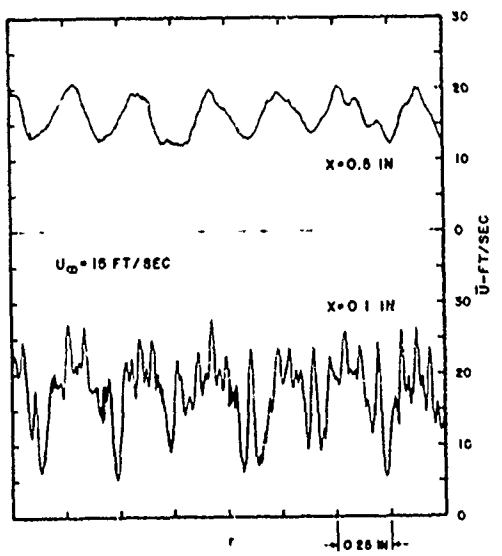

FIG. 58A. RADIAL PROFILES OF $\bar{U}$ FOR P.P. # 3 PLUS SCREEN AT DIFFERENT AXIAL LOCATIONS IN TEST FLOW CONDITION "B".

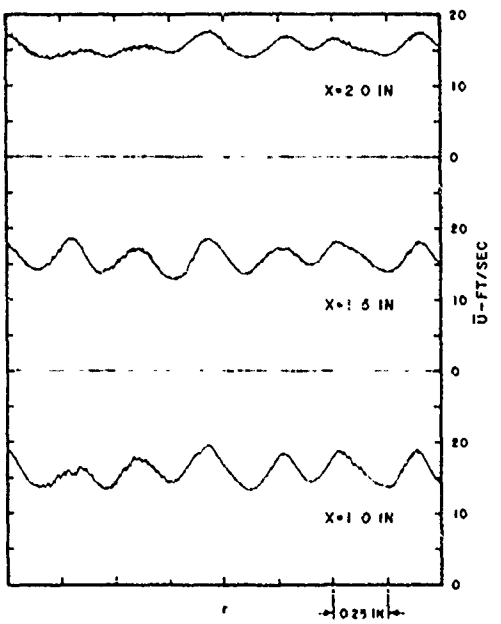

FIG. 58 B. RADIAL PROFILES OF $\bar{U}$ FOR P.P. # 3 PLUS SCREEN AT DIFFERENT AXIAL LOCATIONS IN TEST FLOW CONDITION " B "

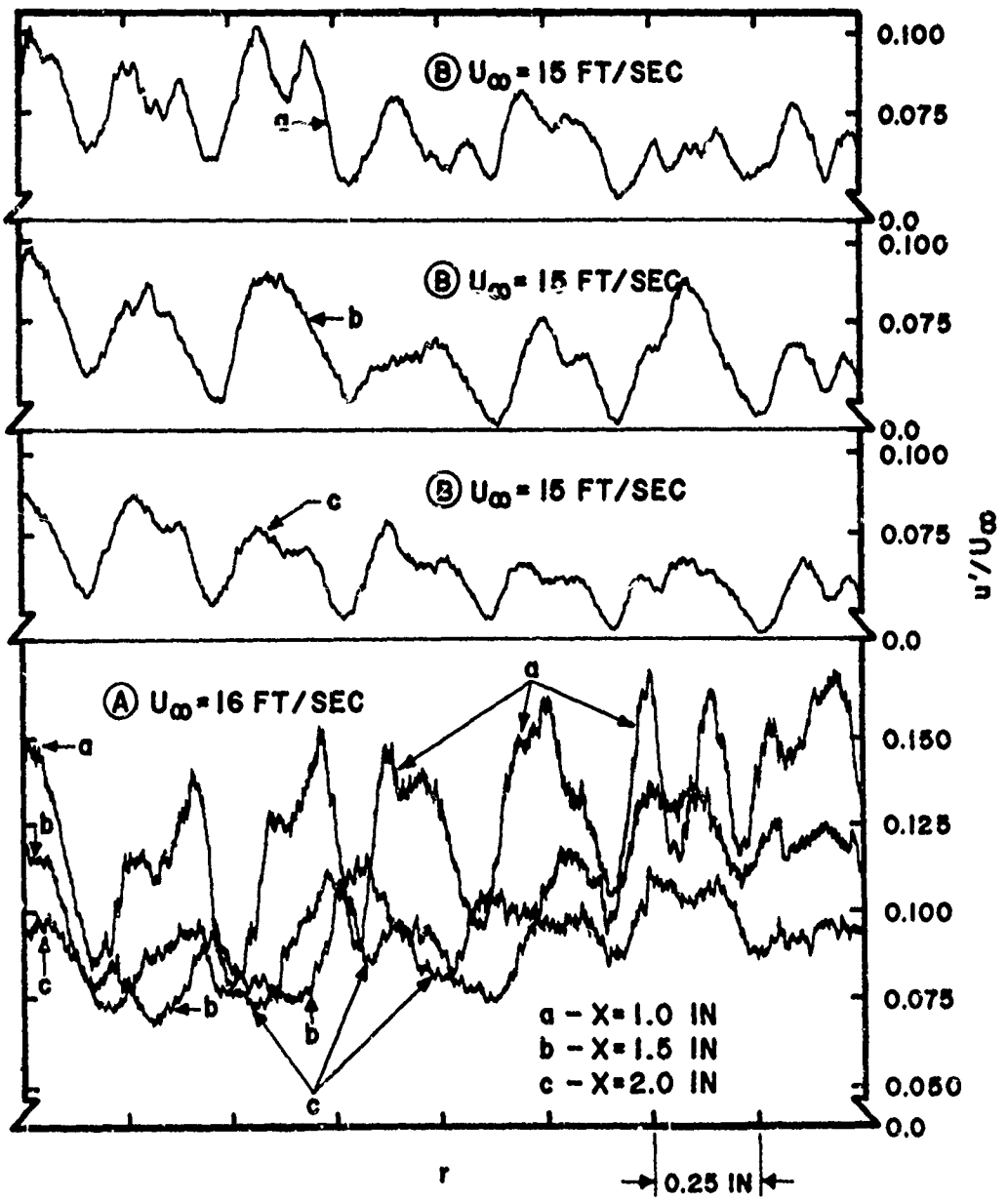

FIG. 59. RADIAL PROFILES OF u'/U FOR P.P. #3 PLUS SCREEN AT DIFFERENT AXIAL LOCATIONS IN TEST FLOW CONDITIONS "A" AND "B".

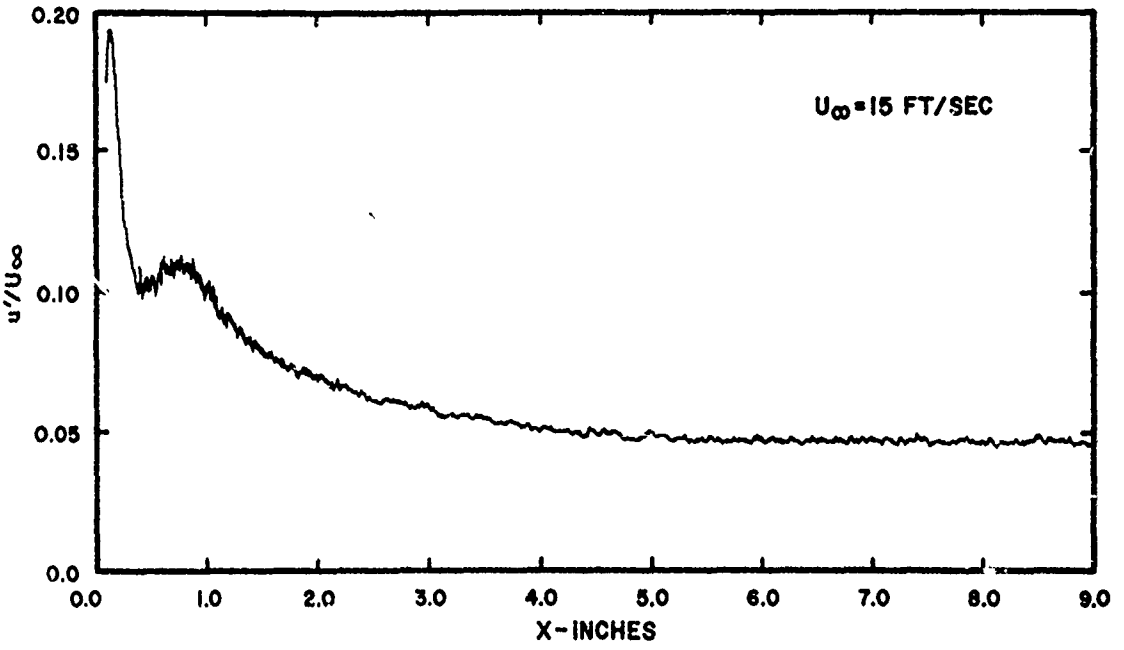

FIG. 60. AXIAL PROFILE OF u'/U_∞ FOR P.P. # 3 PLUS SCREEN IN TEST FLOW CONDITION "A".

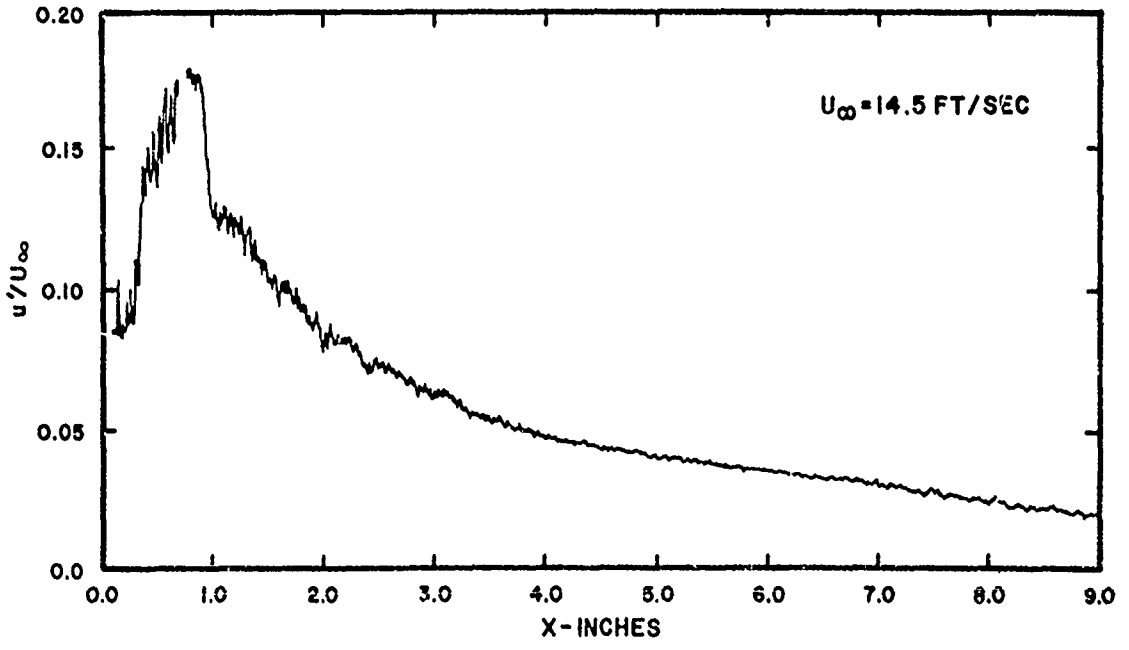

FIG. 61. AXIAL PROFILE OF u'/U_∞ FOR P.P. # 3 PLUS SCREEN IN TEST FLOW CONDITION "B".

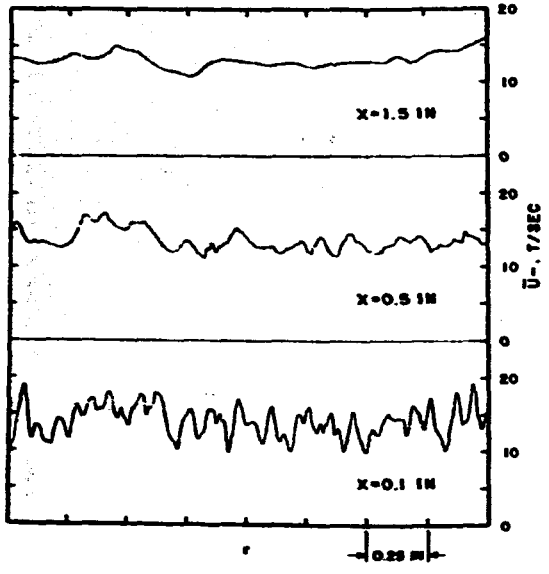

G. 62A. RADIAL PROFILES OF $\overline{U}$ FOR P.P. #2 PLUS FOAM AT DIFFERENT AXIAL LOCATIONS IN TEST FLOW CONDITION "A".

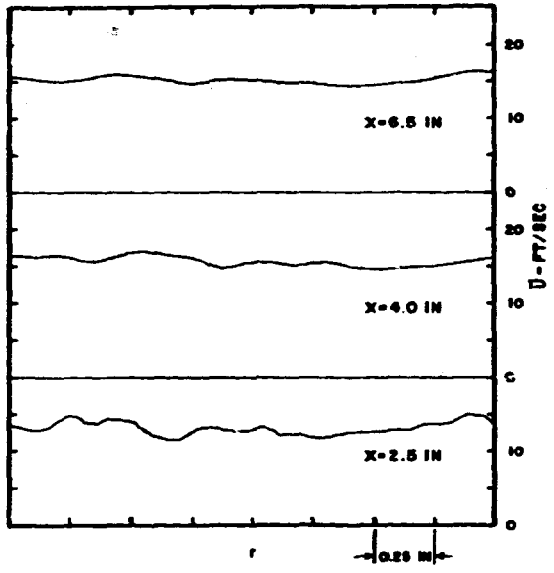

FIG. 62 B. RADIAL PROFILES OF $\overline{U}$ FOR P.P. #2 PLUS FOAM AT DIFFERENT AXIAL LOCATIONS IN TEST FLOW CONDITION "A".

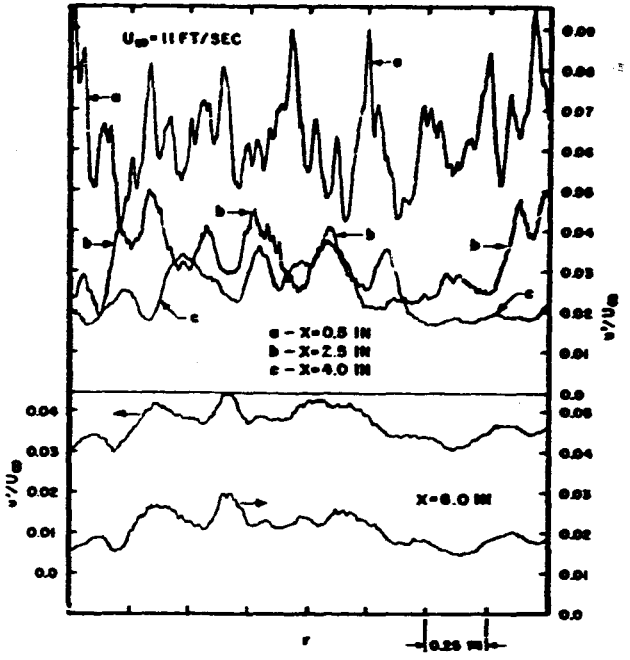

FIG. 63. RADIAL PROFILES OF u'/U_∞ FOR P.P. #2 PLUS FOAM AT DIFFERENT AXIAL LOCATIONS IN TEST FLOW CONDITION "A".

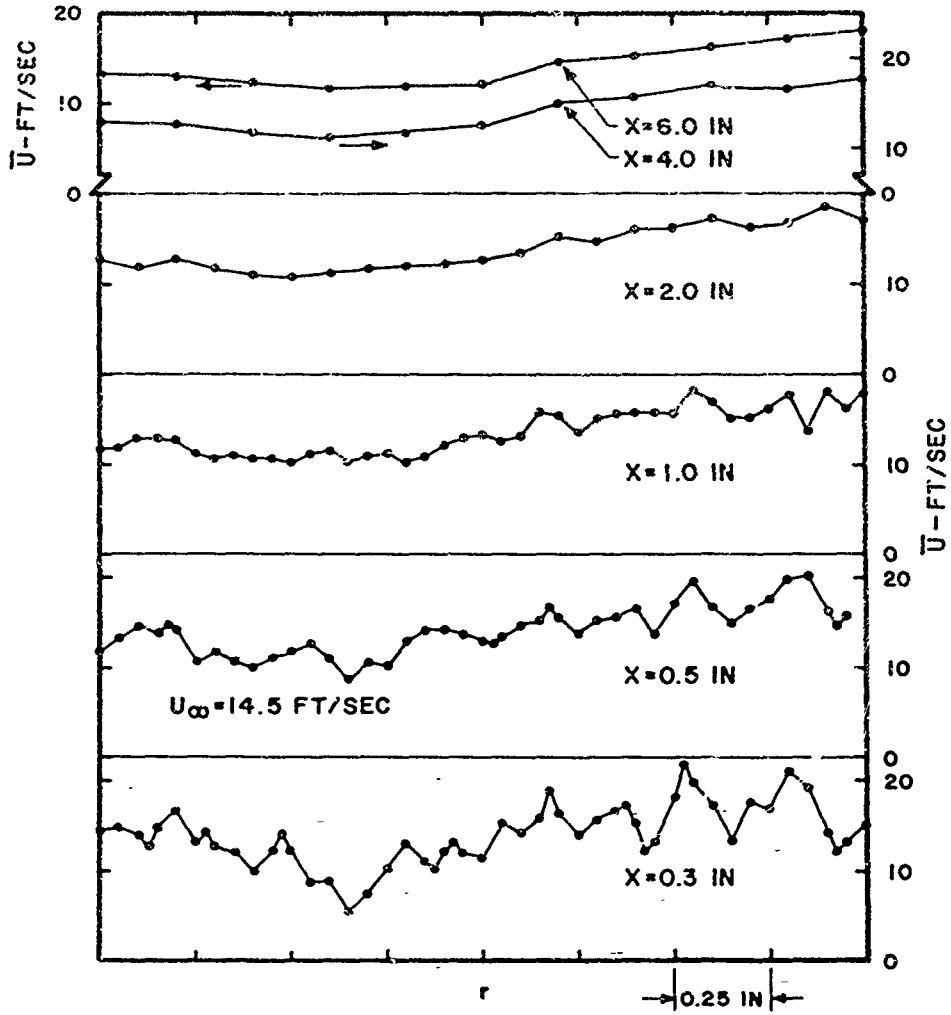

FIG. 64. RADIAL PROFILES OF $\bar{U}$ FOR P.P. # 1 PLUS FOAM AT DIFFERENT AXIAL LOCATIONS IN TEST FLOW CONDITION "A".

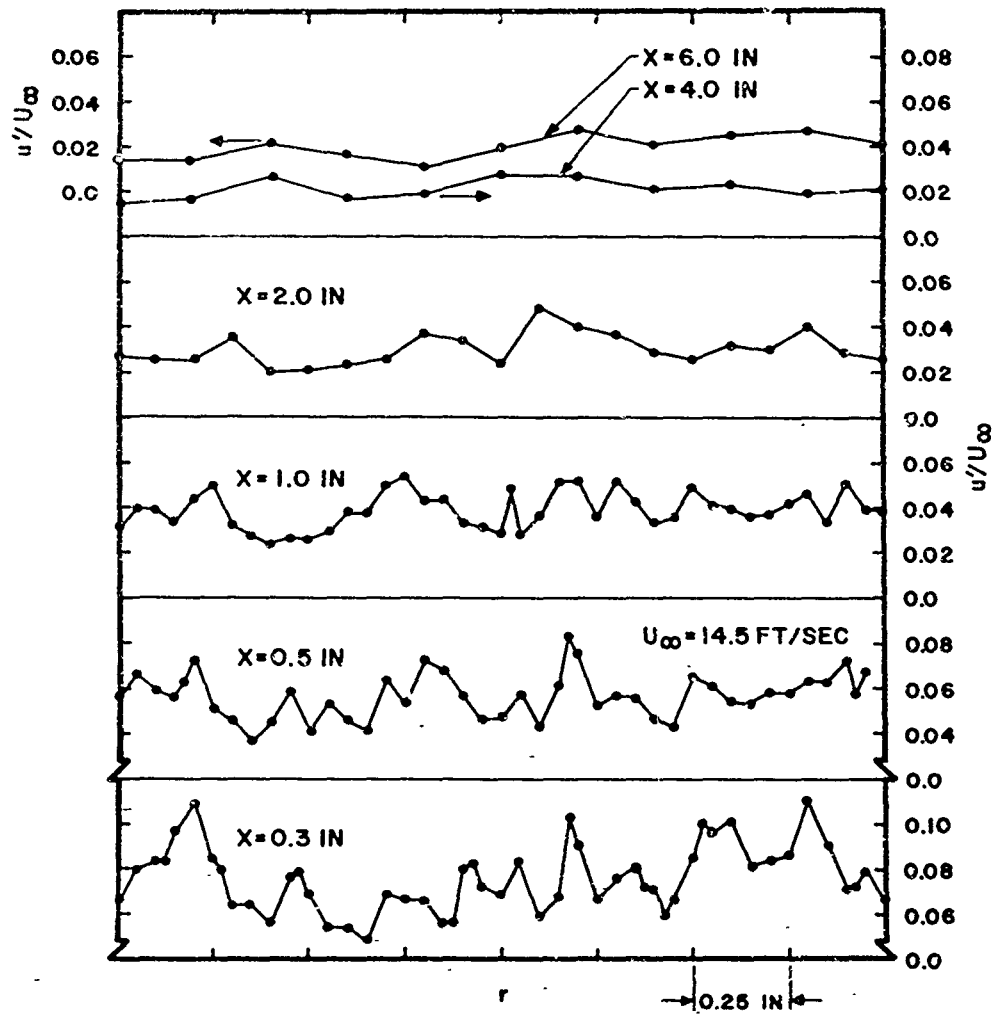

FIG. 65. RADIAL PROFILES OF u'/U_∞ FOR P.P. # 1 PLUS FOAM AT DIFFERENT AXIAL LOCATIONS IN TEST FLOW CONDITION "A".

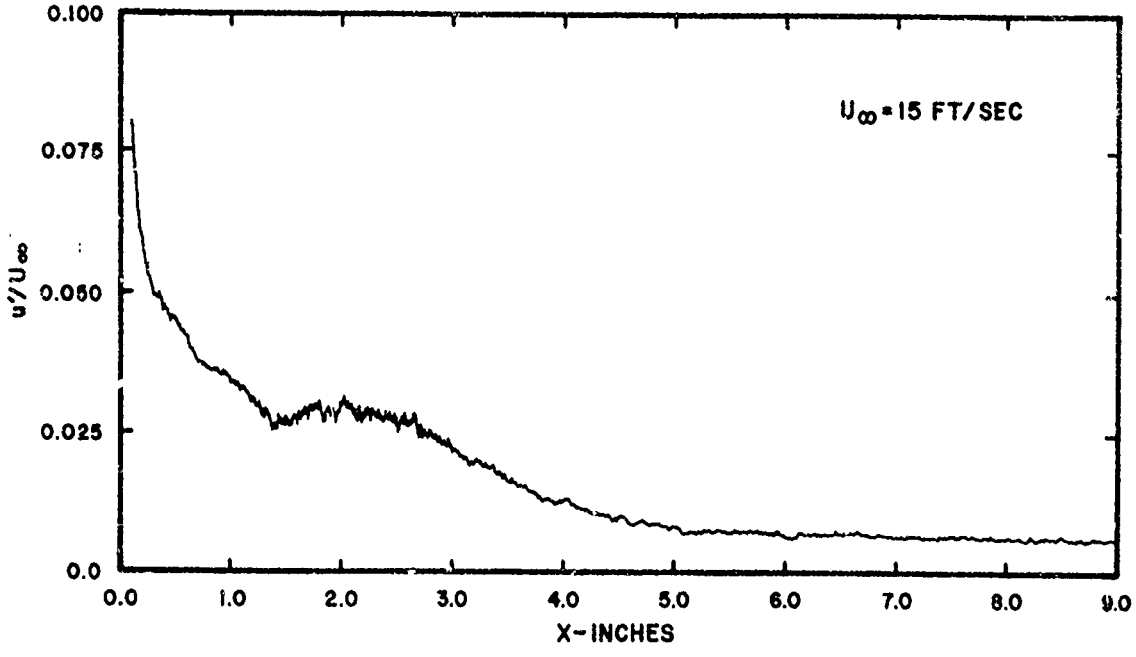

FIG. 66. AXIAL PROFILE OF u'/U_∞ FOR P.P. #2 PLUS FOAM IN TEST FLOW CONDITION "A".

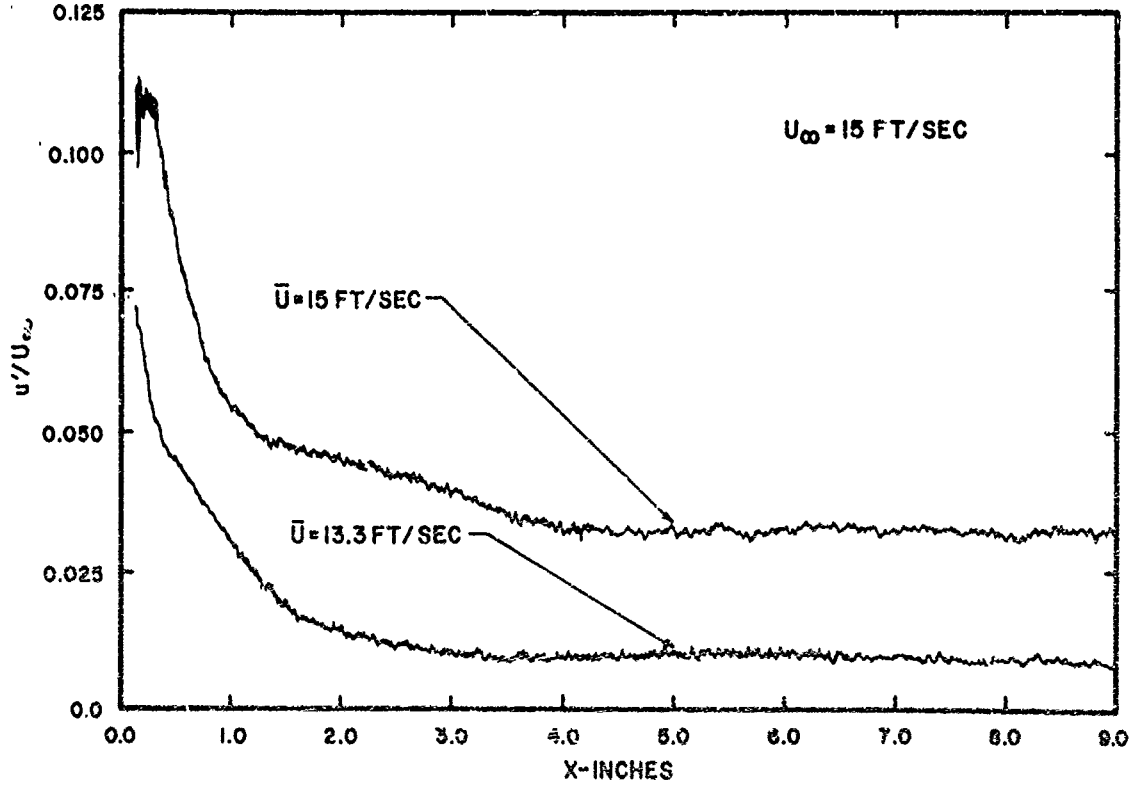

FIG. 67. AXIAL PROFILES OF u'/U_∞ FOR P.P. #1 PLUS FOAM IN TWO RADIAL LOCATIONS IN TEST FLOW CONDITION "A".

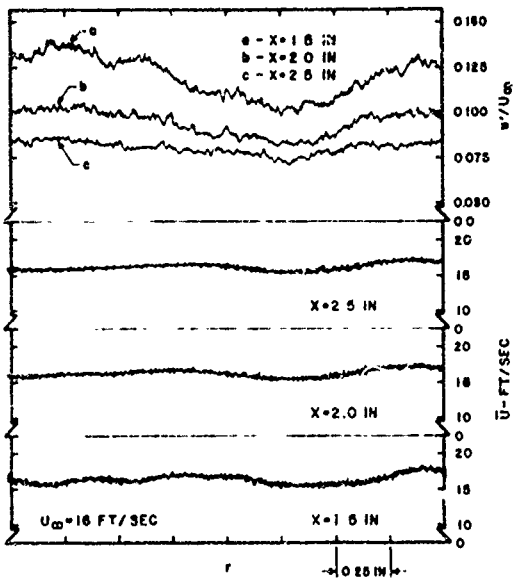

FIG. 68. RADIAL PROFILES OF $\bar{U}$ AND u'/U_∞ FOR P.P. #3 AT DIFFERENT AXIAL LOCATIONS IN TEST FLOW CONDITION "D".

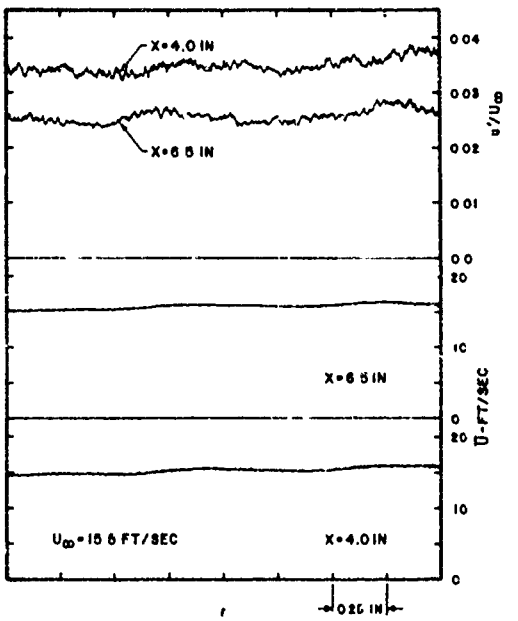

FIG. 69. RADIAL PROFILES OF $\bar{U}$ AND u'/U_∞ FOR P.P. #3 PLUS 3 IN. STRAWS AT DIFFERENT AXIAL LOCATIONS IN TEST FLOW CONDITION "D".

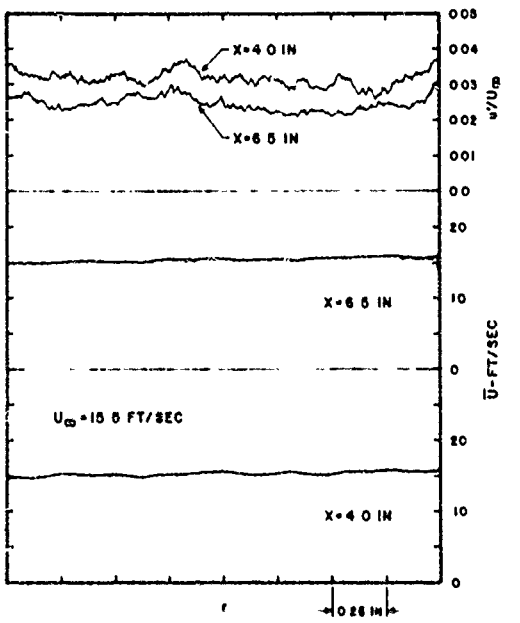

FIG 70. RADIAL PROFILES OF $\bar{U}$ AND u'/U_∞ FOR PP. #3 PLUS 3 IN. STRAWS PLUS SCREEN AT DIFFERENT AXIAL LOCATIONS IN TEST FLOW CONDITION "C".

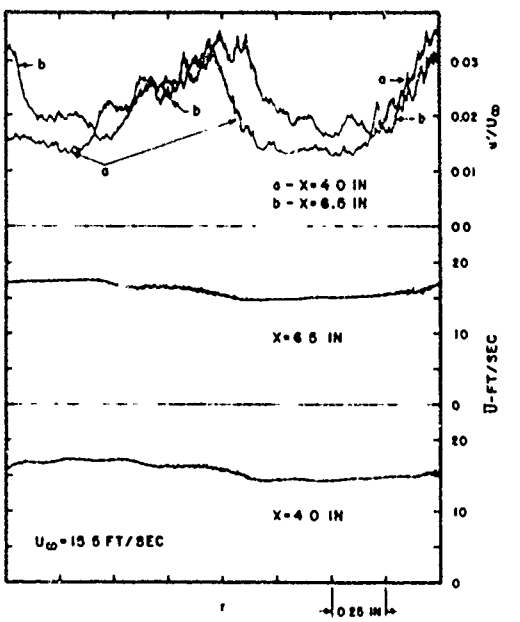

FIG. 71. RADIAL PROFILES OF $\bar{U}$ AND u'/U_∞ FOR 3 IN. STRAWS PLUS SCREEN AT DIFFERENT AXIAL LOCATIONS IN TEST FLOW CONDITION "D".

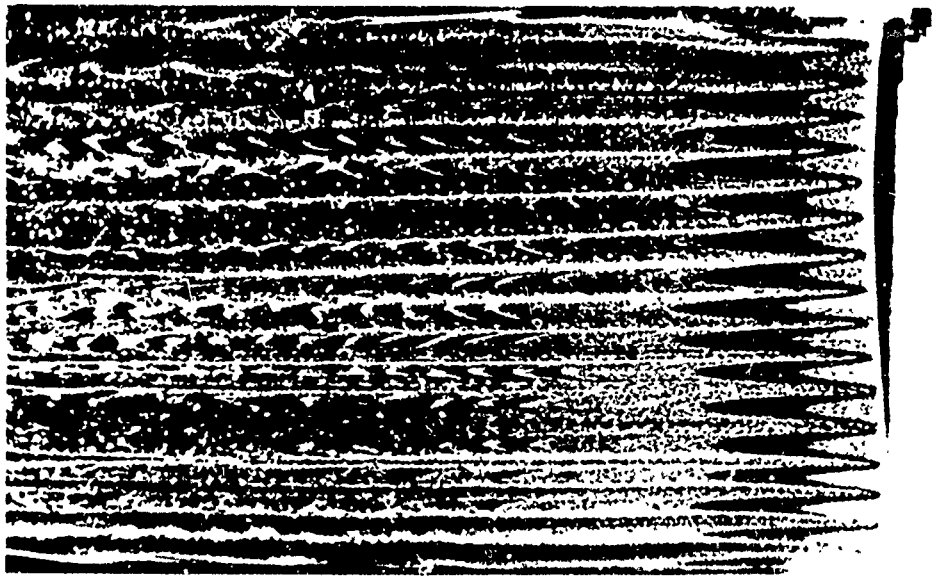

a - U_∞ = 0.25 FT/SEC

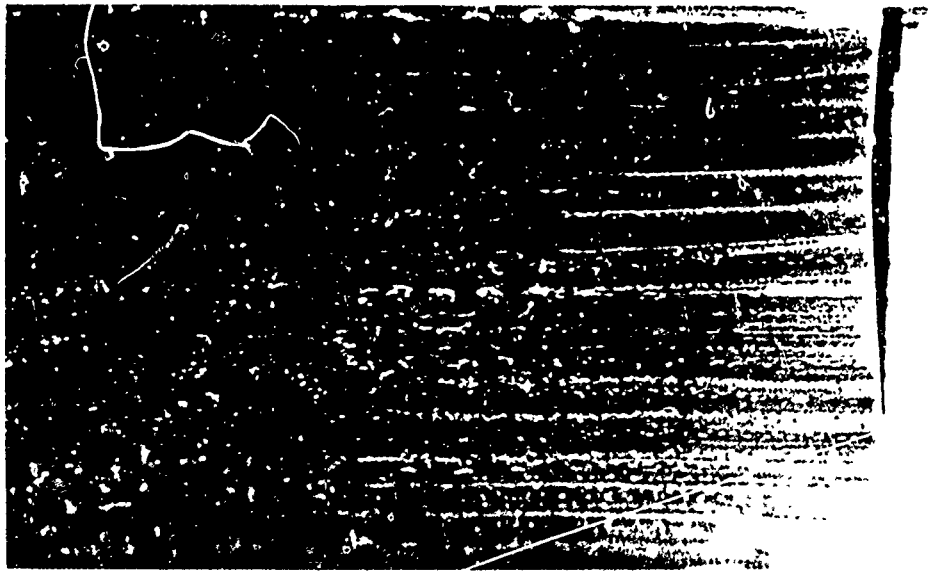

b - U_∞ = 0.47 FT/SEC

FIG. 72. VISUALIZATION OF FLOW DOWNSTREAM FROM 10 IN. STRAWS AT TWO DIFFERENT REYNOLDS NUMBERS.

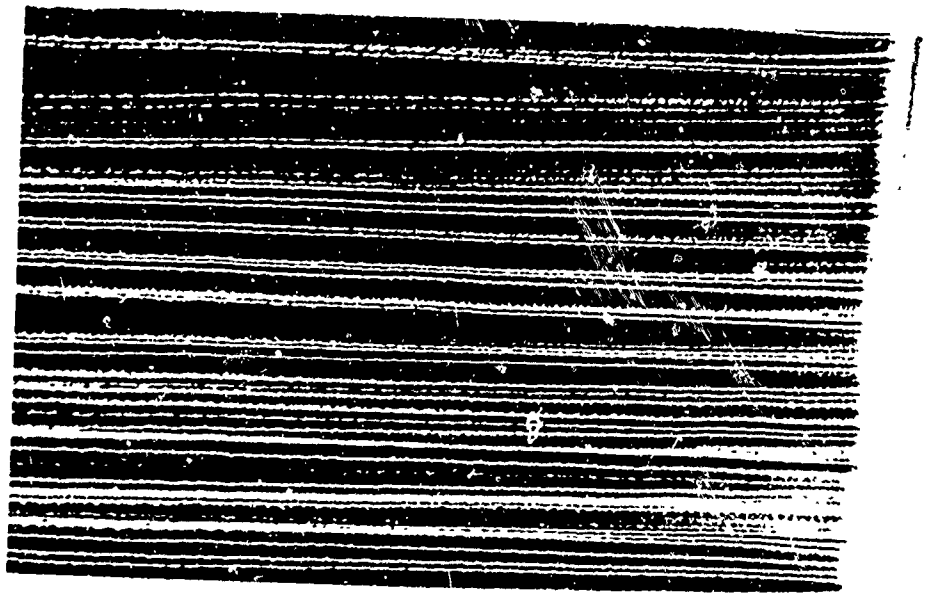

a – U_∞ = 0.26 FT/SEC

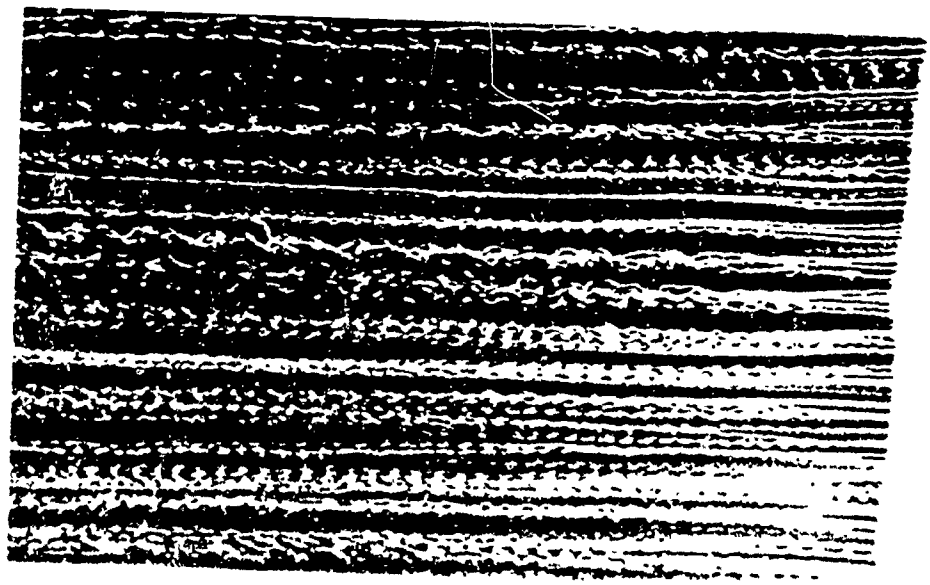

b – U_∞ = 0.45 FT/SEC

FIG. 73. VISUALIZATION OF FLOW DOWNSTREAM FROM 10 IN. STRAWS PLUS SCREEN AT TWO DIFFERENT REYNOLDS NUMBERS.

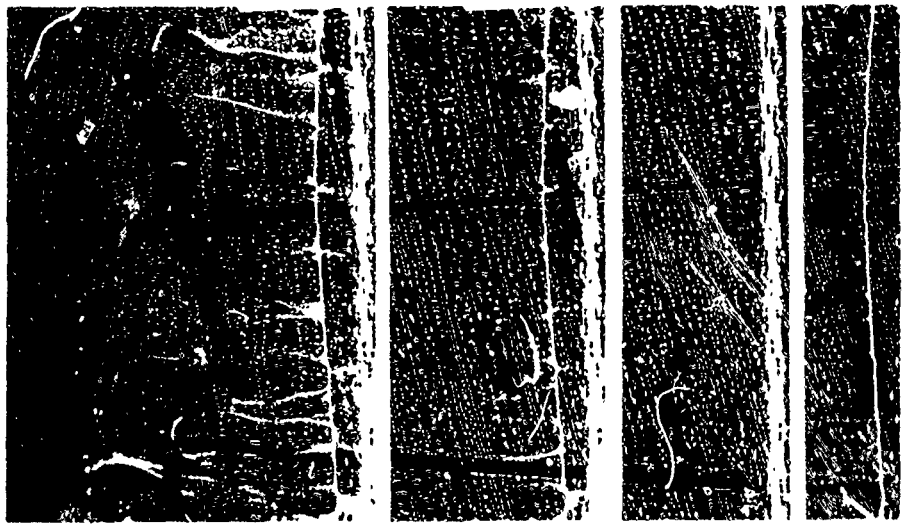

d c b a

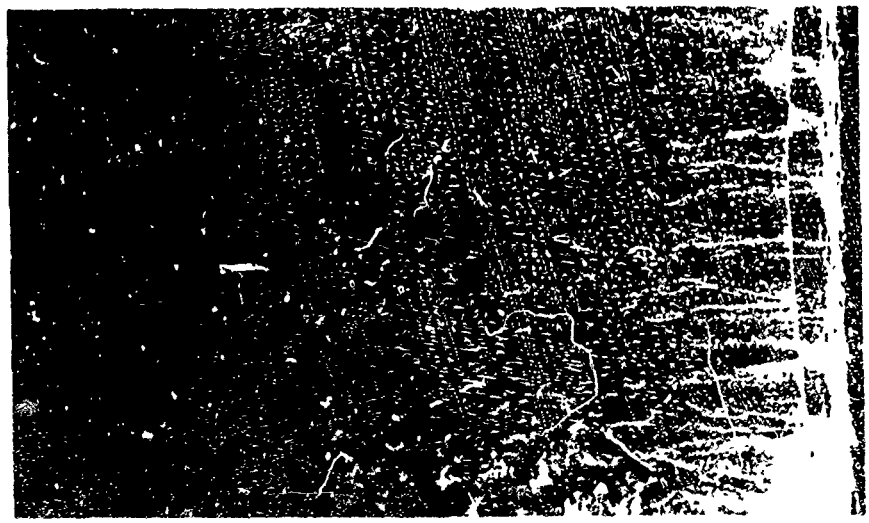

e

U_∞ = 0.11 FT/SEC

FIG. 74. VISUALIZATION OF DEVELOPMENT OF INSTABILITY AND TURBULENCE DOWNSTREAM FROM P.P. #3.

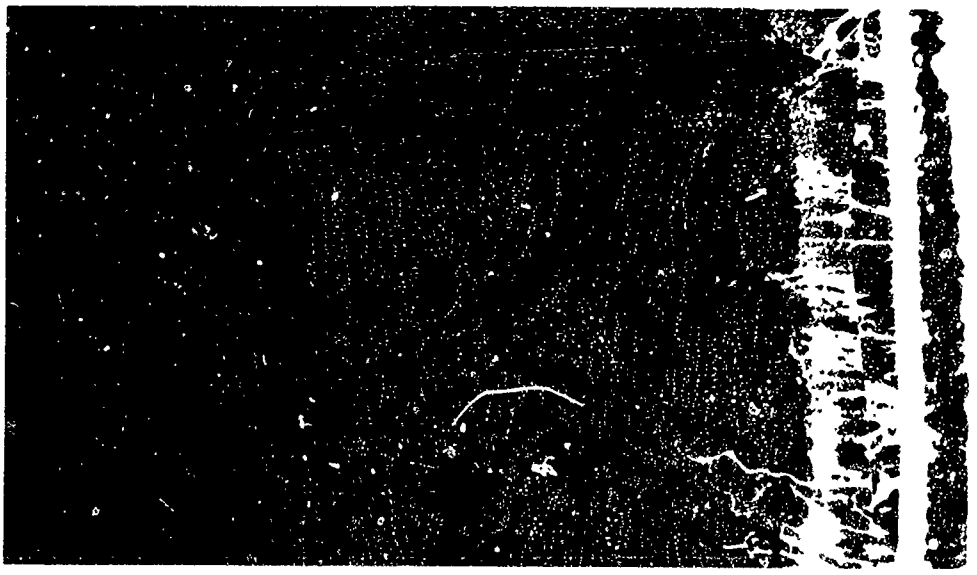

a – P.P. #1 U_∞ = 0.11 FT/SEC

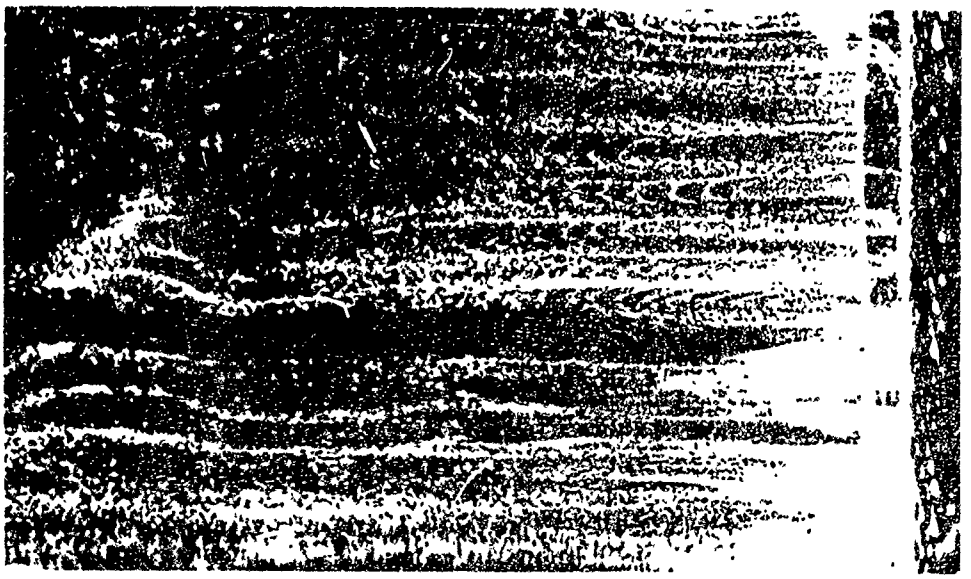

b – P.P. #2 U_∞ = 0.07 FT/SEC

FIG. 75. VISUALIZATION OF FLOW DOWNSTREAM FROM P.P. #1 AND P.P. #2.

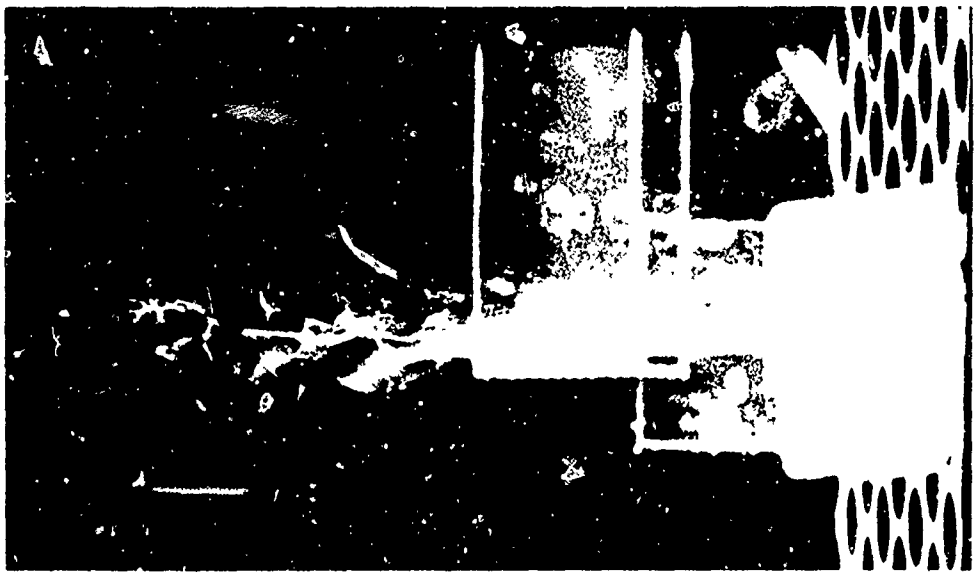

a – P.P. # 3 (Side View) U_∞ = 0.11 FT/SEC

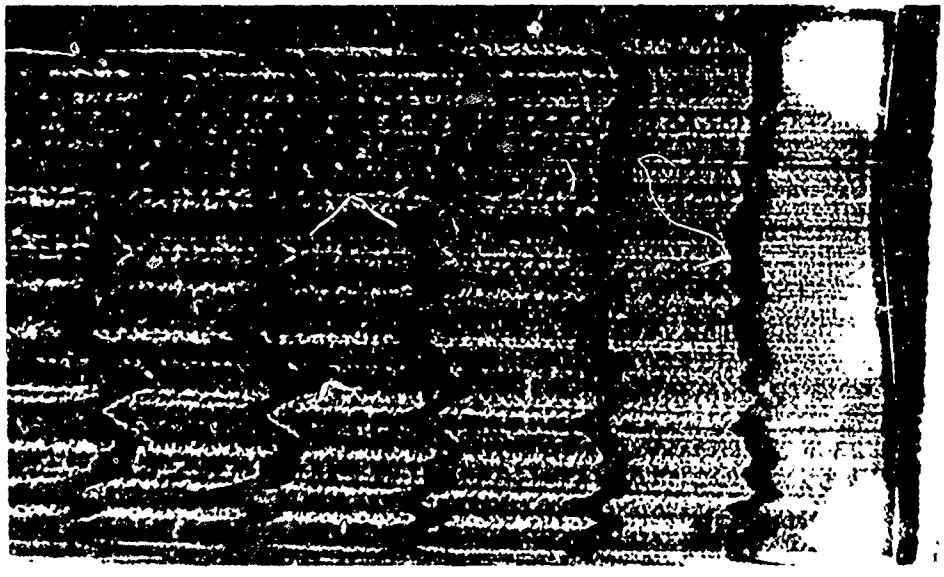

b – P.P. # 3 + Foam U_∞ = 0.11 FT/SEC

FIG. 76. VISUALIZATION OF THREE-DIMENSIONALITY OF INSTABILITY DOWNSTREAM FROM P.P. # 3 AND FLOW DOWNSTREAM FROM P.P. # 3 PLUS FOAM.

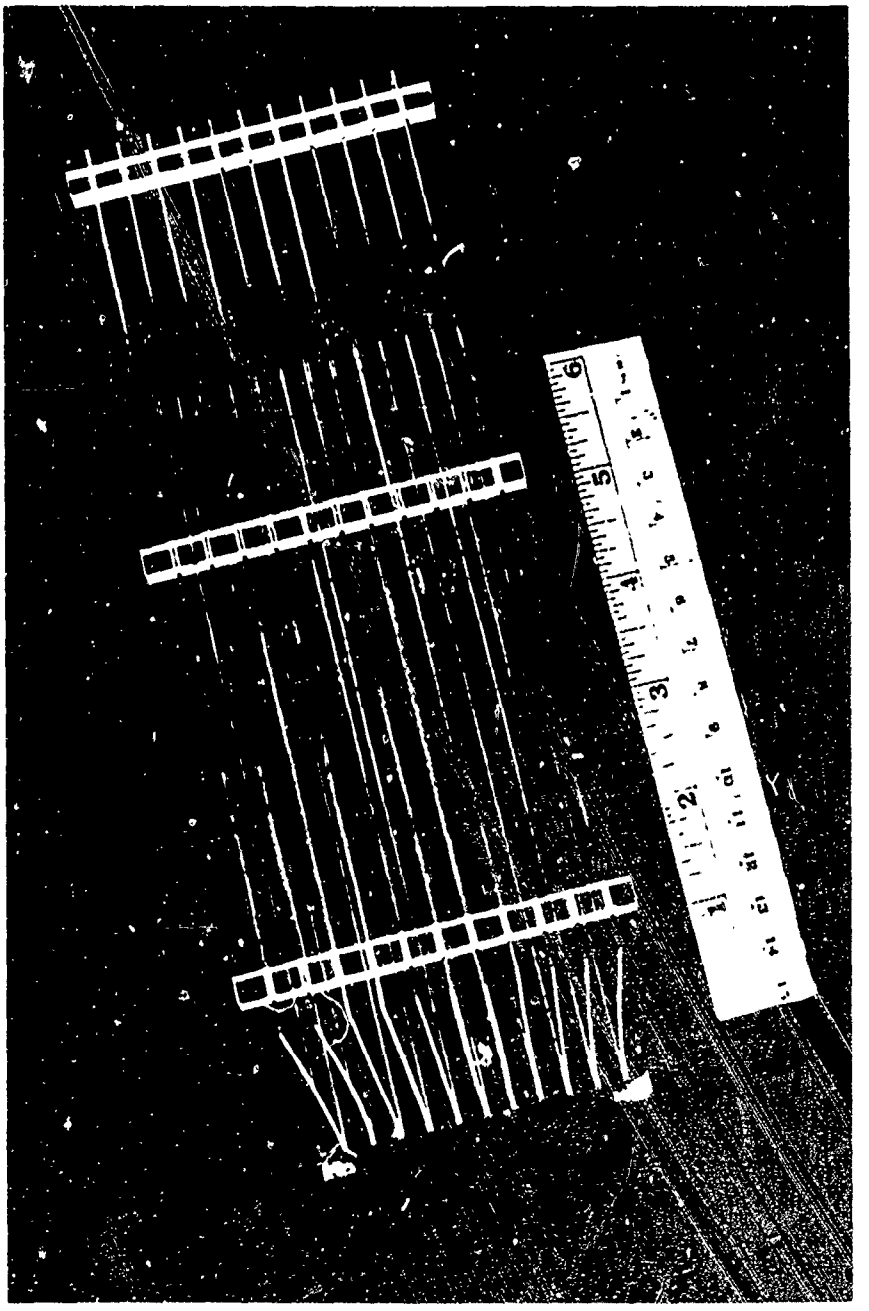

FIG. 77. PHOTOGRAPH OF PARALLEL PLATE ASSEMBLY USED IN FLOW VISUALIZATION.

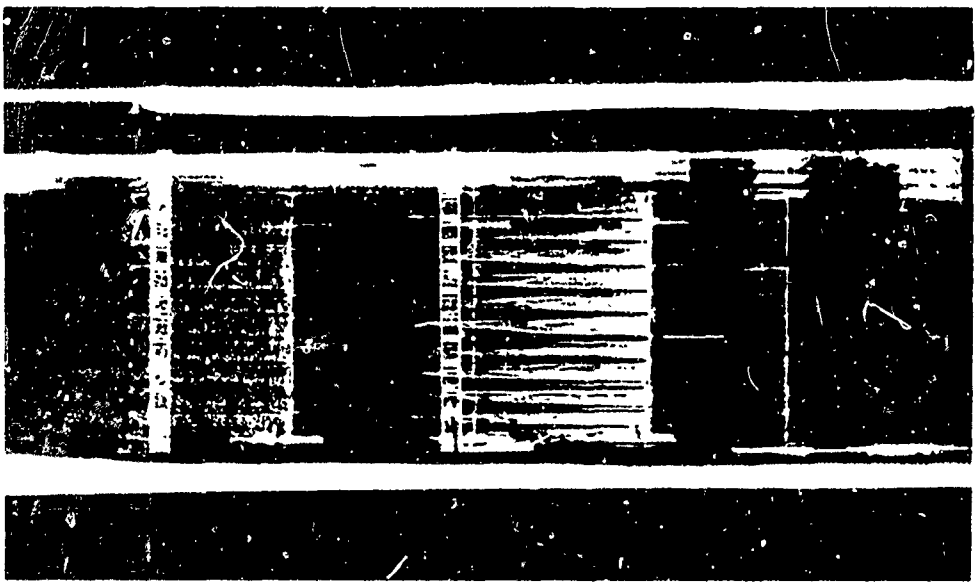

a – U_∞ = 0.22 FT/SEC

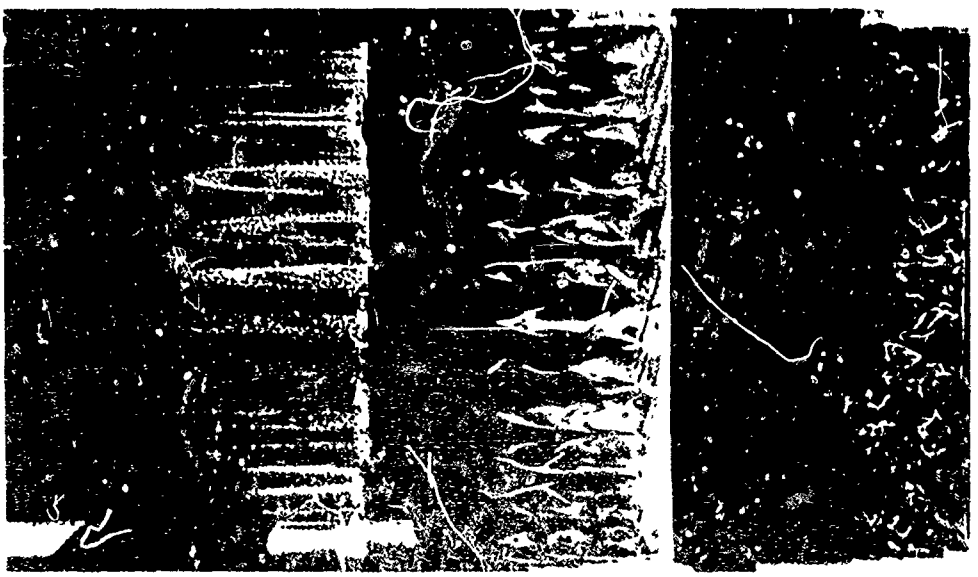

b – U_∞ = 0.22 FT/SEC

FIG. 78. VISUALIZATION OF FLOW UPSTREAM AND THROUGH PARALLEL PLATE MANIPULATORS.

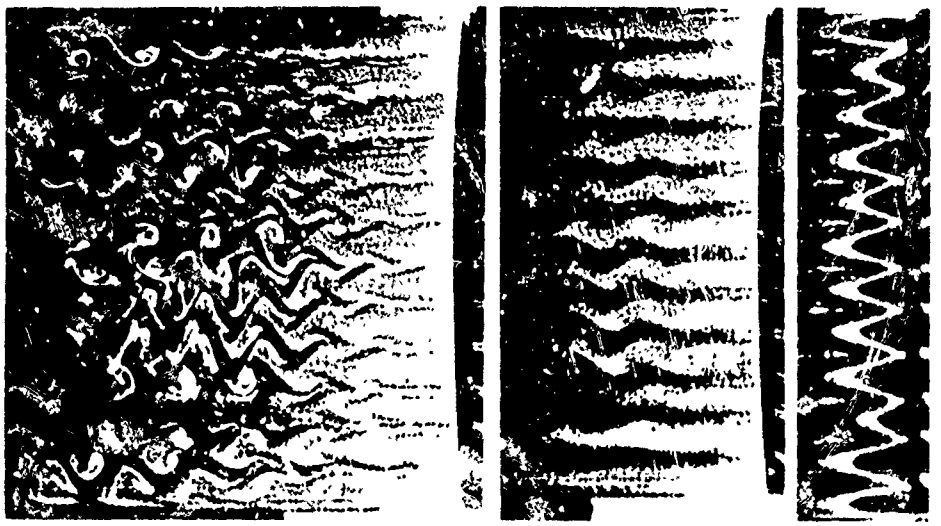

c b a

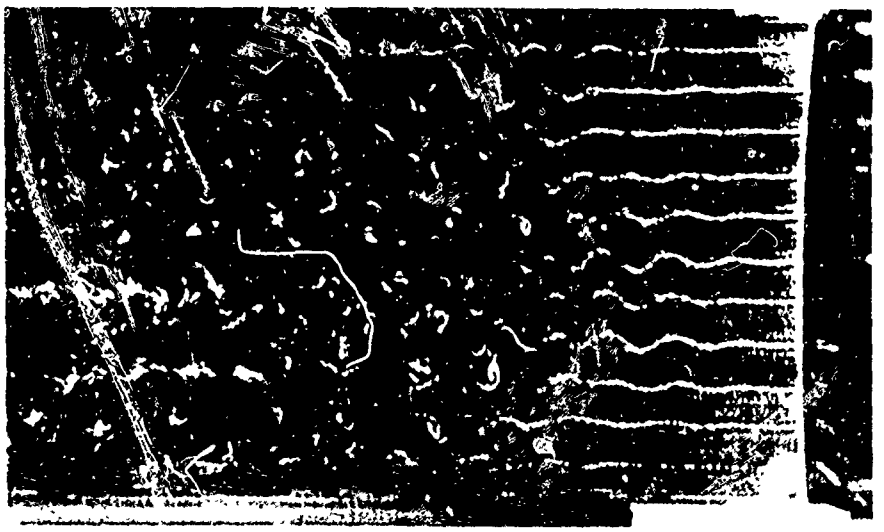

d

U_∞ = 0.13 FT/SEC

FIG. 79. VISUALIZATION OF DEVELOPMENT OF INSTABILITY AND TURBULENCE DOWNSTREAM FROM PARALLEL PLATE MANIPULATOR.

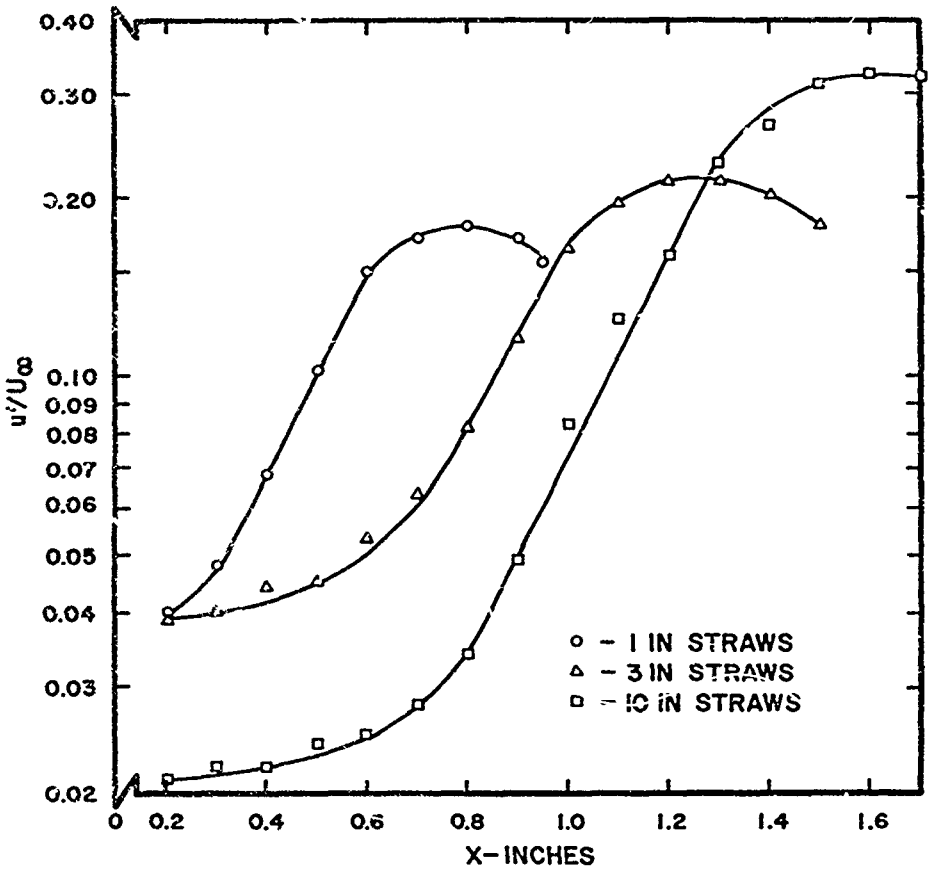

FIG. 80. GROWTH RATE OF INSTABILITY IMMEDIATELY DOWNSTREAM FROM STRAWS.

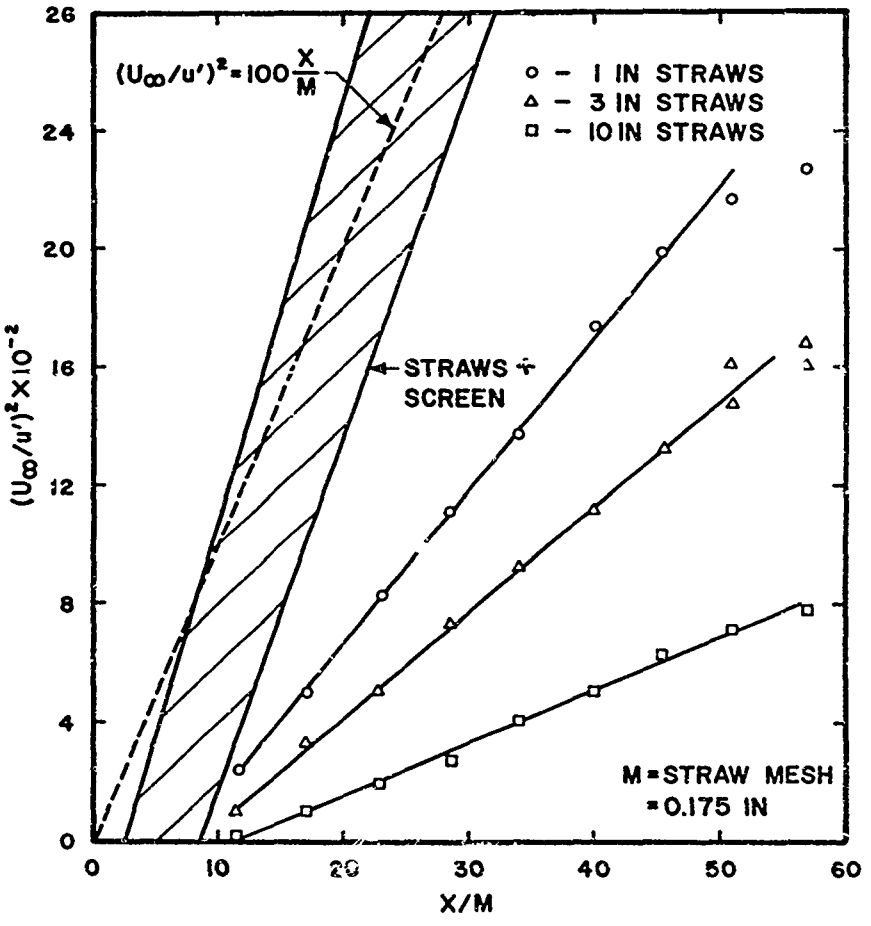

FIG. 81. $(U_\infty/u')^2$ VERSUS x/M COMPARISON BETWEEN STRAWS ALONE AND STRAWS PLUS SCREEN IN TEST FLOW CONDITION "A".

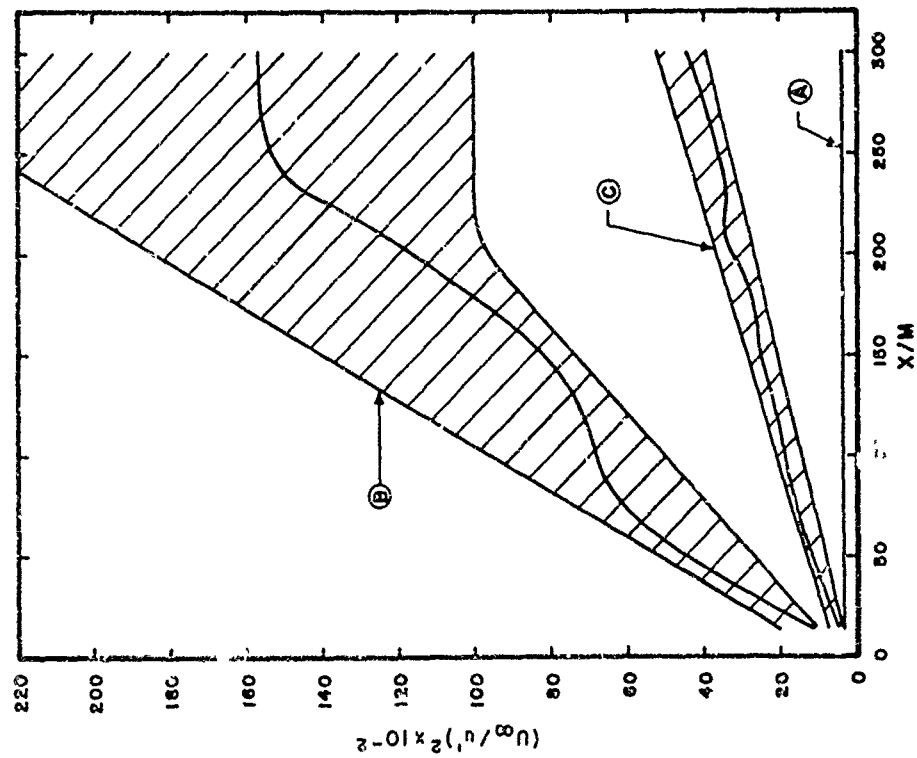

FIG. 83. $(U_\infty/u')^2$ VERSUS x/M FOR SINGLE SCREEN IN TEST FLOW CONDITIONS "A", "B" AND "C".

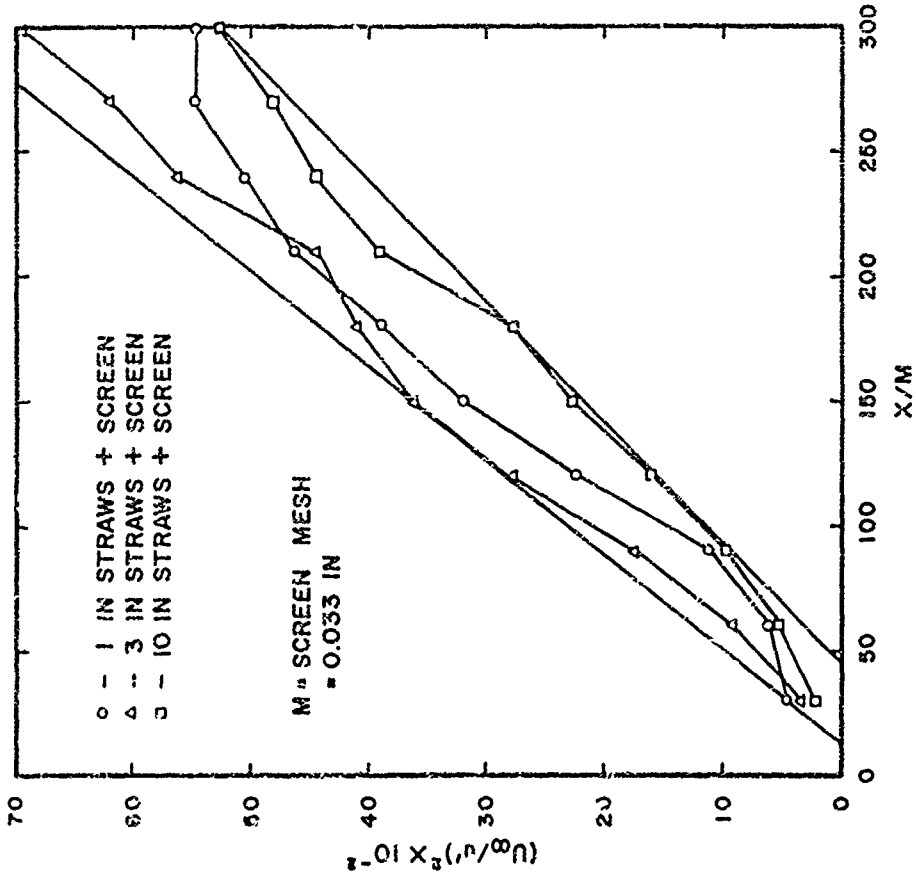

FIG. 82. $(U_\infty/u')^2$ VERSUS x/M DOWNSTREAM FROM STRAWS PLUS SCREEN IN TEST FLOW CONDITION "A".

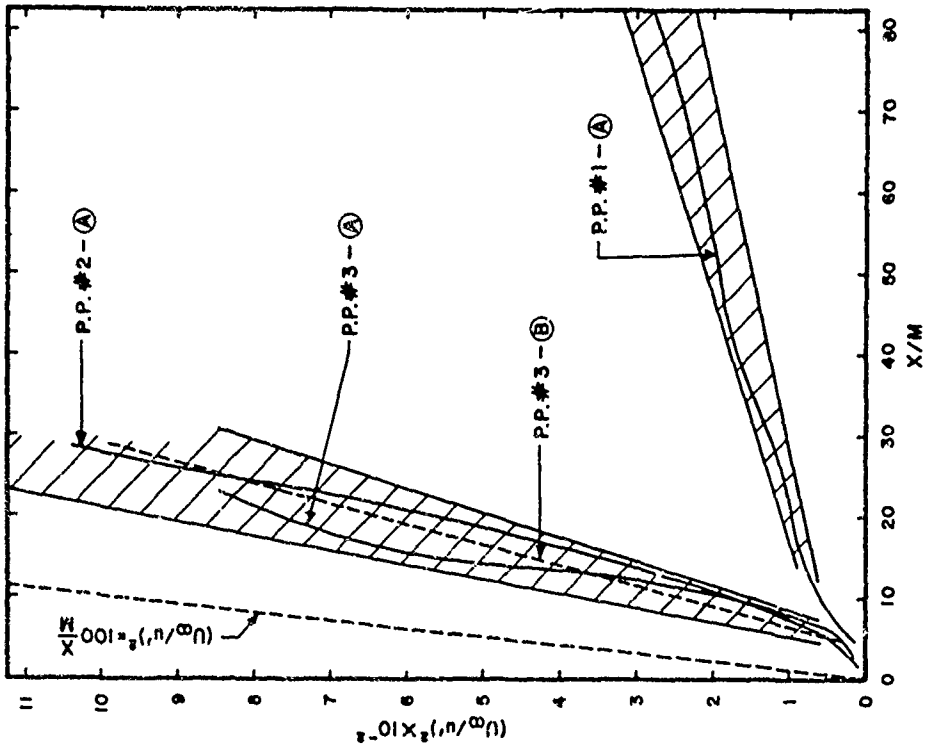

FIG. 85. $(U_\infty/u')^2$ VERSUS x/M DOWNSTREAM FROM PERFORATED PLATES IN TEST FLOW CONDITIONS "A" AND "B".

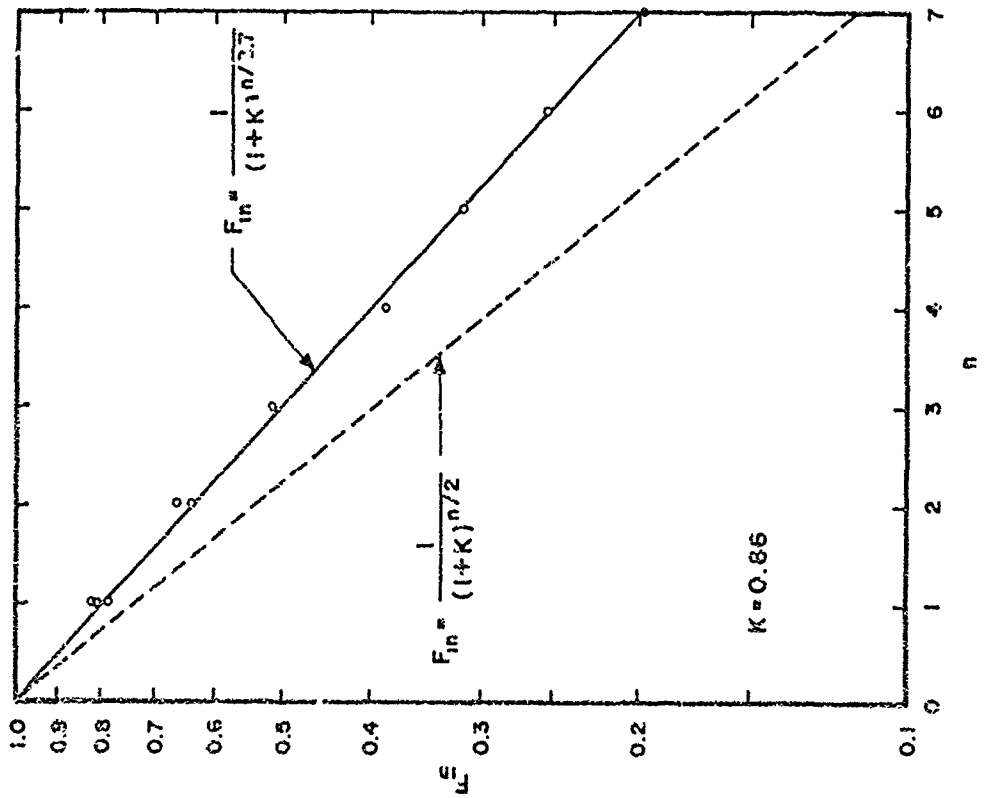

FIG 84. SCREEN TURBULENCE REDUCTION FACTOR VERSUS NUMBER OF SCREENS IN TEST FLOW CONDITION "A".

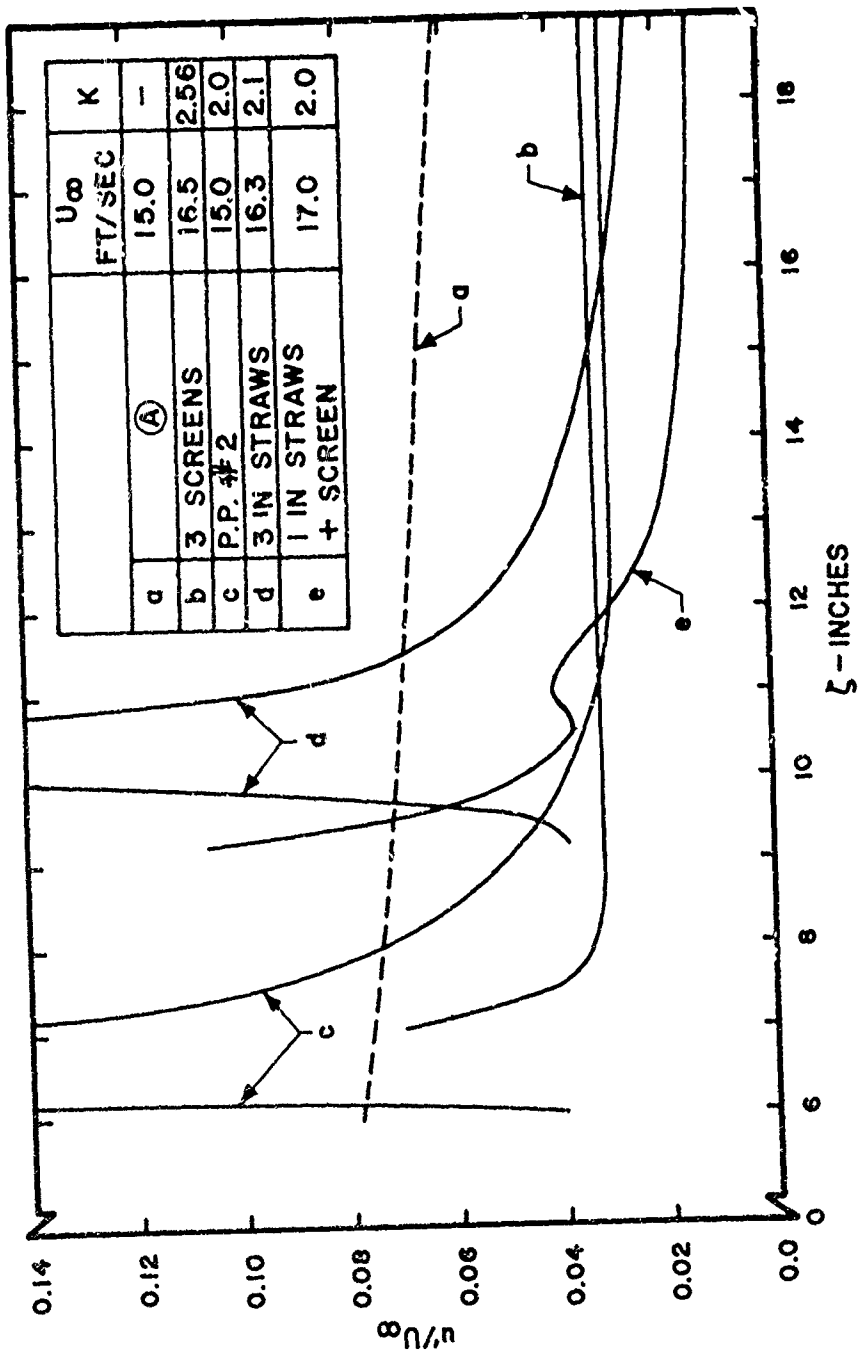

FIG. 86. COMPARISON OF TURBULENCE DAMPING FOR MANIPULATORS OF ALMOST EQUAL PRESSURE DROP COEFFICIENT.

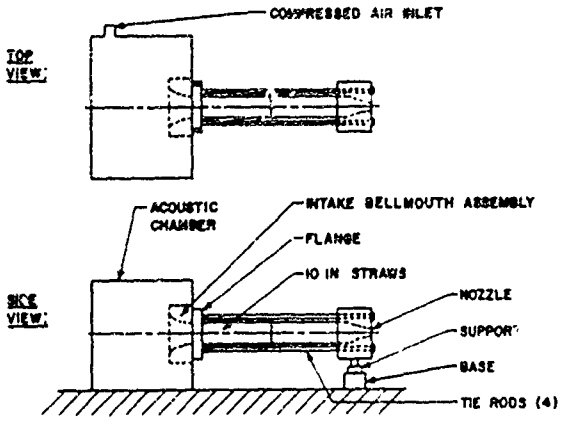

FIG. 87. ASSEMBLY DRAWING OF WIND TUNNEL IN CALIBRATION CONFIGURATION.

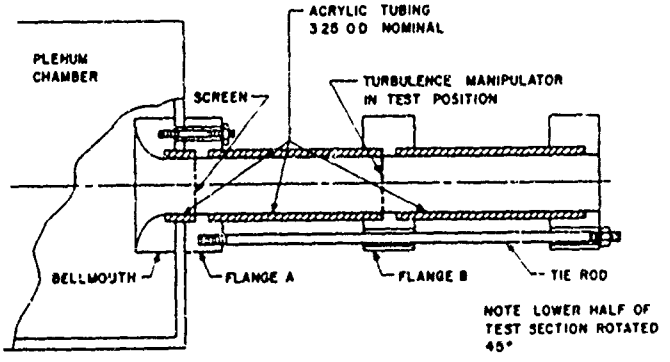

FIG. 88. TYPICAL TEST SECTION ASSEMBLY FOR TURBULENCE MANAGEMENT STUDIES.

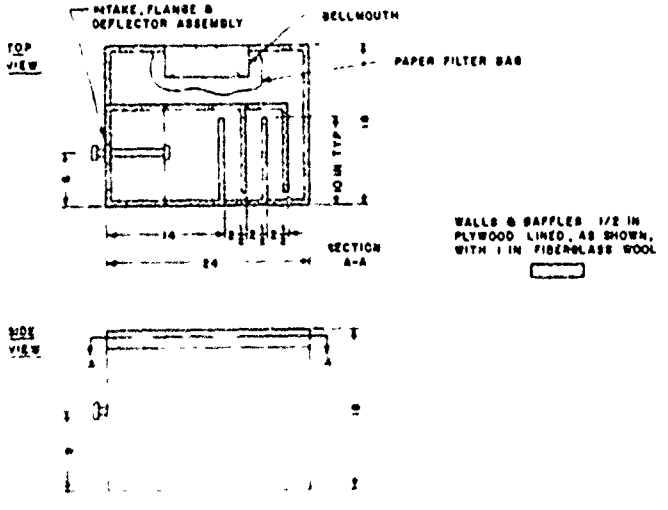

FIG 89 PLENUM CHAMBER DESIGN DETAILS.

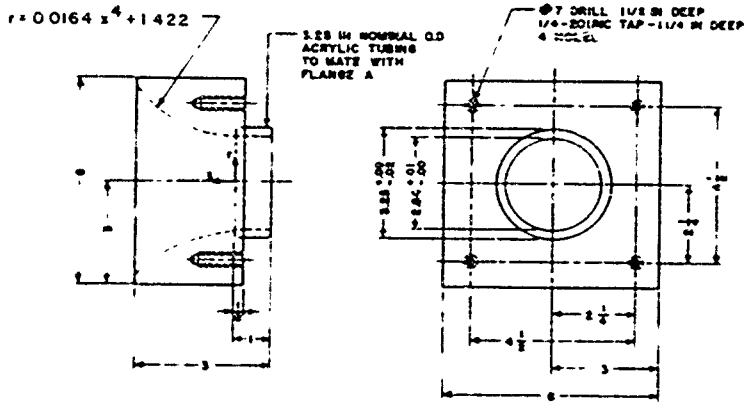

FIG 90 DETAIL DRAWING OF BELLMOUTH ASSEMBLY

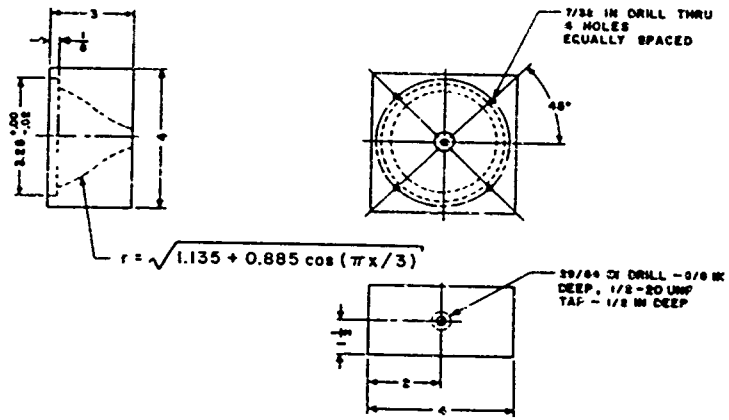

FIG. 91. CALIBRATION NOZZLE DETAILS.

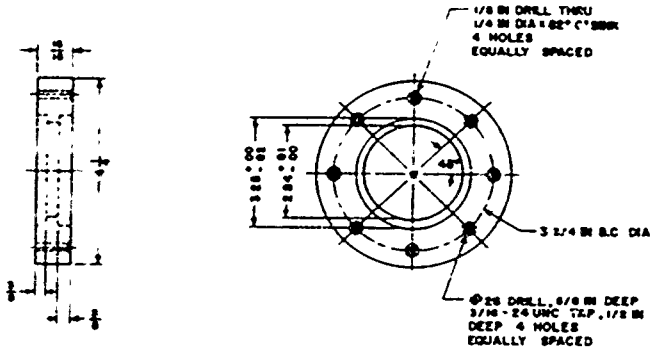

FIG 92 DETAIL OF FLANGE A.

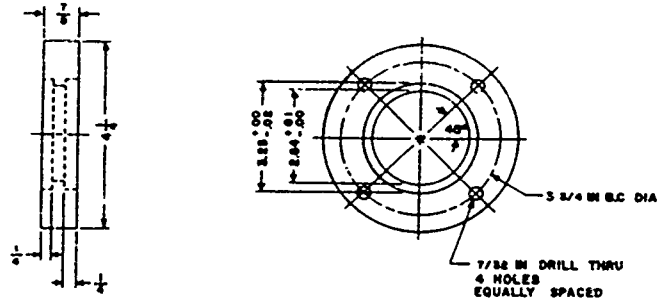

FIG. 93. DETAIL OF FLANGE 3